A Thesis for the Degree of Ph.D. in Engineering

Validation of Vortex Methods as a Direct Numerical Simulation of Turbulence

July 2009

Graduate School of Science and Technology
Keio University

Rio Yokota

©2008
Rio Yokota
All Rights Reserved

To my parents, Yuri and Hisashi Yokota.

Acknowledgements

I wish to express my deepest gratitude to my advisor, Prof. Shinnosuke Obi, for his guidance and support during my graduate studies. I would like to thank him in particular for the freedom he allowed in the course of this investigation and also for his valuable advice at times when they were necessary. His guidance has been the most important factor to my success.

I wish to sincerely thank the members of my examining committee: Prof. Naoki Takano, Prof. Tatsuo Sawada, and Prof. Kenji Yasuoka, for lending their time, interest and insight. I am extremely grateful to Prof. Kenji Yasuoka for his continued interest in my progress, and for sharing the state-of-the-art computational resources that have significantly accelerated the progress of my studies. I would like to thank Dr. Tetsu Narumi for all the fruitful discussions on the implementation issues regarding the MD-GRAPE and GPU. I am also grateful to Prof. Kyoji Kamemoto, Prof. Teruhiko Kida, Dr. Akira Ojima, and Dr. Kota Fukuda for the fruitful discussions on vortex methods. I also thank Prof. Shigeaki Masuda and Dr. Koji Fukagata for valuable suggestions during the weekly seminars.

I would also like to thank my friends and colleagues at the lab for their contributions and support. I am grateful to Dr. Tarun Kumar Sheel for his enthusiasm that has helped motivate me for many years. I thank Qiu Jifeng for his friendship and support, and the delicious dumplings that he cooks. I am also grateful to Yoshitsugu Naka for being a consistent running partner, for his encyclopedic knowledge of computers, and his sense of humor, which has made this otherwise rough journey an enjoyable one.

I must thank the staff of the Yagami ITC and mediacenter for their assistance. I am also grateful to the KLL for the financial assistance that made this work possible. I also thank Hisataka Oiwa for his support when I was a research assistant at the draft room.

Finally, I would like to thank my parents who are always there for me. I am grateful for their encouragement and unending support.

Abstract

Vortex methods have made remarkable advancements in the past decade, and now offer an interesting alternative to finite difference and spectral methods for the numerical simulation of turbulence, especially for external flows involving unsteady vortical motion. However, the lack of validation in simple flows has left many fundamental questions unanswered. The aim of this thesis is to provide a concrete answer to these fundamental questions by systematically benchmarking the vortex method for simple turbulent flows.

The simulation of turbulence requires the accurate prediction of the production and dissipation of kinetic energy. In vortex methods, this is made possible by properly calculating the stretching term and diffusion term of the vorticity equation. The homogeneous isotropic turbulence does not involve any mean shear and near wall effects. Therefore, it is suitable for the isolated validation of the viscous diffusion problem, and serves as the starting point of the present sequence of validation. The homogeneous shear flow involves mean shear (strong stretching), but no near wall effects. Thus, it serves the role of validating the stretching term, while adding minimum complexity to the isotropic case. The turbulent channel flow involves all three difficulties but is still geometrically simple and an equilibrium turbulent flow. The availability of credible references also proved to be helpful when validating the near wall issues of vortex methods.

In all three flows, the present vortex method has shown quantitative agreement with the reference calculations using finite difference and spectral methods. The match of the decay rate of kinetic energy and the energy spectra in the homogeneous isotropic turbulence calculation exemplifies the high accuracy of the present viscous diffusion scheme. The match of the time evolution of the anisotropy tensors and joint probability density functions of velocity in the homogeneous shear flow shows the soundness of our stretching calculation. Finally, the agreement of the mean velocity profile in the turbulent channel flow indicates the overall soundness of our vortex method in the presence of solid boundaries.

Contents

List of Figures

Nomenclature

Upper-Case Roman

D	Wigner D matrix
$\mathcal{E}$	Two point double correlation tensor
E	Kinetic energy
$\mathbf{G}$	Vector Green's function
G	Green's function
$\mathcal{I}$	Identity operator
I	Identity matrix
$\mathcal{K}$	Turbulent kinetic energy
K	Number of quadratures on spherical-t
$\mathcal{L}$	Differential operator
L	Local expansion, Integral length scale
M	Multipole expansion
P	Probability density
S	Shear rate
$\mathcal{T}$	Two point triple correlation tensor
T	Eddy turnover time
U	Time averaged velocity
W	Interpolation kernel

Lower-Case Roman

d	Dimensionality of the problem
f	Convection term of the Navier-Stokes equation
$\mathbf{f}$	Force vector
g	Cutoff function
h	Inter-particle spacing

$\mathbf{k}$	Wave number vector
k	Wave number, Exponent of the number of periodic images
$\mathbf{n}$	Unit normal vector
p	Pressure, Potential, Number of multipole moments
$\mathbf{q}$	Vector source strength
q	Source strength
$\mathbf{r}$	Distance vector
r	Distance for spherical coordinate of source element
t	Time
$\mathbf{u}$	Velocity vector
u	Fluctuating component of velocity
w	Complex velocity
z	Complex coordinate

Upper-Case Greek

$\mathbf{\Gamma}$	Circulation vector
Δ	Difference
Φ	Scalar potential
$\mathbf{\Psi}$	Vector potential
Ω	Time averaged vorticity

Lower-Case Greek

$\boldsymbol{\alpha}$	Vortex strength of element
α	Azimuthal angle for spherical coordinate of source element
β	Polar angle for spherical coordinate of source element
γ	Angle between the source and target element
δ	Dirac's delta function
ϵ	Permutation tensor, Turbulent dissipation
ζ	Smoothing function, Enstrophy
η	PSE kernel
θ	Azimuthal angle for spherical coordinate of target element
ι	Imaginary unit
λ	Taylor's microscale
μ	Ratio between the distance of source and target element
ν	Kinematic viscosity

π	Circumference ratio
ρ	Density, Distance for spherical coordinate of target element
ϕ	Polar angle for spherical coordinate of target element
$\boldsymbol{\omega}$	Vorticity vector
ω	Fluctuating component of vorticity

Subscripts

u_i	Properties of target element (vector notation)
u_j	Properties of source element (vector notation)
u_σ	Non-raidally-symmetric kernel
u_Φ	Properties of the potential field
$u_{\boldsymbol{\Psi}}$	Properties of the solenoidal field
u_∞	Properties of the far field
u_*	Properties of origin of expansion

Superscripts

u^p	Properties of target element (index notation)
u^q	Properties of source element (index notation)
u^*	Non-dimensional properties
$\bar{u}$	Complex conjugate
$\hat{u}$	Fourier component
$\tilde{u}$	Instantaneous component

Symbols

$\sum$	Summation
∇	Differential operator
!	Factorial
$\lvert u \rvert$	Absolute value
$\int_\Gamma d\Gamma$	Boundary integral
$\int_\Omega d\Omega$	Domain integral

Chapter 1

Introduction

1.1 Background

This thesis is concerned with the validation of vortex methods (a Lagrangian numerical method, based on the velocity-vorticity formulation) as a direct numerical simulation of unsteady, incompressible, viscous flows. Vortex methods have made remarkable advancements in the past decade, and now offer an interesting alternative to finite difference and spectral methods for the numerical simulation of turbulence, especially for external flows involving unsteady vortical motion. However, the lack of validation in canonical flows has left many fundamental questions unanswered. The aim of this thesis is to provide a concrete answer to these fundamental questions, and enhance the reliability of vortex methods in engineering applications.

Vortex methods possess the following essential advantages over grid based methods. First of all, vortex methods calculate the convection in a Lagrangian manner by moving the calculation points according to the local velocity. Thus, it is free of numerical diffusion and dispersion, and allows the use of larger time step sizes because it is not subject to numerical instabilities arising from the convection. This feature alone allows the vortex method to become an order of magnitude faster than finite difference methods.[1] Furthermore, the velocity-vorticity formulation allows the vortex method to place calculation points only in the regions of non-zero vorticity. For external flows, this results in a large reduction of the number of calculation points because the vorticity is confined to a thin region near the wall. Despite these advantages, the vortex method has received only a small amount of attention.

1.2 Related Previous Studies

The origins of the vortex method can be traced back to the inviscid two dimensional calculations of the Kelvin-Helmholtz instability by Rosenhead.[2] The elements used in this calculation were singular point vortices, which tracked the motion of the vortex sheet roll-up. The study of Rosenhead was followed by similar calculations using regularized point vortices, which resulted in a more stable calculation.[3][4] The convergence of the two dimensional point vortex method for Euler's equations was proven by Hald.[5] Proof was provided for the existence of a solution as long as the vortex blobs overlapped sufficiently. This was extended to three dimensions by Beale & Majda [6] using Lagrangian update to compute the stretching. Another ancestor of the vortex method is the panel method[7], which is a method that solves the potential flow around a body of arbitrary shape. It has been widely used in aeronautical industries during the 1980's and early-90's. The panel method is nowadays considered as a special case of the boundary element method.[8] Actually, all the techniques mentioned above can be integrated into a single framework, as the solution of the Poisson equation using Green's functions.[9] Therefore, the detailed understanding of the individual methods mentioned above is not a prerequisite for understanding modern vortex methods.

The extension to viscous flows has been the focal point of interest in vortex methods during the 1980's and early 1990's. Among others, the random vortex method (RVM) by Chorin[10], the core spreading method (CSM) by Leonard[11], and the particle strength exchange (PSE) by Degond & Mas-Gallic,[12] were introduced as methods to calculate the diffusion in vortex methods. The inherent difficulty in calculating the diffusion in a Lagrangian framework has lead to the use of semi-Lagrangian methods such as the vortex-in-cell (VIC).[13] The viscous treatment near the wall has been of prime difficulty and also of prime importance, since the wall diffusion is the source of the entire vorticity in the vortex method simulation. Chorin[14] first proposed a method that used sheet elements that move randomly in the vicinity of a wall. Fishelov[15] used the Prandtl equations for a thin layer to calculate the wall diffusion. Although some of these methods evolved into rigorous direct numerical simulations of the Navier-Stokes equations during the next decade, the methods mentioned above were in no way comparable to finite difference methods of that time, in terms of both accuracy and speed. The intention during this era was not to fully resolve the high Reynolds number fluid flow, but to somewhat mimic the dominant vortex dynamics using discrete vortex elements.

During the 1990's and early 2000's, the viscous vortex method framework was reinforced by the introduction of essential tools. Winckelmans & Leonard [16] gives a detailed

mathematical formulation of the three dimensional viscous vortex method, with particular emphasis on the smoothing functions and stretching term calculation. Remeshing techniques to deal with the Lagrangian distortion of vortex elements were also introduced during this period. The use of spatially varying element sizes has been investigated for the VIC[17] and PSE[18]. Near wall treatment of vortex methods advanced remarkably during this period. Koumoutsakos *et al.* formulated the basic equations for the two dimensional case.[19] The equations were slightly modified to achieve higher accuracy[20] and extended to three dimensions by Ploumhans *et al.*[21] Furthermore, fast algorithms such as the treecode by Barnes & Hut [22] and the fast multipole method (FMM) by Greengard & Rokhlin [23] were applied to vortex method calculations. This reduced the calculation cost from $O(N^2)$ to $O(N \log N)$ and $O(N)$ for the treecode and FMM, respectively. Specialized hardware for N-body problems were also developed during this period[24] [25]. These efforts led to a new paradigm, *i.e.* solving flows of moderate Reynolds numbers and fully resolving these flows. During this period, vortex methods were applied to numerous complex applications, and their results showed that these methods could indeed produce quantitatively correct results.

Recent interest in vortex method studies has been focused on the development of more advanced tools, such as fast N-body solvers [26], high order convergent diffusion schemes [27] [28], and efficient three-dimensional near wall treatment[29]. Further maturation of each of these tools shall soon allow the vortex method to overcome most of its traditional weaknesses. However, the lack of validation in canonical turbulent flows has left the overall reliability of vortex methods in question. The independent sources of errors must be investigated in simple flows, despite the fact that such flows are not always suitable for showing the advantage of vortex methods.

A chronological table of the above mentioned evolution of vortex methods is shown in Fig. 1.1.

1.3 Importance of Systematic Validation

The simulation of turbulence requires the accurate prediction of the production, transport, and dissipation of kinetic energy. In vortex methods, this is made possible by properly calculating the stretching term and diffusion term of the vorticity equation. Vortex methods are a convergent method, but have multiple sources of numerical errors. First, even if a high order convergent diffusion scheme is used, the diffusion term calculation still contains a finite amount of error. The quantity of this error depends

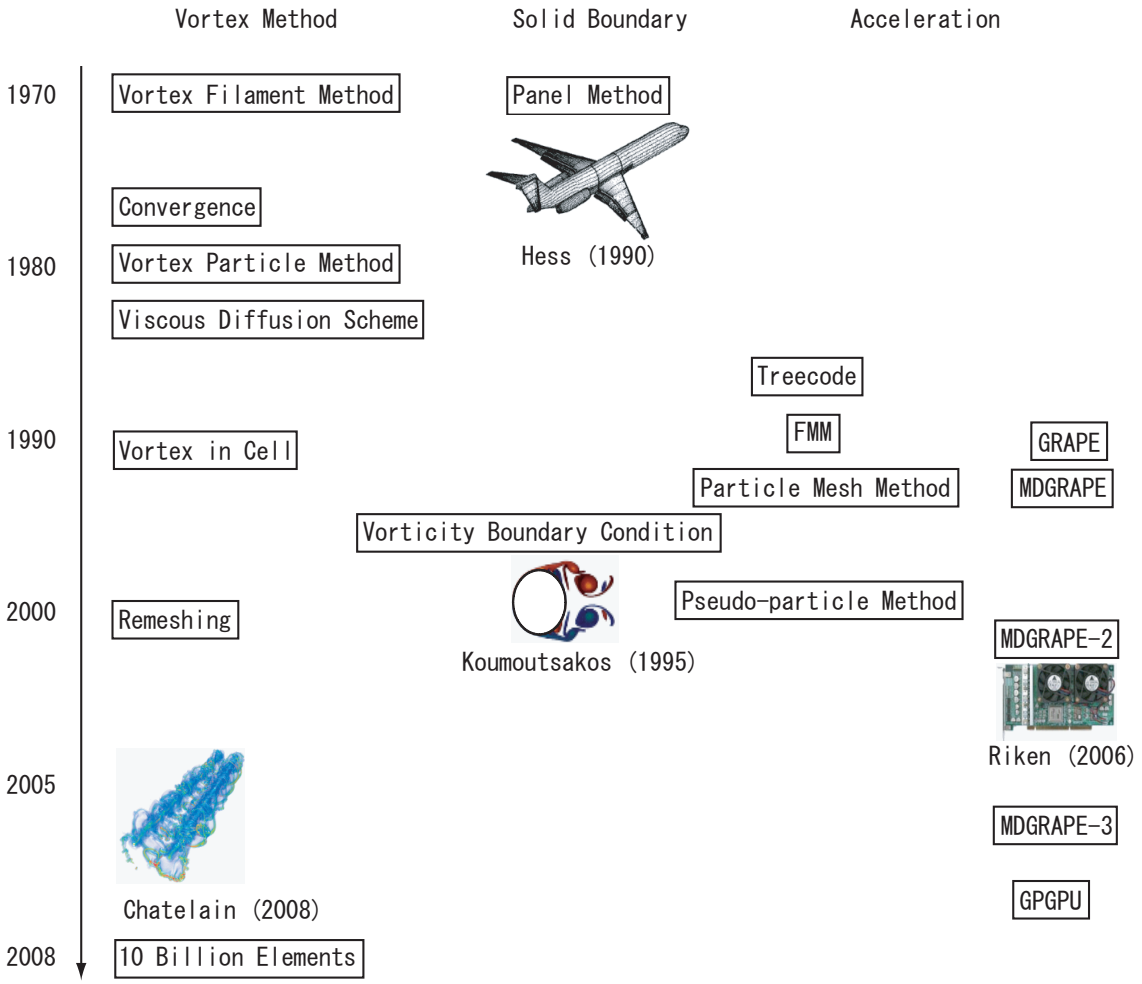

Figure 1.1: Chronological Table of Vortex Methods

on the spatial resolution, the overlap ratio of vortex elements [30], and the frequency of remeshing [31], and cannot be neglected. Another source of error is the stretching term calculation, which is highly sensitive to the spatial and temporal resolution due to its non-linearity [16]. Also, for the regions with high shear, the stretching becomes intense and the flow field becomes highly anisotropic. This may impose additional constraints on the spatial and temporal resolution [31]. It is important to determine the relation between the shear-rate and the constraints on resolution in the absence of a solid boundary. Finally, for regions near a solid boundary, a high spatial resolution in the direction normal to the wall is required. This imposes another restriction on the spatial resolution of vortex elements. It is possible to find an optimum value for the spatial resolution, temporal resolution, remeshing frequency, element anisotropy, and spatial variation of the element size if, and only if, the sources of these errors are considered independently.

There have only been a few attempts to systematically investigate the independent sources of the errors mentioned above. The two-dimensional isotropic turbulence was calculated by Totsuka & Obi [32] using a vortex method and pseudo-spectral method. The rate of energy decay had good agreement with the pseudo-spectral method when spatial adaptation was implemented for their vortex method calculation. A related effort was made by Cottet *et al.* [33] by comparing the vortex-in-cell method to a pseudo-spectral method for the homogeneous isotropic turbulence. Their results also showed good quantitative agreement between the vortex method and pseudo-spectral method calculation, for both the decay of kinetic energy and the energy spectrum.

1.4 Objective

The present study aims to develop a vortex method, which is capable of reproducing the dissipation and production of turbulent kinetic energy at an unprecedented accuracy. In order to achieve this goal, the present study performs a systematic validation of the key components of vortex methods. These key components include the ability to properly calculate the balance between the cascade and dissipation of kinetic energy, the production of the Reynolds stress due to high shear, and the production of vorticity at the wall. The three-dimensional homogeneous isotropic turbulence was calculated in order to assess the balance between the cascade and dissipation of kinetic energy. Following that, the homogeneous shear flow was calculated in order to check the production of the Reynolds stress due to high shear. Finally, the turbulent channel flow was calculated in order to evaluate the production of vorticity at the wall.

1.5 Present Contribution

The following numerical methods are either completely unique to the present study, or were put to practical use for the first time in the present study.

1. A novel technique to perform the spatial adaptation for the core spreading method without increasing the number of elements, is used for the first time in an actual 3-D turbulence

2. The method to generate the initial condition of vortex methods from the data of grid based methods using radial basis function interpolation is developed and used for the first time

3. The fast multipole method is extended to shear periodic boundary conditions for the first time

4. A method to enforce a constant flow rate in a channel is developed and used for the first time

1.6 Contents of the Thesis

The thesis is organized as follows. In chapter 2, the fundamentals of the present numerical method are given. There exist a wide variety of methods referred to as "vortex methods". In order to clarify which of these numerical methods are used, and also to keep this thesis self-contained, the derivation of the discretized equations are shown in detail. A few illustrations are included to help realize the physical interpretation of the equations.

In chapter 3 the calculation of the homogeneous isotropic turbulence is discussed. Some numerical techniques are introduced to solve this particular flow, such as the periodic fast multipole method, and also the radial basis function interpolation. This chapter first concentrates on the time evolution of the kinetic energy spectrum, where the reproducibility of the energy cascade is examined. The focus then moves on to the decay of kinetic energy and enstrophy. The velocity derivative skewness and flatness are also examined to ascertain the soundness of higher order statistics. Subsequently, the dependence on spatial resolution and Reynolds number is studied, in order to generalize our observations. Following that, the spectral energy transfer is observed from a different perspective by plotting all terms of the energy spectrum equation. Finally, the effect of spatial adaptation is investigated for both viscous diffusion schemes.

In chapter 4 the calculation of the homogeneous shear flow is discussed. The shear periodic fast multipole method is introduced, and the vorticity equation is calculated in a perturbation form. Using this technique, the vortex method calculation of the homogeneous shear flow is performed and compared with a finite difference method. The focus of this section is on the ability of vortex methods to reproduce the anisotropy of turbulence, i.e. the ability of spherical vortex blobs to reproduce streaky global vortex structures. Another objective is the assessment of the production of turbulence in vortex methods, i.e. the validation of the vortex stretching term calculation for strongly strained flows.

In chapter 5 the calculation of the turbulent channel flow is discussed, along with some preliminary calculations for the laminar channel flow. The fast multipole method is once again extended to a periodic boundary condition with two periodic directions. Using this technique the vortex method calculation of a channel flow is performed and compared with a finite difference calculation using the same calculation conditions. First, the validity of the wall boundary condition for the vorticity is examined in the laminar channel flow. Following that a parameter study is performed for the turbulent channel flow.

In chapter 6 the overall conclusion is given, along with future prospects of vortex methods. Supplementary material are given in appendices A-D. Especially, a detailed explanation of the fast multipole method is given in appendix C.

Chapter 2

Vortex Method

2.1 Introduction

The vortex method solves the following set of equations.

$$\nabla^2 \mathbf{u} = -\nabla \times \boldsymbol{\omega}, \tag{2.1}$$

$$\frac{D\boldsymbol{\omega}}{Dt} = \boldsymbol{\omega} \cdot \nabla \mathbf{u} + \nu \nabla^2 \boldsymbol{\omega}, \tag{2.2}$$

where $\mathbf{u}$ is the velocity vector, $\boldsymbol{\omega}$ is the vorticity vector, and ν is the kinematic viscosity. When the velocity Poisson equation Eq. (2.1) is formulated as an integral equation using Green's functions, it yields the generalized Biot-Savart equation, as shown in section 2.2. In the present vortex method the vorticity equation Eq. (2.2) is solved in a fractional step manner by solving the first and second term on the right hand side separately. The details of the method for solving the first term (stretching term) is shown in section 2.3, while the method for solving the second term (diffusion term) is shown in section 2.4.

2.2 Biot-Savart Equation

The weighted residual formulation of Eq. (2.1) using the Green's function G as the weighting function becomes

$$\int_\Omega G \nabla^2 \mathbf{u} d\Omega = -\int_\Omega G(\nabla \times \boldsymbol{\omega}) d\Omega, \tag{2.3}$$

where Ω represents the entire calculation domain. The Green's function for the three dimensional Laplace equation is

$$G = \frac{1}{4\pi r}, \tag{2.4}$$

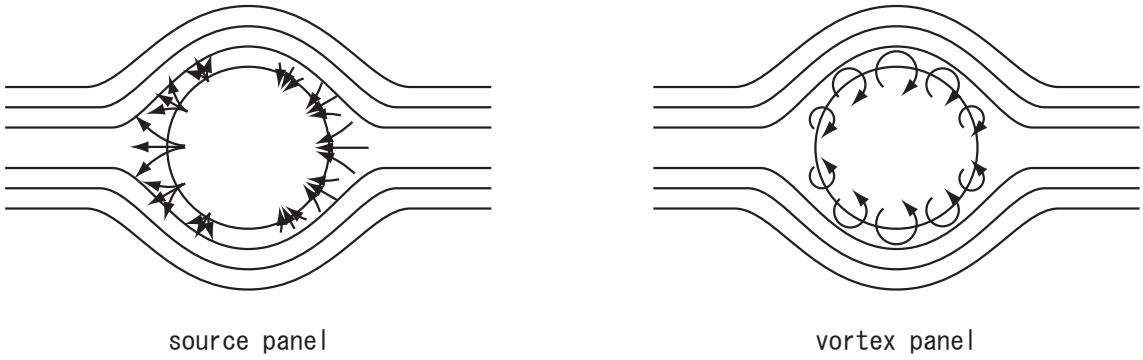

Figure 2.1: Boundary Element Solution of an Inviscid Flow Around a Circular Body

where r is the distance between two calculation points. After a little manipulation using vector analysis and the divergence theorem, we obtain

$$\int_\Omega \mathbf{u}\nabla^2 G d\Omega - \int_\Gamma [(\mathbf{n}\cdot\mathbf{u})\nabla G + (\mathbf{n}\times\mathbf{u})\times\nabla G] d\Gamma = -\int_\Omega \boldsymbol{\omega}\times\nabla G d\Omega + \mathbf{U}_\infty, \tag{2.5}$$

where Γ represents the boundary of the calculation domain, and $\mathbf{U}_\infty$ is the free stream velocity. See section A.3 of the appendix for details of the derivation. Due to the following properties of the Green's function

$$\begin{cases} \int_\Omega \nabla^2 G = 1, & \text{interior} \\ \int_\Omega \nabla^2 G = \dfrac{1}{2}, & \text{boundary} \\ \int_\Omega \nabla^2 G = 0, & \text{exterior} \end{cases} \tag{2.6}$$

Eq. (2.5) becomes

$$\frac{1}{2}\mathbf{u} - \int_\Gamma [\underbrace{(\mathbf{n}\cdot\mathbf{u})}_{\sigma}\nabla G + \underbrace{(\mathbf{n}\times\mathbf{u}+\boldsymbol{\omega})}_{\boldsymbol{\gamma}}\times\nabla G] d\Gamma = \mathbf{U}_\infty, \tag{2.7}$$

on the boundary of the calculation domain. This is solved by the boundary element method using either source panels (σ) or vortex panels ($\boldsymbol{\gamma}$). As an example, an illustration of the flow around a circular body solved by source panels and vortex panels is shown in Fig. 2.1.

Once the strength of the panels are calculated, the velocity at an arbitrary location in the domain can be calculated from

$$\mathbf{u} = \int_\Gamma [(\mathbf{n}\cdot\mathbf{u})\nabla G + (\mathbf{n}\times\mathbf{u})\times\nabla G] d\Gamma - \int_\Omega \boldsymbol{\omega}\times\nabla G d\Omega + \mathbf{U}_\infty. \tag{2.8}$$

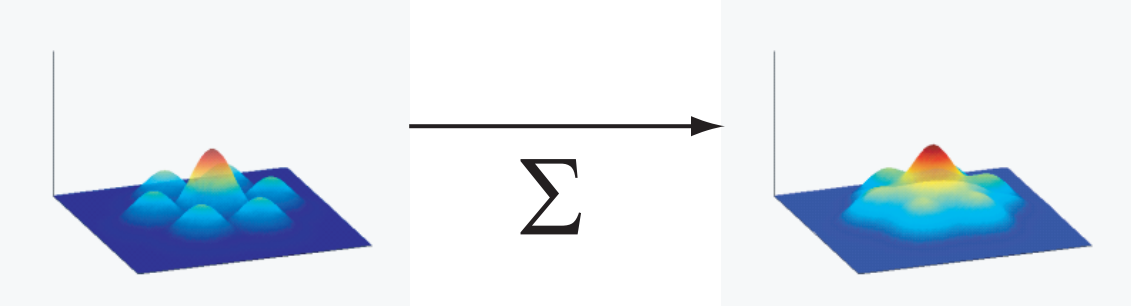

Figure 2.2: The Superposition of Gaussian Distributions

The boundary integral part is calculated by the boundary element method. Thus, the remaining task is to solve

$$\mathbf{u} = -\int_{\Omega} \boldsymbol{\omega} \times \nabla G d\Omega. \tag{2.9}$$

The vorticity field is discretized by using a superposition of Gaussian distributions.

$$\boldsymbol{\omega}_i = \sum_{j=1}^{N} \boldsymbol{\alpha}_j \zeta_\sigma, \tag{2.10}$$

where $\boldsymbol{\alpha}$ is the vortex strength and

$$\zeta_\sigma = \frac{1}{(2\pi\sigma_j^2)^{3/2}} \exp\left(-\frac{r_{ij}^2}{2\sigma_j^2}\right), \tag{2.11}$$

is the Gaussian smoothing function. r_{ij} is the distance between point i and point j. An image of what the superposition would look like, is shown in Fig. 2.2. Substituting Eq. (2.10) into Eq. (2.9) yields

$$\mathbf{u}_i = \sum_{j=1}^{N} \boldsymbol{\alpha}_j g_\sigma \times \nabla G, \tag{2.12}$$

where

$$g_\sigma = \operatorname{erf}\left(\sqrt{\frac{r_{ij}^2}{2\sigma_j^2}}\right) - \sqrt{\frac{4}{\pi}}\sqrt{\frac{r_{ij}^2}{2\sigma_j^2}} \exp\left(-\frac{r_{ij}^2}{2\sigma_j^2}\right). \tag{2.13}$$

erf(x) is the error function

$$\operatorname{erf}(x) = \frac{2}{\sqrt{\pi}} \int_0^x e^{-t^2} dt. \tag{2.14}$$

The complete form of the spatially discretized Biot-Savart equation is

$$\mathbf{u}_i = \sum_{j}^{N} \frac{\mathbf{r}_{ij} \times \boldsymbol{\alpha}_j}{4\pi r_{ij}^3} \left[\operatorname{erf}\left(\sqrt{\frac{r_{ij}^2}{2\sigma_j^2}}\right) - \sqrt{\frac{4}{\pi}}\sqrt{\frac{r_{ij}^2}{2\sigma_j^2}} \exp\left(-\frac{r_{ij}^2}{2\sigma_j^2}\right)\right]. \tag{2.15}$$

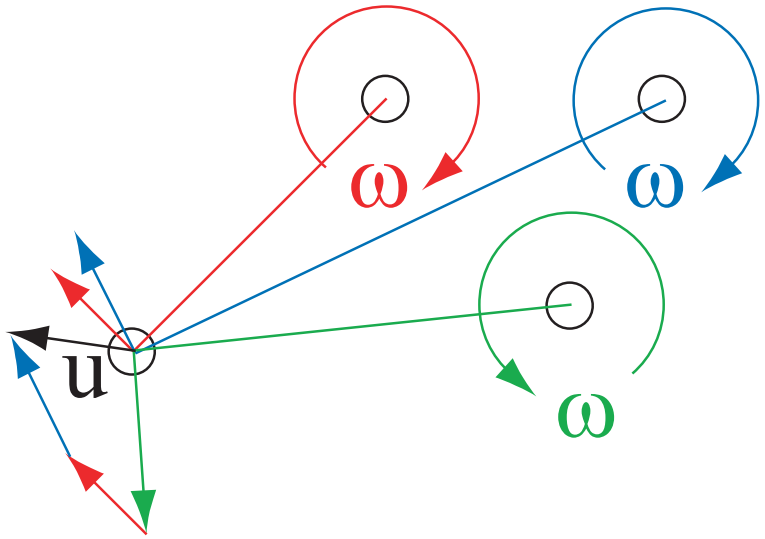

Figure 2.3: Graphical Representation of the Biot-Savart Equation

A schematic of what this equation physically represents, is shown in Fig. 2.3. Each pairwise interaction of elements induces a velocity perpendicular to the distance vector between the two elements. The velocity of an element is obtained by summing these individual velocity vectors.

2.3 Stretching Term

2.3.1 Formulation

Starting from the Navier-Stokes equation

$$\frac{\partial \mathbf{u}}{\partial t} + \mathbf{u} \cdot \nabla \mathbf{u} = -\frac{1}{\rho} \nabla p + \nu \nabla^2 \mathbf{u}, \tag{2.16}$$

and taking the curl, we obtain the vorticity equation,

$$\frac{\partial \boldsymbol{\omega}}{\partial t} + \mathbf{u} \cdot \nabla \boldsymbol{\omega} = \boldsymbol{\omega} \cdot \nabla \mathbf{u} + \nu \nabla^2 \boldsymbol{\omega}, \tag{2.17}$$

which is the Eulerian form. The vortex method solves this in the Lagrangian form

$$\begin{cases} \dfrac{D\boldsymbol{\omega}}{Dt} = \boldsymbol{\omega} \cdot \nabla \mathbf{u} + \nu \nabla^2 \boldsymbol{\omega}, \\ \dfrac{\partial \mathbf{x}}{\partial t} = \mathbf{u} \quad \left(\dfrac{D\mathbf{x}}{Dt} = 0 \right), \end{cases} \tag{2.18}$$

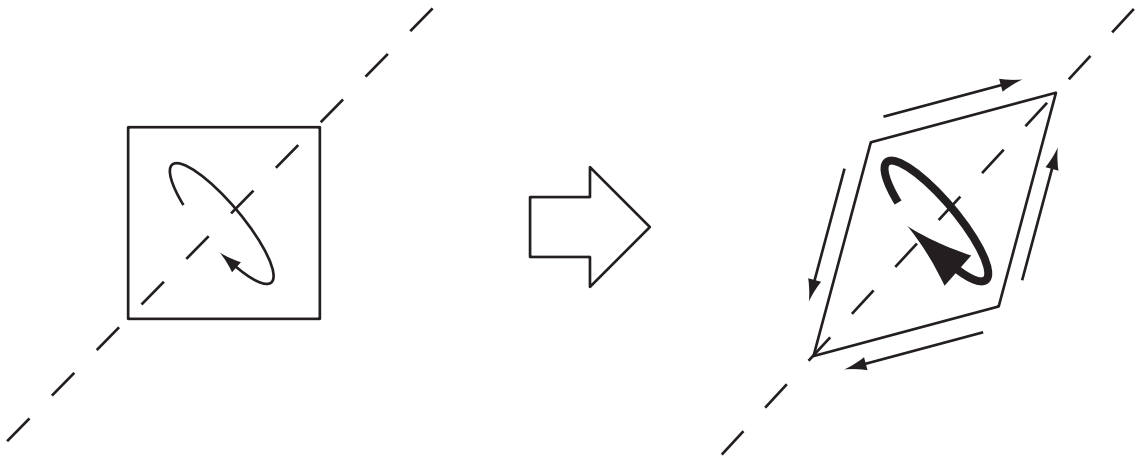

Figure 2.4: Graphical Representation of the Stretching Term

which corresponds to neglecting the convection term and moving the calculation points according to their local velocity. This section deals with the rate-of-change of vorticity caused by the stretching term,

$$\frac{D\boldsymbol{\omega}}{Dt} = \boldsymbol{\omega} \cdot \nabla \mathbf{u}. \tag{2.19}$$

By substituting Eq. (2.10) into this equation we obtain

$$\frac{D\boldsymbol{\alpha}_i}{Dt} = \boldsymbol{\alpha}_i \cdot \nabla \mathbf{u}_i. \tag{2.20}$$

Then substituting Eq. (2.12) results in

$$\frac{D\boldsymbol{\alpha}_i}{Dt} = \sum_{j=1}^{N} \boldsymbol{\alpha}_j \nabla(g_\sigma \times \nabla G) \cdot \boldsymbol{\alpha}_i \tag{2.21}$$

The complete form of the spatially discretized stretching term calculation is

$$\begin{aligned}\frac{D\boldsymbol{\alpha}_i}{Dt} = \sum_{j}^{N} \frac{\boldsymbol{\alpha}_i \times \boldsymbol{\alpha}_j}{4\pi r_{ij}^3} \left[\operatorname{erf}\left(\sqrt{\frac{r_{ij}^2}{2\sigma_j^2}}\right) - \sqrt{\frac{4}{\pi}} \sqrt{\frac{r_{ij}^2}{2\sigma_j^2}} \exp\left(-\frac{r_{ij}^2}{2\sigma_j^2}\right) \right] \\ + (\boldsymbol{\alpha}_i \cdot \mathbf{r}_{ij}) \frac{\boldsymbol{\alpha}_j \times \mathbf{r}_{ij}}{4\pi r_{ij}^5} \left[3\operatorname{erf}\left(\sqrt{\frac{r_{ij}^2}{2\sigma_j^2}}\right) - \left(\frac{r_{ij}^2}{\sigma_j^2} + 3\right) \sqrt{\frac{4}{\pi}} \sqrt{\frac{r_{ij}^2}{2\sigma_j^2}} \exp\left(-\frac{r_{ij}^2}{2\sigma_j^2}\right) \right].\end{aligned} \tag{2.22}$$

A schematic of what this equation physically represents, is shown in Fig. 2.4 The vorticity vector that is aligned with the principal axis of the shear is strengthened. This is the result of the conservation of angular momentum, while the fluid is being strained.

2.4 Viscous Diffusion

In this section, the methods to calculate the diffusion term

$$\frac{D\boldsymbol{\omega}_i}{Dt} = \nu\nabla^2\boldsymbol{\omega}_i, \tag{2.23}$$

are shown. This linear differential equation has an analytical solution

$$\boldsymbol{\omega}_i = \frac{\boldsymbol{\alpha}_j}{(4\pi\nu t)^{d/2}} \exp\left(-\frac{\mathbf{r}_{ij}^2}{4\nu t}\right). \tag{2.24}$$

However, this solution itself cannot be directly implemented in the vortex method because $\boldsymbol{\omega}$ is not a variable that the vortex elements possess. The diffusion must be represented by changing either σ, $\boldsymbol{\alpha}$, or $\mathbf{u}$, which are the variables that are assigned to the vortex elements. There are a wide variety of viscous diffusion schemes for vortex methods. Before giving a detailed description of the methods used in the present calculation, the possible candidates are briefly introduced.

2.4.1 Review of Viscous Diffusion Schemes

Generally, Eulerian methods have difficulties in solving convection but can easily handle diffusion, as to where Lagrangian methods can solve the convection in a straightforward manner but have a problem with diffusion. Thus, the extension of vortex methods to viscous flows has not been a straightforward task, and the diversity of methods has become quite large. The random vortex method (RVM) by Chorin [10] uses a stochastic interpretation of the diffusion equation. It has served an important role in the early development of viscous diffusion schemes, but its slow convergence rate prompted the development of alternative methods. The core spreading method (CSM) by Kuwahara & Takami [4] or Leonard [11] uses a deterministic approach, which changes the standard deviation of the Gaussian distribution of vorticity to match the fundamental solution of the diffusion equation. A straightforward implementation of this method lacks convergence due to the fact that the ever-expanding Gaussian distribution moves with the velocity at its center. Local spatial refinement [34] can circumvent this problem, though this will introduce a large amount of error without careful consideration [30][35].

The particle strength exchange (PSE) by Degond & Mas-Gallic [12] redistributes the strength among vortex elements by solving the integral equation of the Laplacian operator. The location of elements are used as quadrature points, thus requires them to be nearly uniform for an accurate calculation. In highly strained fields this is impossible

without frequent regridding, which will sacrifice the grid-free nature and also accumulate numerical diffusion error without careful selection of the interpolation scheme [36]. The vortex redistribution method (VRM) by Shankar & van Dommelen [37] also redistributes the strength of vortex elements but by solving an underdetermined system of equations to equate the truncated Taylor series of the new distribution with that of the exactly diffused vorticity. Although, restrictions of particle nonuniformity are not as severe as the PSE, it is obvious that a sufficient number must exist in the neighborhood. The insertion and merging of particles is still an open area of research, as is the case with splitting and merging particles in CSMs.

In most cases a vortex element has three properties, vortex strength, core radius, and velocity. The CSM changes the core radius, PSE and VRM change the vortex strength to account for diffusion. The diffusion velocity method by Ogami & Akamatsu [38] modifies the velocity instead, where the diffusion velocity becomes the product of $-\nu/\omega$ and the gradient of vorticity. For regions of zero vorticity the $-\nu/\omega$ becomes singular, so an algorithm which does not increase the vorticity magnitude outside of the computational vorticity support [39] is essential to this scheme. There exist many other ways to calculate the viscous diffusion of vorticity using a semi-Lagrangian discretization, such as the vortex in cell (VIC), free Lagrangian, triangulated, and moving least squares (MLS). The present study focuses on pure Lagrangian schemes (with spatial adaptation), thus semi-Lagrangian methods are out of scope.

In particular, two of these viscous diffusion schemes -the PSE and CSM- are selected. The PSE is favorable in the sense that, it permits the use of higher order kernels, does not require viscous splitting, and is a straightforward solution to the governing integral equation. It has also been successfully implemented in many applications. On the other hand, the CSM has the potential of becoming a pure Lagrangian scheme, despite its reputation it once suffered from. Unlike, other viscous diffusion methods the CSM does not require the use of any kind of mesh whatsoever, even for spatial adaptation. Furthermore, the spatial adaptation can be performed in a less ambiguous manner compared to the VRM.

The PSE and CSM contrast with each other in many aspects, starting from the physical property it changes, to the way it handles spatial adaptation of elements, as shown in Fig. 2.5. It is worth investigating how these differences affect the performance of the vortex method for the homogeneous isotropic turbulence. The details of the calculation method of the two schemes are discussed below.

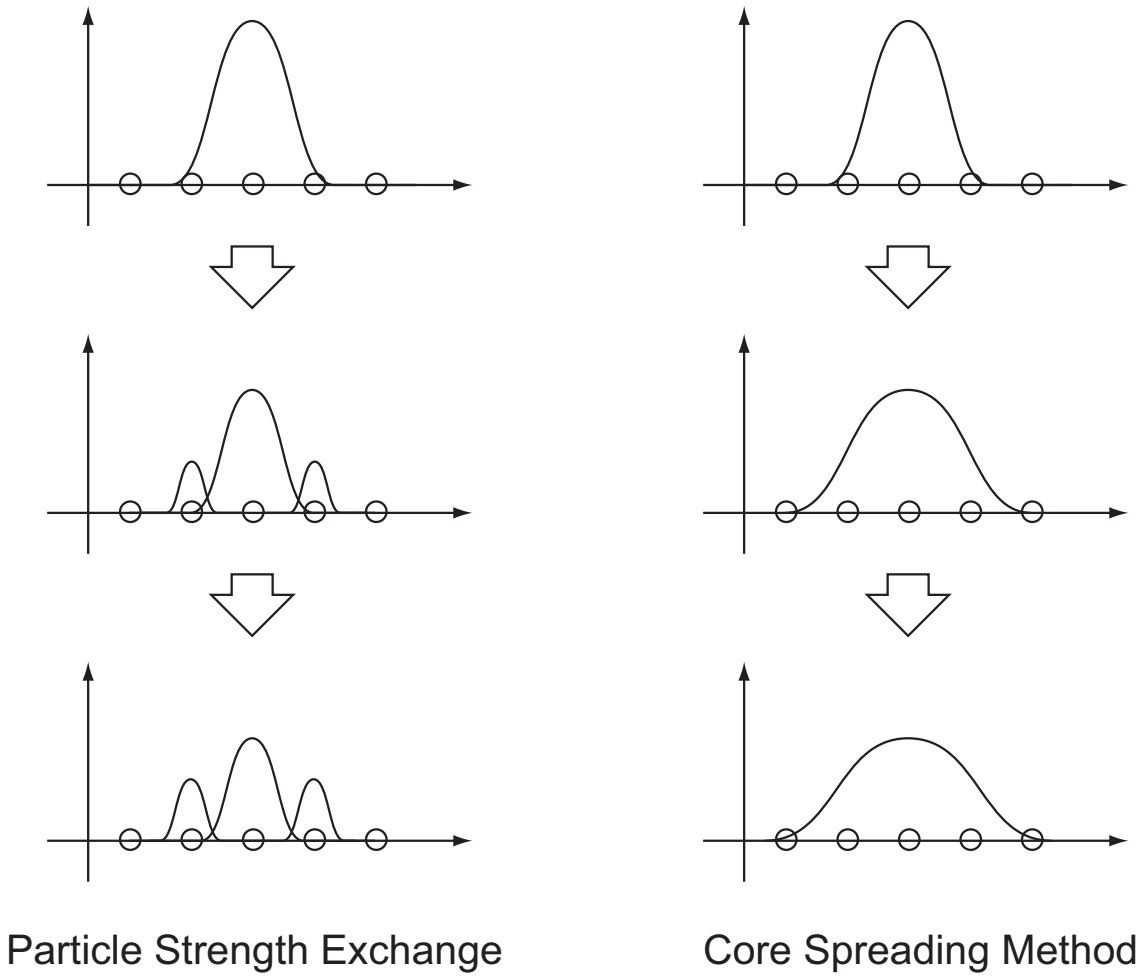

Figure 2.5: Difference of the PSE and CSM

2.4.2 CSM

By substituting Eq. (2.11) into Eq. (2.10), it can be seen that changing the variance of the Gaussian distribution according to

$$\sigma^2 = 2\nu t, \tag{2.25}$$

will result in the heat kernel Eq. (2.24). σ is often referred to as the core radius of the vortex blob, and represents the physical length scale of the vortex elements. The rate-of-change of the core radius is

$$\frac{D\sigma_i}{Dt} = \frac{\nu}{\sigma_i}. \tag{2.26}$$

A straightforward implementation of this method is non-convergent, because the core radius eventually becomes too large to represent the local fluid motion. Splitting the vortex elements into smaller ones [34] can circumvent this problem, though this will introduce a large amount of error without careful consideration. Furthermore, the number of elements required for an accurate splitting process becomes larger than the number of elements required to sufficiently resolve the flow.

Barba *et al.* proposed an alternative method [30], which uses the radial basis function interpolation to reproduce the field using smaller core sizes. In this case the number of elements remains constant. An example of the interpolation process is shown in Fig. 2.6. First, the vorticity field is calculated from Eq. (2.10). Then, the core radius σ is reduced to a sufficiently small size. Now the task is to recalculate the vortex strength $\boldsymbol{\alpha}$ to reproduce the original vorticity field. Eq. (2.10) can be viewed as a matrix vector multiplication of the form

$$\begin{bmatrix} \vdots \\ \boldsymbol{\omega}_i \\ \vdots \end{bmatrix} = \begin{bmatrix} \ddots & & \\ & \zeta_\sigma(r_{ij}) & \\ & & \ddots \end{bmatrix} \begin{bmatrix} \vdots \\ \boldsymbol{\alpha}_j \\ \vdots \end{bmatrix}. \tag{2.27}$$

This linear matrix equation can be solved for to obtain $\boldsymbol{\alpha}$. Since ζ_σ decays rapidly, the matrix in Eq. (2.27) is banded and easy to solve.

2.4.3 PSE

The PSE solves an integral equation for the Laplacian operator

$$\nabla^2 \boldsymbol{\omega}_i = \frac{2}{\sigma^2} \sum_j \eta_\sigma(\mathbf{r}_{ij})(\boldsymbol{\omega}_j - \boldsymbol{\omega}_i) V_j, \tag{2.28}$$

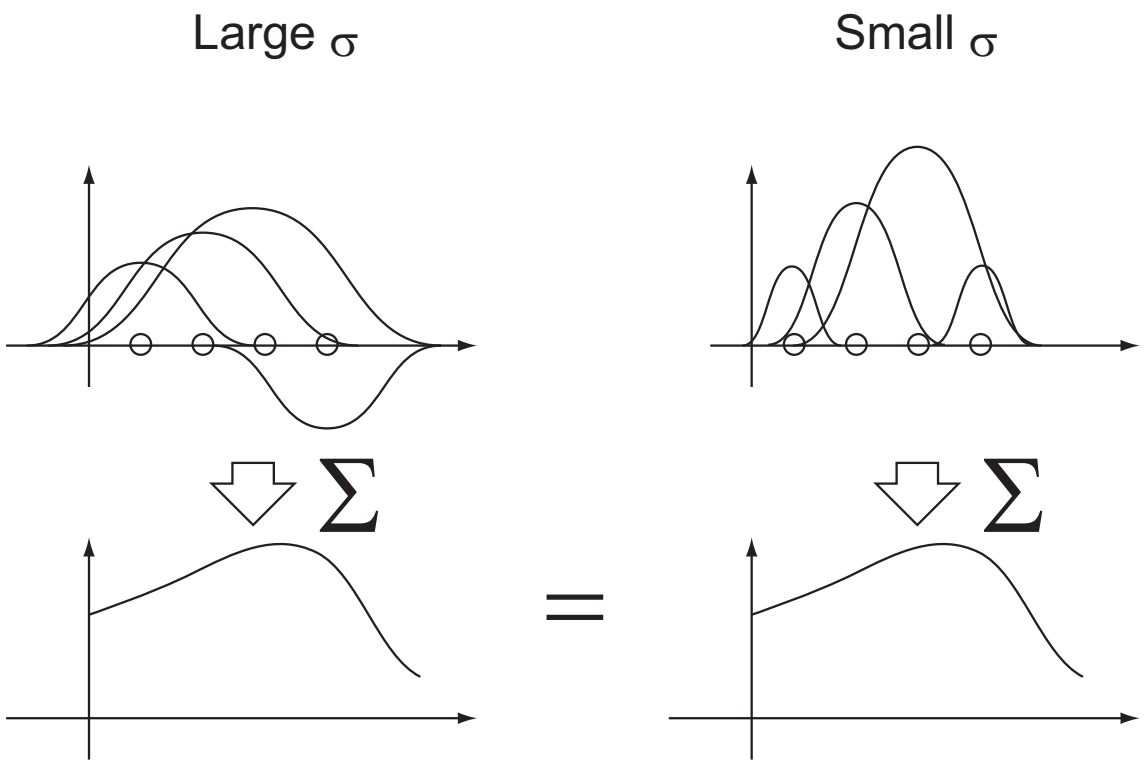

Figure 2.6: Reproducing the Vorticity Field Using Smaller Core Size

where V is the volume of the vortex element, and the PSE kernel is

$$\eta_\sigma = \frac{1}{(2\pi\sigma^2)^{d/2}} \exp\left(-\frac{\mathbf{r}_{ij}^2}{2\sigma^2}\right). \tag{2.29}$$

The Gaussian smoothing function Eq. (2.10) and Gaussian PSE kernel Eq. (2.29) are identical. So by assuming $\sigma^2 = 2\nu t$ the PSE kernel will also reduce to the heat kernel. However, unlike the CSM σ is not changed, but Eq. (2.28) and Eq. (2.29) are substituted into Eq. (2.23) to obtain the rate of change of the vortex strength

$$\frac{D\boldsymbol{\alpha}_i}{Dt} = \sum_j^N (V_i\boldsymbol{\alpha}_j - V_j\boldsymbol{\alpha}_i)\frac{2\nu}{\sigma_j^2}\frac{1}{(2\pi\sigma_j^2)^{3/2}} \exp\left(-\frac{r_{ij}^2}{2\sigma_j^2}\right), \tag{2.30}$$

As the vortex method calculation proceeds, the vortex elements become more and more disordered. This has a detrimental effect not only on the PSE diffusion calculation, but also the velocity and stretching calculations. Therefore, it is common to remesh the elements onto a uniform distribution every few timesteps. The interpolation is done by integrating the vortex strength of the elements near-by using a weighting function of the form

$$M_4'(x) = \begin{cases} 0, & \text{if } |x| > 2, \\ \frac{1}{2}(2-|x|)^2(1-|x|), & \text{if } 1 \le |x| \le 2 \\ 1 - \frac{5x^2}{2} + \frac{3|x|^3}{2}, & \text{if } |x| \le 1 \end{cases}. \tag{2.31}$$

This weighting function is plotted in Fig. 2.7

2.4.4 Time Stepping

In the present calculations, the second order Adams-Bashforth method is used for the time stepping to update all variables.

$$\mathbf{x}_i^{n+1} = \mathbf{x}_i^n + \frac{\Delta t}{2}\left(3\mathbf{u}_i^n - \mathbf{u}_i^{n-1}\right), \tag{2.32}$$

$$\boldsymbol{\alpha}_i^{n+1} = \boldsymbol{\alpha}_i^n + \frac{\Delta t}{2}\left(3\left.\frac{D\boldsymbol{\alpha}_i}{Dt}\right|_n - \left.\frac{D\boldsymbol{\alpha}_i}{Dt}\right|_{n-1}\right), \tag{2.33}$$

$$\sigma_i^{n+1} = \sigma_i^n + \frac{\Delta t}{2}\left(3\left.\frac{D\sigma_i}{Dt}\right|_n - \left.\frac{D\sigma_i}{Dt}\right|_{n-1}\right). \tag{2.34}$$

Although this method has stability issues in Eulerian methods, Lagrangian vortex methods do not share this problem. Without the stability problem, it is a second order method that requires only one calculation per time step. Other high order methods such as the Runge-Kutta require multiple calculations per time step.

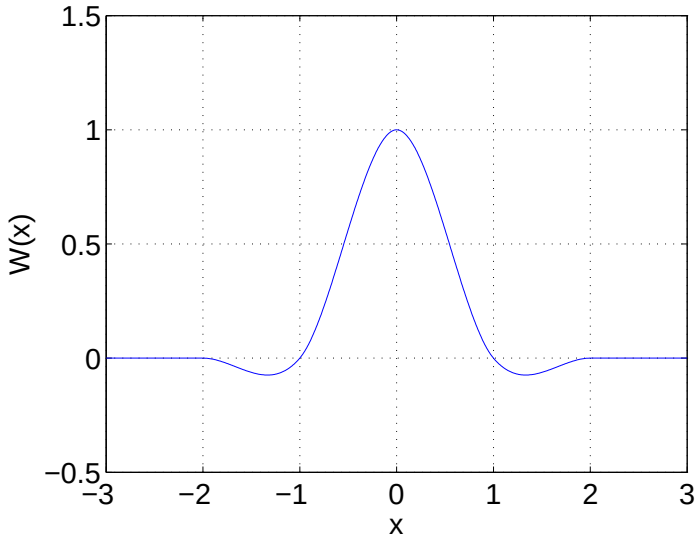

Figure 2.7: The M_4' Interpolation Kernel

2.5 Fast Multipole Method

The Biot-Savart and stretching calculation are accelerated by the fast multipole method (FMM). The details of the FMM are given in appendix C. Here, the final equations for the far field calculation are shown in the actual order that they are calculated. First, for the Biot-Savart equation.

1. Particle to Multipole Translation (P2M)

$$M_n^m = \sum_{j=1}^{N} \boldsymbol{\alpha}_j \rho_j^n Y_n^{-m}(\alpha_j, \beta_j), \tag{2.35}$$

2. Multipole to Multipole Translation (M2M)

$$M_n^m(0,0) = \sum_{k=-n}^{n} D_n^{km}(-\alpha, -\beta) M_n^k(\alpha, \beta), \tag{2.36}$$

$$M_j^k(0,0) = \sum_{n=0}^{j} \frac{\hat{M}_{j-n}^k(0,0) A_n^0 A_{j-n}^k \rho^n Y_n^0(0,0)}{(-1)^n A_j^k}, \tag{2.37}$$

$$M_n^m(\alpha,\beta) = \sum_{k=-n}^{n} D_n^{km}(\alpha, \beta) M_n^k(0,0). \tag{2.38}$$

3. Multipole to Local Translation (M2L)

$$M_n^m(0,0) = \sum_{k=-n}^{n} D_n^{km}(-\alpha,-\beta) M_n^k(\alpha,\beta), \tag{2.39}$$

$$L_j^k(0,0) = \sum_{n=0}^{p-1} \frac{\hat{M}_n^k(0,0) A_n^k A_j^k Y_{j+n}^0(0,0)}{(-1)^j A_{j+n}^0 \rho^{j+n+1}}, \tag{2.40}$$

$$L_n^m(\alpha,\beta) = \sum_{k=-n}^{n} D_n^{km}(\alpha,\beta) L_n^k(0,0). \tag{2.41}$$

4. Local to Local Translation (L2L)

$$L_n^m(0,0) = \sum_{k=-n}^{n} D_n^{km}(-\alpha,-\beta) L_n^k(\alpha,\beta), \tag{2.42}$$

$$L_j^k(0,0) = \sum_{n=j}^{p-1} \frac{\hat{L}_n^k(0,0) A_{n-j}^0 A_j^k \rho^{n-j} Y_{n-j}^0(0,0)}{A_n^k}, \tag{2.43}$$

$$L_n^m(\alpha,\beta) = \sum_{k=-n}^{n} D_n^{km}(\alpha,\beta) L_n^k(0,0). \tag{2.44}$$

5. Local to Particle Translation (L2P)

$$\mathbf{u}_i \approx \frac{1}{4\pi} \sum_{n=0}^{p-1} \sum_{m=-n}^{n} \left\{ \sum_{j=1}^{M} L_j \right\} \times \nabla R_i. \tag{2.45}$$

For the stretching calculation the equations are identical except for the first and final equations.

1. Particle to Multipole Translation (P2M)

$$M_n^m = \sum_{j=1}^{N} \boldsymbol{\alpha}_j \nabla \times \left\{ \rho_j^n Y_n^{-m}(\alpha_j,\beta_j) \right\}. \tag{2.46}$$

5. Local to Particle Translation (L2P)

$$\frac{D\boldsymbol{\alpha}_i}{Dt} \approx \frac{1}{4\pi} \sum_{n=0}^{p-1} \sum_{m=-n}^{n} \left(\sum_{j=1}^{M} L_j \right) (\boldsymbol{\alpha}_i \cdot \nabla R_i). \tag{2.47}$$

2.6 Summary

In summary, the present vortex method code calculates the following equations. Each vortex element holds seven variables (two vectors and one scalar); $\mathbf{x}, \boldsymbol{\alpha}, \sigma$. These variables are updated in the following order. First, it calculates the Biot-Savart equation to obtain the velocity induced on the vortex elements.

$$\frac{D\mathbf{x}_i}{Dt} = \sum_j^N \frac{\mathbf{r}_{ij} \times \boldsymbol{\alpha}_j}{4\pi r_{ij}^3} \left[\mathrm{erf}\left(\sqrt{\frac{r_{ij}^2}{2\sigma_j^2}} \right) - \sqrt{\frac{4}{\pi}} \sqrt{\frac{r_{ij}^2}{2\sigma_j^2}} \exp\left(-\frac{r_{ij}^2}{2\sigma_j^2} \right) \right].$$

Then, it solves the stretching term of the vorticity equation to obtain the rate-of-change of vortex strength.

$$\begin{aligned} \frac{D\boldsymbol{\alpha}_i}{Dt} = & \sum_j^N \frac{\boldsymbol{\alpha}_i \times \boldsymbol{\alpha}_j}{4\pi r_{ij}^3} \left[\mathrm{erf}\left(\sqrt{\frac{r_{ij}^2}{2\sigma_j^2}} \right) - \sqrt{\frac{4}{\pi}} \sqrt{\frac{r_{ij}^2}{2\sigma_j^2}} \exp\left(-\frac{r_{ij}^2}{2\sigma_j^2} \right) \right] \\ & + (\boldsymbol{\alpha}_i \cdot \mathbf{r}_{ij}) \frac{\boldsymbol{\alpha}_j \times \mathbf{r}_{ij}}{4\pi r_{ij}^5} \left[3\mathrm{erf}\left(\sqrt{\frac{r_{ij}^2}{2\sigma_j^2}} \right) - \left(\frac{r_{ij}^2}{\sigma_j^2} + 3 \right) \sqrt{\frac{4}{\pi}} \sqrt{\frac{r_{ij}^2}{2\sigma_j^2}} \exp\left(-\frac{r_{ij}^2}{2\sigma_j^2} \right) \right]. \end{aligned}$$

If the core spreading method is used as the diffusion scheme, the core radius is expanded by

$$\frac{D\sigma_i}{Dt} = \frac{\nu}{\sigma_i}.$$

Also, spatial adaptation is performed every few time steps, by recalculating the vortex strength of the vortex elements with smaller core radii by solving a system of equations for

$$\begin{bmatrix} \vdots \\ \boldsymbol{\omega}_i \\ \vdots \end{bmatrix} = \begin{bmatrix} \ddots & & \\ & \zeta_\sigma(r_{ij}) & \\ & & \ddots \end{bmatrix} \begin{bmatrix} \vdots \\ \boldsymbol{\alpha}_j \\ \vdots \end{bmatrix}.$$

If the particle strength exchange is used as the diffusion scheme, the rate-of-change of vortex strength is determined from

$$\frac{D\boldsymbol{\alpha}_i}{Dt} = \sum_j^N (V_i \boldsymbol{\alpha}_j - V_j \boldsymbol{\alpha}_i) \frac{2\nu}{\sigma_j^2} \frac{1}{(2\pi\sigma_j^2)^{3/2}} \exp\left(-\frac{r_{ij}^2}{2\sigma_j^2} \right),$$

Remeshing is performed every few time steps, by interpolating the vortex strength onto uniformly spaced vortex elements using

$$\boldsymbol{\alpha}_i = \sum_{j=1}^N \boldsymbol{\alpha}_j W(\mathbf{r}_{ij}),$$

where the $M4'$ interpolation kernel is used.

$$W(x) = \begin{cases} 0, & \text{if } |x| > 2, \\ \frac{1}{2}(2-|x|)^2(1-|x|), & \text{if } 1 \le |x| \le 2 \\ 1 - \frac{5x^2}{2} + \frac{3|x|^3}{2}, & \text{if } |x| \le 1 \end{cases}.$$

Finally, all variables are updated by the second-order Adams-Bashforth method

$$\begin{aligned} \mathbf{x}_i^{n+1} &= \mathbf{x}_i^n + \frac{\Delta t}{2}\left(3\frac{\partial \mathbf{x}_i^n}{\partial t} - \frac{\partial \mathbf{x}_i^{n-1}}{\partial t}\right), \\ \boldsymbol{\alpha}_i^{n+1} &= \boldsymbol{\alpha}_i^n + \frac{\Delta t}{2}\left(3\left.\frac{D\boldsymbol{\alpha}_i}{Dt}\right|_n - \left.\frac{D\boldsymbol{\alpha}_i}{Dt}\right|_{n-1}\right), \\ \sigma_i^{n+1} &= \sigma_i^n + \frac{\Delta t}{2}\left(3\left.\frac{D\sigma_i}{Dt}\right|_n - \left.\frac{D\sigma_i}{Dt}\right|_{n-1}\right). \end{aligned}$$

Chapter 3

Calculation of Isotropic Turbulence

3.1 Introduction

The simulation of turbulence requires the accurate prediction of the production, transport, and dissipation of kinetic energy. In vortex methods, this is made possible by properly calculating the stretching term and diffusion term of the vorticity equation. Although vortex methods have made remarkable advancements in the past decade, they still face numerous challenges, especially involving viscous diffusion schemes. The mesh-free nature of vortex methods itself is a large advantage, but it is also the primary source of this viscous diffusion problem. To solve these problems, numerous viscous diffusion schemes have been proposed during the past quarter century, along with spatial adaptation schemes to handle the distortion of particles. It is important to first validate these schemes in an environment, isolated from mean shear and near wall effects, but still complex enough to represent general turbulent behavior, i.e. the cascade and decay of kinetic energy. The homogeneous isotropic turbulence is an ideal test case in this sense, and has been used to validate grid based direct numerical simulations (DNS) in the past. The same can be done for vortex methods, as the first step toward developing a mesh-free but rigorous turbulence simulation.

Only a small number of vortex methods have been tested for the homogeneous isotropic turbulence. Cottet *et al.* [33] used the vortex-in-cell for the viscous diffusion scheme and compared with a spectral method for $N = 128^3$ grid points. The evolution of the energy spectrum, kinetic energy, dissipation, enstrophy and skewness were in excellent agreement. However, their method requires the use of a grid for the stretching and velocity calculations, leaving only the convection to be calculated using a Lagrangian discretization. Totsuka & Obi [32] compared the spectral method with

the vortex method using the core spreading method and a Laplacian model used in the moving particle semi-implicit (MPS), which is similar to the redistribution method in vortex methods. All calculations are performed in 2-D and no spatial refinement is used in the core spreading method. They use a particle insertion and merging technique for the MPS Laplacian method and the energy spectrum agrees with the spectral method for this case. Since the stretching term does not exist in the 2-D vorticity equation, their calculation can be thought of as an assessment of the diffusion term only. It is necessary to extend this to a 3-D flow and evaluate the balance between stretching and dissipation, in order to validate both the cascade and dissipation of kinetic energy in vortex methods.

The absence of vortex method applications to homogeneous isotropic turbulence can be explained by its comparative inefficiency for this particular flow. The calculation cost becomes high compared to spectral methods because vortex methods do not benefit from periodic boundary conditions, whereas the spectral methods enormously do. Even with the use of fast algorithms, the speed of a N-body calculation is several orders lower than a grid based fast Poisson solver as noted by Cottet *et al.* [33]. However, the vortex method would become advantageous for external flows, where the vorticity is confined to a finite region near the wall.

In the present study, an acceleration technique for the Biot-Savart calculation in a periodic domain is developed and validated. With the help of this acceleration technique, the 3-D isotropic turbulence is calculated using the vortex method. A spectral method calculation using the same number of elements N, Reynolds number Re_λ and initial condition, is used as a reference. The particle strength exchange (PSE) and core spreading method (CSM) are selected as viscous diffusion schemes for the vortex method to consider both possibilities. This study first concentrates on the time evolution of the kinetic energy spectrum, where the reproducibility of the energy cascade is examined. Our focus then moves on to the decay of kinetic energy and enstrophy. The velocity derivative skewness and flatness are also examined to ascertain the soundness of higher order statistics. Subsequently, the dependence on spatial resolution and Reynolds number is studied, in order to generalize our observations. Following that, the spectral energy transfer is observed from a different perspective by plotting all terms of the energy spectrum equation. Finally, the effect of spatial adaptation is investigated for both viscous diffusion schemes.

3.2 Numerical Method

3.2.1 Spectral Method for Isotropic Turbulence

The spectral Galerkin method with primitive variable formulation is used in the present study. When the pressure term is eliminated by considering the pressure Poisson equation in wave space, we have

$$\hat{\mathbf{u}}_{\mathbf{k}}^{n+1} = \hat{\mathbf{u}}_{\mathbf{k}}^{n} - \Delta t \nu k^2 \hat{\mathbf{u}}_{\mathbf{k}}^{n} - \Delta t \widehat{(\mathbf{u}^n \cdot \nabla \mathbf{u}^n)}_{\mathbf{k}} + \Delta t \frac{\mathbf{k}}{k^2} \left[\mathbf{k} \cdot \widehat{(\mathbf{u}^n \cdot \nabla \mathbf{u}^n)}_{\mathbf{k}} \right]. \tag{3.1}$$

This is the actual equation which is solved, where $\hat{\mathbf{u}}_{\mathbf{k}}$ is the velocity in wave number space, $\mathbf{k}$ is the wave number vector. A pseudo-spectral method was used to compute the convolution sums, and the aliasing error was removed by the 3/2-rule. The time integration was performed using the fourth order Runge-Kutta method for all terms. No forcing was applied to the calculation, since it would be difficult to do so with vortex methods.

3.2.2 Initial Condition for Isotropic Turbulence

The initial condition was generated in Fourier space as a solenoidal isotropic velocity field with random phases and a prescribed energy spectrum

$$E \sim k^4 \exp\left(-\frac{2k^2}{k_p^2}\right), \tag{3.2}$$

and transformed to physical space [41]. $k_p = 4$ is the peak wave number. The grid points are equally spaced and the calculation domain is $[0, 2\pi]^3$. The resulting initial velocity field has a Gaussian distribution and zero mean. The spectral method calculation uses this initial condition directly.

The initial condition of the vortex method is generated as follows. First, the vortex elements are placed at the grid points. The vorticity at the grid points are calculated from the initial velocity field using a fourth order central difference method. The strength of the vortex elements were calculated from this vorticity by solving a system of equations by using a method described in section 3.3.6. The core radius of the vortex elements are set to $2\pi/N$ and the overlap ratio is 1.

The vortex method calculation is performed without the use of a grid. The velocity and stretching term calculation are performed by the periodic FMM. The diffusion is calculated by either updating the cutoff radius or vortex strength for the CSM and PSE, respectively. The PSE calculation is embedded in the direct calculation part of the

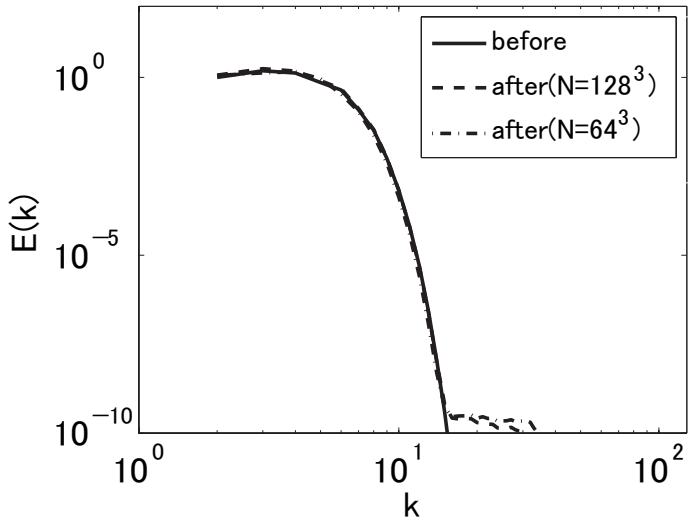

Figure 3.1: Energy Spectrum Before and After Initialization

periodic FMM stretching routine. The position, vortex strength and cutoff radius are updated by a second order Adams-Bashforth method. Vortex elements are convected according to the periodic boundary condition, thus if an element moves out from one side it comes in from the opposite side. For the energy spectrum calculation of the vortex method, the velocity on the grid is calculated using the Biot-Savart law, and then transformed to wave number space.

The accuracy of this initialization procedure is confirmed by comparing the energy spectrum before and after the initialization. If this error turns out to be negligible compared to the error in the vortex method itself, it would be fair to say that our measures for initialization and energy spectrum calculation are adequate for the present investigation.

In Fig. 3.1 the kinetic energy spectrum before and after the initialization procedure are shown for different spatial resolutions. The total error involved in steps 2 and 4 are small enough to produce a strict correspondence with the prescribed energy spectrum for a range of $E(k)$ that spans 10 digits. It is shown in the following section that the errors associated with the vortex method calculation itself are much larger than this.

3.2.3 Periodic Boundary Condition

The calculation of homogeneous isotropic turbulence assumes periodicity in all directions. In the present study the FMM is modified to include the effect of periodic boundary conditions. Previous attempts to use the FMM in a periodic domain have a $3^k \times 3^k \times 3^k$

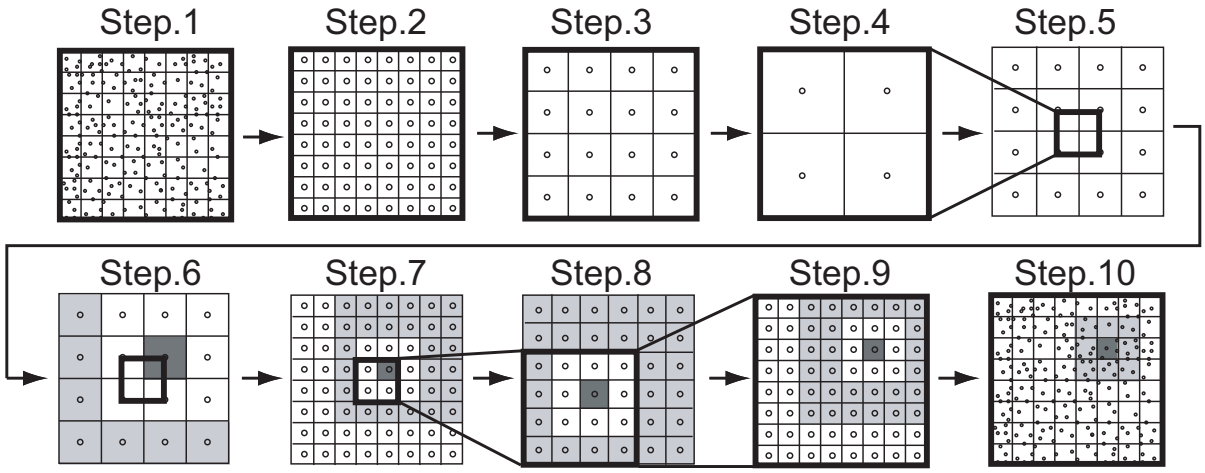

Figure 3.2: Flow of periodic FMM calculation

structure [42], where k is the number of periodic image cells per dimension. The present method forms a $2^k \times 2^k \times 2^k$ structure, by grouping the cells in the following manner.

A schematic of the flow of calculation is shown in Fig. 3.2. The heavy black line represents the original domain without periodic images. Although the figures are in 2-D, they represent 3-D structures. In step 1, the original calculation domain is repeatedly divided into smaller cells until the optimum level is reached. In step 2, the multipole moments are calculated for each cell. In steps 3,4, and 5, the cells are repeatedly grouped, and the multipole moments are shifted to the center of the larger cells. The only difference between our method and the one by Lambert *et al.* [42] is how the periodic image cells are grouped at step 5. Their method groups the original domain into one cell, and forms a $3^k \times 3^k \times 3^k$ structure thereafter. The present method forms a $2^k \times 2^k \times 2^k$ structure by leaving the original domain divided, while grouping with the outer cells. By doing so, the original oct-tree structure of the FMM is retained throughout the entire calculation. Thus, the complexity and error bounds directly follow that of the original FMM, and will not be shown here.

In step 6, the multipole moments are translated to local moments for non-neighboring cells. For example, the local moments of the dark grey cell are calculated from the multipole moments of the light grey cells. In steps 7, 8, and 9, the cells are repeatedly divided, and the local moments are translated to the center of these cells. The multipole moments of the newly non-neighboring cells (shown in light grey) are also translated to the divided cells (shown in dark grey). Finally, the effect of the neighboring cells at the optimum level are directly calculated at step 10.

The spectral method solves the Navier-Stokes equation in Fourier space Eq. (3.1),

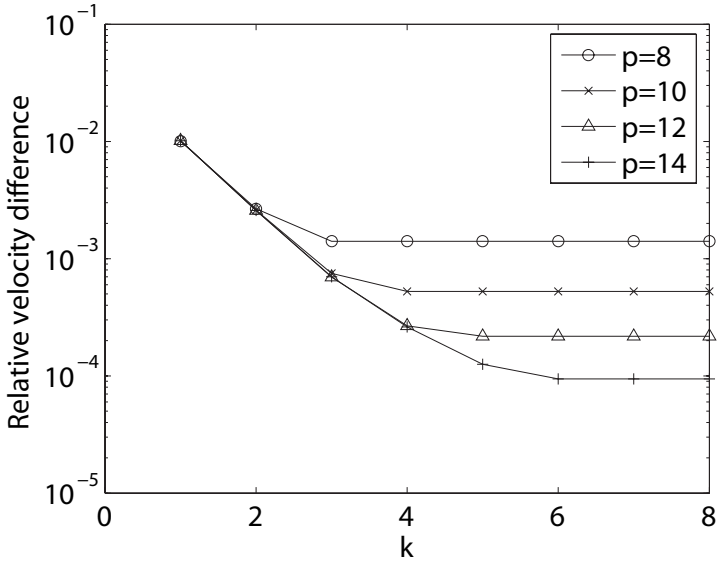

Figure 3.3: Relative error of the Biot-Savart calculation using periodic FMM for a different number of periodic image cells

and considers the periodic boundary conditions exactly. On the other hand, the periodic FMM is an approximation, where the accuracy can be controlled by adjusting the number of periodic image cells $2^k \times 2^k \times 2^k$, and the order of multipole expansion p.

We will examine how the accuracy of the periodic boundary approximation is affected by the number of periodic image boxes, and also the order of the multipole expansion. This is done by placing $N = 100$ particles with random coordinates and random vortex strength within a $[-\pi, \pi]^3$ domain and calculating for the $2^k \times 2^k \times 2^k$ periodic images using the periodic FMM. The result of the direct calculation for $k = 8$ is used as a reference value. The results for different orders of multipole expansion p are shown in Fig. 3.3. The relative velocity difference is calculated by taking the root mean square of the velocity difference at each point. The relative velocity error decreases as k is increased until it reaches the accuracy limit of the FMM for the given order of multipole expansions p. For the present calculations $p = 10$ and $k = 4$ are selected, so that the relative velocity difference is lower than 10^{-3}.

The periodic FMM calculation for the test cases shown above took only a few seconds. For the actual calculation of isotropic turbulence the number of particles can reach $N = 128^3$. The FMM Biot-Savart calculation for the unit cell without periodic images takes around 100 seconds for a problem of this size. Since the calculation cost of the periodic image cells remains constant regardless of N, the additional effort to include

periodic effects is less than 3% of the total. Lambert *et al.* [42] mention that their method takes about $25 - 30\%$ more time to compute the periodic effects for $N = 10^5$. For this N, our method would have a similar percentage.

3.3 Results and Discussion

3.3.1 Isosurface of the Second Invariant

The qualitative difference between the spectral method and the vortex method is compared by observing the isosurface of the second invariant of the velocity derivative tensor, otherwise known as the Q criterion. By setting Q to a negative value, it is possible to extract the vortical structures in the isotropic turbulence. The isosurface for $Q = -0.5$ for the spectral method and the vortex method using the PSE and CSM are shown in Fig. 3.4. There is little difference between the three methods. The position and shape of the vortical structures match quite well.

3.3.2 Energy Spectra and Statistics

The transfer and dissipation of kinetic energy determines the shape of the energy spectrum. Therefore, if the vortex method is unable to calculate either of these correctly, it would immediately result in a discrepancy in the energy spectrum. The results are presented for a calculation having an initial Re_λ of 25 and number of elements $N = 64^3$. The time increment is $\Delta t = 0.005$ for all calculations, including the spectral method. This corresponds to a quarter of the Kolmogorov time scale, and the Courant number $u\Delta t/\Delta x$ never exceeds 0.5. No spatial refinement is performed for these calculations. The effect of spatial refinement will be considered for the PSE and CSM separately in sections 3.3.5 and 3.3.6, respectively.

The kinetic energy, enstrophy and velocity derivative moments are calculated from

$$K = \frac{1}{2}u_i^2, \tag{3.3}$$

$$\zeta = \omega_i^2, \tag{3.4}$$

$$F_n = \frac{\overline{(\partial u_1/\partial x_1)^n}}{\overline{(\partial u_1/\partial x_1)^2}^{\frac{1}{2}n}}. \tag{3.5}$$

Also, the integral scale, Taylor's micro scale, micro scale Reynolds number, and eddy

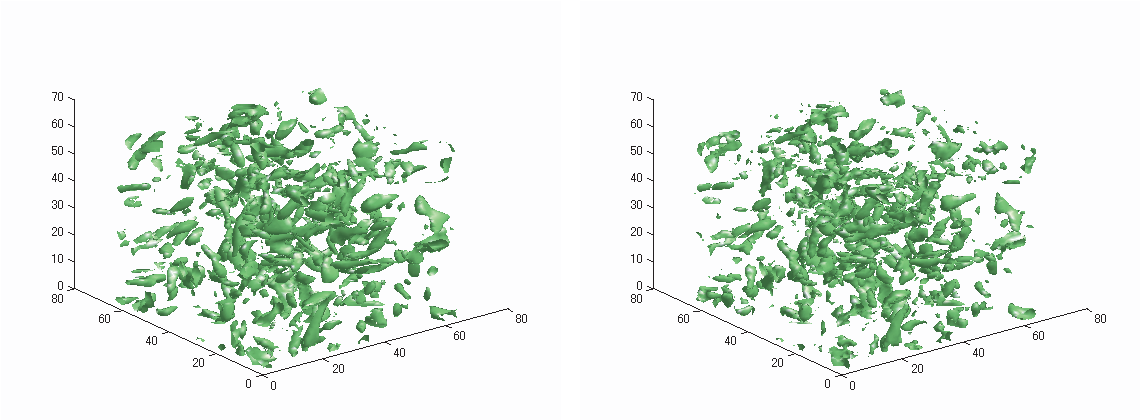

(a) *SGM* (b) *PSE*

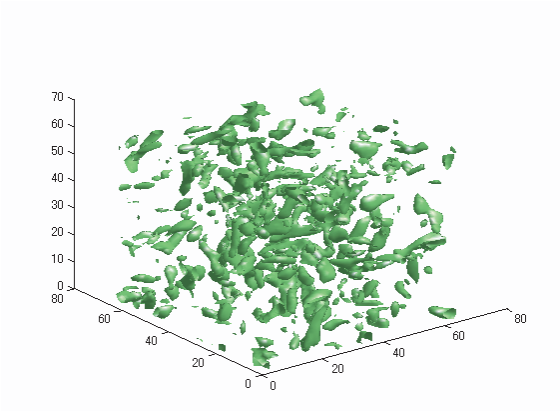

(c) *CSM*

Figure 3.4: Isosurface of the second invariant $Q = -0.5$

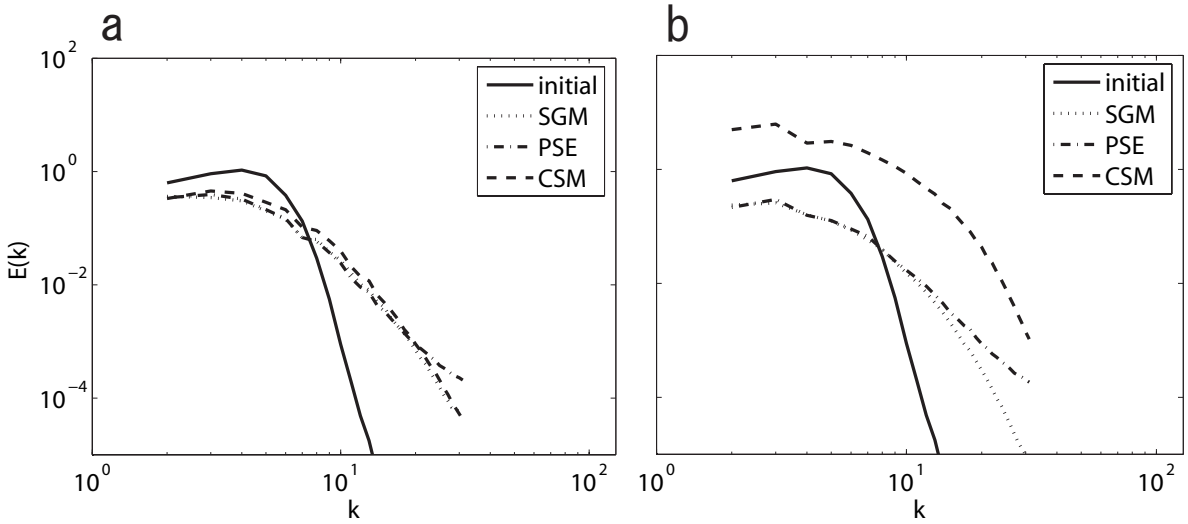

Figure 3.5: Kinetic Energy Spectra for $Re_\lambda = 25$, $N = 64^3$. (a) Spectra at $t/T = 2$. (b) Spectra at $t/T = 4$.

turnover time have the following relation.

$$L = \frac{\pi}{2u'^2} \int k^{-1} E(k) dk, \tag{3.6}$$

$$\lambda = \sqrt{15\nu u'^2/\epsilon}, \tag{3.7}$$

$$Re_\lambda = u'\lambda/\nu, \tag{3.8}$$

$$T = L/u'. \tag{3.9}$$

where $u' = \frac{2}{3}K$. The kinetic energy spectra for different times are shown in Fig. 3.5. The time t/T is in eddy turnover units, where $T = 0.25$. 'SGM', 'PSE', and 'CSM' stand for the spectral Galerkin method, particle strength exchange, and core spreading method, respectively. Note that the scaling of the vertical axis is different from Fig. 3.1, indicating that the initialization error is negligible for these calculations.

All energy spectra start out from the prescribed initial spectrum, and rapidly cascade the energy down to the higher wave numbers at the earlier stages of the calculation. Once the higher wave numbers contain a certain amount of energy, the entire spectrum gradually decays. At $t/T = 2$ the three methods behave quite similarly. However, at $t/T = 4$ the CSM spectrum is about two orders of magnitude larger than the other two. Also, the PSE shows a jump at the tail of the spectrum. For these calculations the Kolmogorov scale is $\eta \approx 0.05$ and the wave number corresponding to this scale is $k \approx 20$. It can be seen that the PSE is very close to matching the SGM up to this wave number.

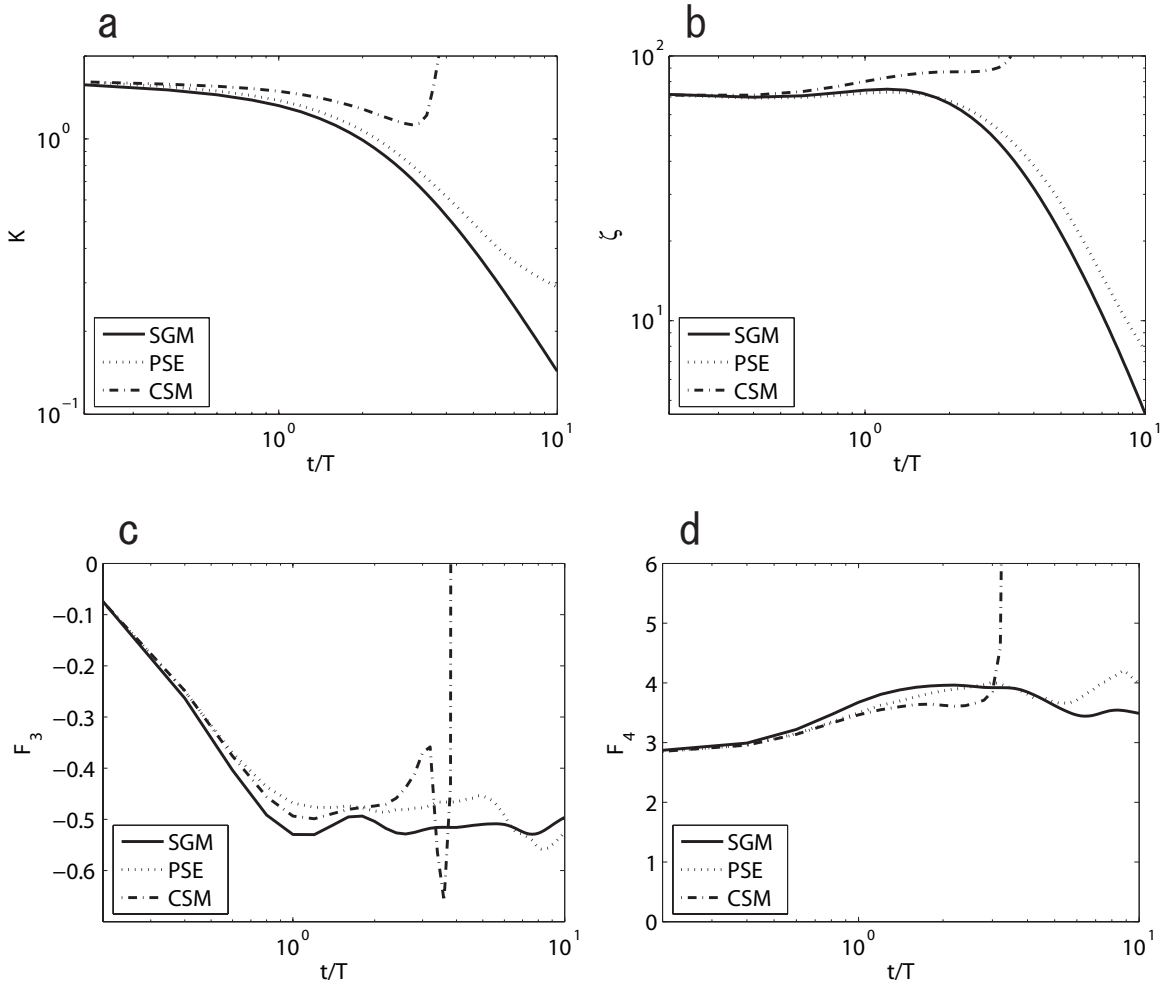

Figure 3.6: Statistical Properties for $Re_\lambda = 25$, $N = 64^3$. (a) Kinetic energy. (b) Enstrophy. (c) Skewness. (d) Flatness.

The energy spectrum alone is insufficient for the justification of our methods. The errors accumulating in the vortex method calculation become clear in the following time evolution plots. In Fig. 3.6 the time evolution of kinetic energy, enstrophy, velocity derivative skewness and flatness are shown. Their initial values are the same, but gradually diverge. The kinetic energy and enstrophy are known to show self-similar behavior at the final period of isotropic decay. This should result in a linear gradient at the end of these log-log plots. For the kinetic energy, only the SGM shows such behavior. The PSE fails to decay the kinetic energy properly at later time steps. The CSM decays only slightly, until the calculation starts to diverge at $t/T \approx 3$. For the enstrophy, the PSE shows self-similar behavior, whereas the CSM does not even decrease. The skewness and flatness of the velocity derivative behave similarly for the PSE and SGM. The CSM is able to reproduce the initial drop in the skewness but behaves strangely just prior to the blow up. Judging from the results of forced simulations for similar Re_λ by Jimenez *et al.* [43] and also Pumir [44] the skewness and flatness should reach values somewhere between $0.45 - 0.49$ and $3.5 - 4.0$, respectively. In this sense, the PSE estimates the velocity derivative moments quite well, while the flatness of the CSM prior to the blow up seems to be considerably small compared to the above mentioned criteria.

3.3.3 Spatial Resolution and Reynolds Number Dependence

So far, our knowledge of the performance of vortex methods is limited to a certain Reynolds number, and certain spatial resolution. One would naturally think that increasing the spatial resolution while retaining the Reynolds number would reduce the discretization errors in the calculation. Conversely, there should exist a maximum Reynolds number for which the vortex method can accurately calculate for a given number of elements. These two issues are inextricably linked, and should be investigated simultaneously.

The Reynolds number of the flow is doubled by quadrupling the strength of the prescribed energy spectrum in Eq. (3.2). Hence, the initial velocity fluctuation is doubled and the viscosity is unchanged. Also, the time increment is halved to account for the increase in the velocity magnitude in high Re_λ cases.

The kinetic energy spectra for 4 different cases are shown in Fig. 3.7. As mentioned earlier, the Kolmogorov wave length is $k \approx 20$ for $Re_\lambda = 25$. For $Re_\lambda = 50$ it is $k \approx 30$. The spectrum of the PSE diverges from the SGM at a wave number higher than the Kolmogorov wave number for all calculation conditions except $Re_\lambda = 50$, $N = 64$. Furthermore, increasing the spatial resolution shifts the bifurcation point of the PSE to

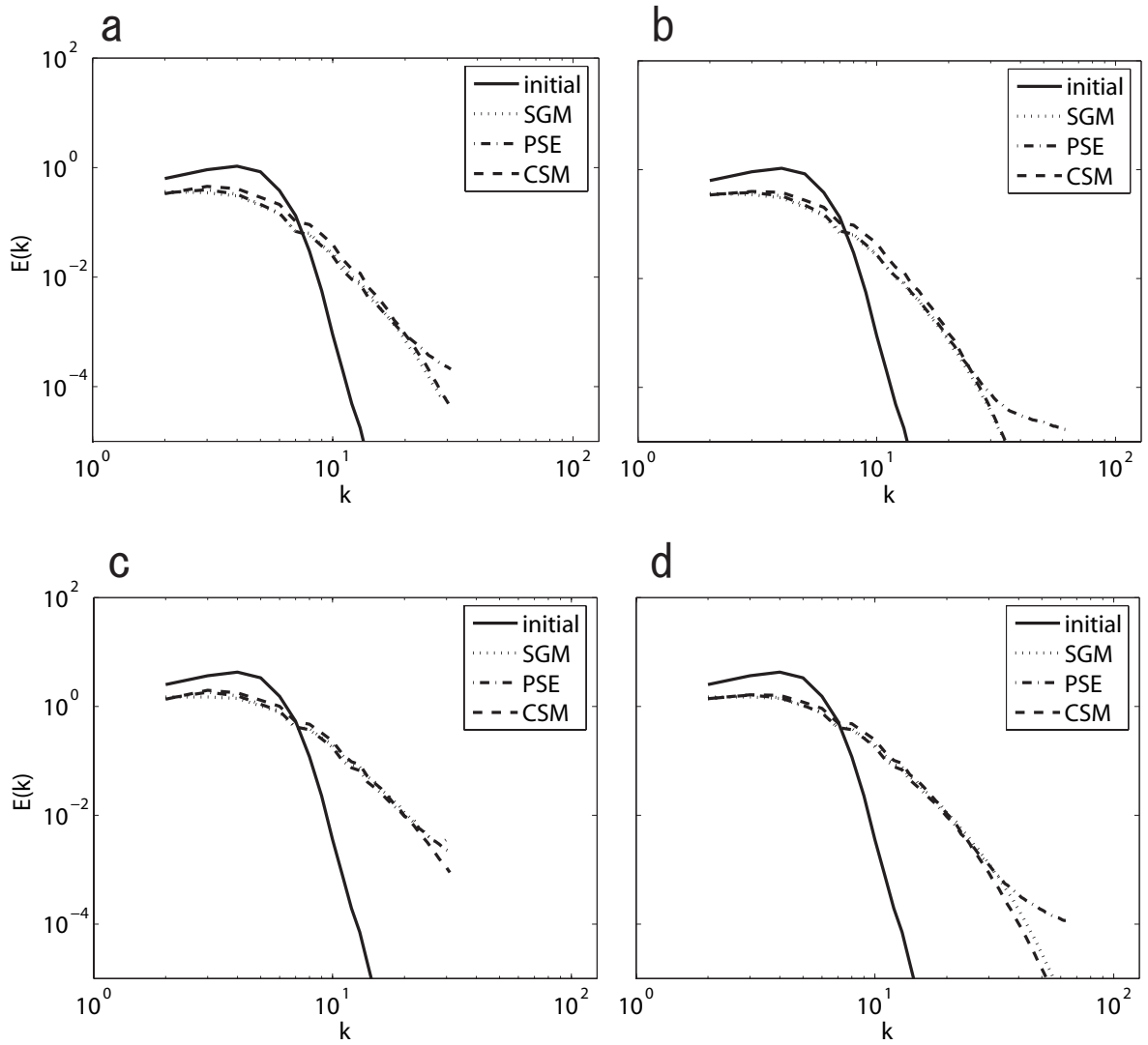

Figure 3.7: Kinetic Energy Spectra at $t/T = 2$. (a) $Re_\lambda = 25$, $N = 64$. (b) $Re_\lambda = 25$, $N = 128$. (c) $Re_\lambda = 50$, $N = 64$. (d) $Re_\lambda = 50$, $N = 128$.

a higher wave number. On the other hand, it is difficult to tell from these plots whether or not the CSM results are improved for higher spatial resolution calculations.

The decay of kinetic energy for the 4 different cases are shown in Fig. 3.8. The CSM calculation diverges at $t/T \approx 3$ for all 4 conditions. For the most poorly resolved case (c), the PSE also diverges at around the same time. At this Re_λ and N even the SGM should be slightly under-resolved but it does not diverge. These results indicate that the vortex methods require more computation elements compared to spectral methods, in order to calculate high Reynolds number flows stably. It is also clear that the results of the PSE do not improve when the spatial resolution is increased.

By looking at the four cases of $Re_\lambda = 25, 50$ and $N = 64^3, 128^3$ in a comprehensive manner, the following observations can be made. First, the CSM is indeed valid for a short time $t/T = 2$ and predicts the energy spectrum, kinetic energy and enstrophy decay, and also the initial drop of the velocity derivative skewness reasonably well during this finite time span. The length of this time is independent of Re_λ and N, since all calculations diverge at $t/T = 3$. Therefore, it is suspected that the divergence occurs when the overlap ratio $\sigma/\Delta x$ exceeds a certain limit, since its value is kept equal for all calculation conditions. Hence, the overlap ratio is bounded by a minimum and maximum value, and requires further investigation to ascertain the presence of an optimum range. This optimum range can then be used to obtain the frequency of spatial adaptation in CSMs. This issue will be considered further in section 3.3.6 along with the effect of spatial adaptation.

Another comprehensive observation is that the PSE agrees well with the SGM for large time steps and for most configurations, except the most poorly resolved case ($Re_\lambda = 50$, $N = 64^3$). Furthermore, the PSE yields higher accuracy when the spatial resolution is increased, and for these cases it matches the energy spectrum of the SGM up to the Kolmogorov wave number for a significantly long time. This fact alone demonstrates the high accuracy of the PSE vortex method. Though, a few problems remain unsolved. It has been shown that the insufficient decay rate of the kinetic energy in PSE calculations persists for all calculation conditions. Based on the observations of the 2-D isotropic turbulence calculation [32], where the decay rate of the kinetic energy matched that of the 2-D spectral method, the problem is likely to be the vorticity stretching term calculation, which is unique to a 3-D calculation. In the next section the spectral energy transfer is evaluated, in order to look at the stretching term error from a different perspective.

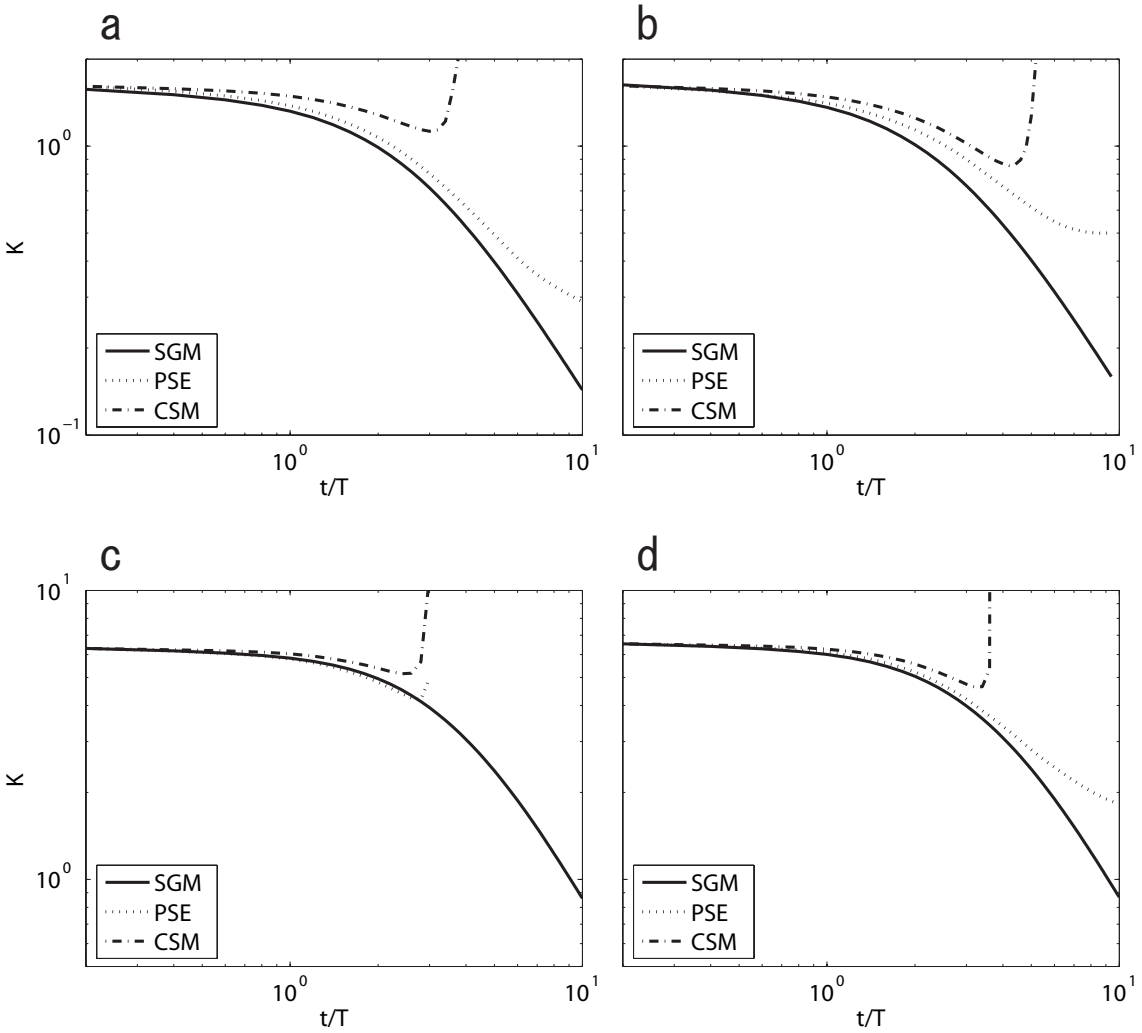

Figure 3.8: Kinetic Energy Decay. (a) $Re_\lambda = 25$, $N = 64$. (b) $Re_\lambda = 25$, $N = 128$. (c) $Re_\lambda = 50$, $N = 64$. (d) $Re_\lambda = 50$, $N = 128$.

3.3.4 Spectral Energy Transfer

Our main concern is how accurately the vortex method can predict the energy cascade. Plotting the energy spectra is one way to observe this. A more straightforward procedure to evaluate the spectral energy transfer would be to plot each term in the energy spectrum equation. In an isotropic turbulence the pressure terms drop out to yield,

$$\frac{\partial E}{\partial t}(k,t) = T(k,t) - 2\nu k^2 E(k,t). \tag{3.10}$$

The first term on the right hand side is the transfer term, which expresses the amount of energy being transferred between the wave numbers. The second term is the dissipation term, which accounts for the energy being dissipated at that particular wave number. The balance of these two determine the rate of change in kinetic energy contained in each wave number.

The terms of the energy spectrum equation for $Re_\lambda = 25$, $N = 64^3$ at $t/T = 2$ are plotted in Fig. 3.9. It is impossible to plot for later times because the CSM diverges shortly after this time. Plots (a)-(c) show the balance of the 3 terms for each method. Although there are some quantitative discrepancies between the 3 plots, the qualitative behavior is quite similar. The transfer term T is negative at lower wave numbers and positive at higher wave numbers, indicating that the energy is being cascaded to smaller scales. At the higher wave numbers the dissipation term has a negative peak and indicates that the kinetic energy is dissipated at smaller scales. The fact that Fig. 3.9 (c) shows a large quantitative discrepancy between the CSM and the other two methods cannot be neglected. Investigating the terms of the energy spectrum equation has reveled further problems in the CSM, but does not clarify the insufficient decay rate of the PSE.

3.3.5 Spatial adaptation in PSE

As the vortex method calculation proceeds, the vortex elements become more and more disordered. This has a detrimental effect not only on the PSE diffusion calculation, but also the velocity and stretching calculations. The particle density distribution throughout the flow field is examined by making use of the FMM box structure. The FMM can identify and index all particles in the vicinity of any given particle. Since this box structure is used to calculate the velocity, stretching and PSE diffusion calculations, monitoring the particle density using this method shows the direct relation between the magnitude of Lagrangian distortion and the error caused by it.

The case for $Re_\lambda = 25$ and $N = 64^3$ is considered, for which the FMM divides the domain into 8^4 boxes. One box contains an average of 64 particles, so if one considers

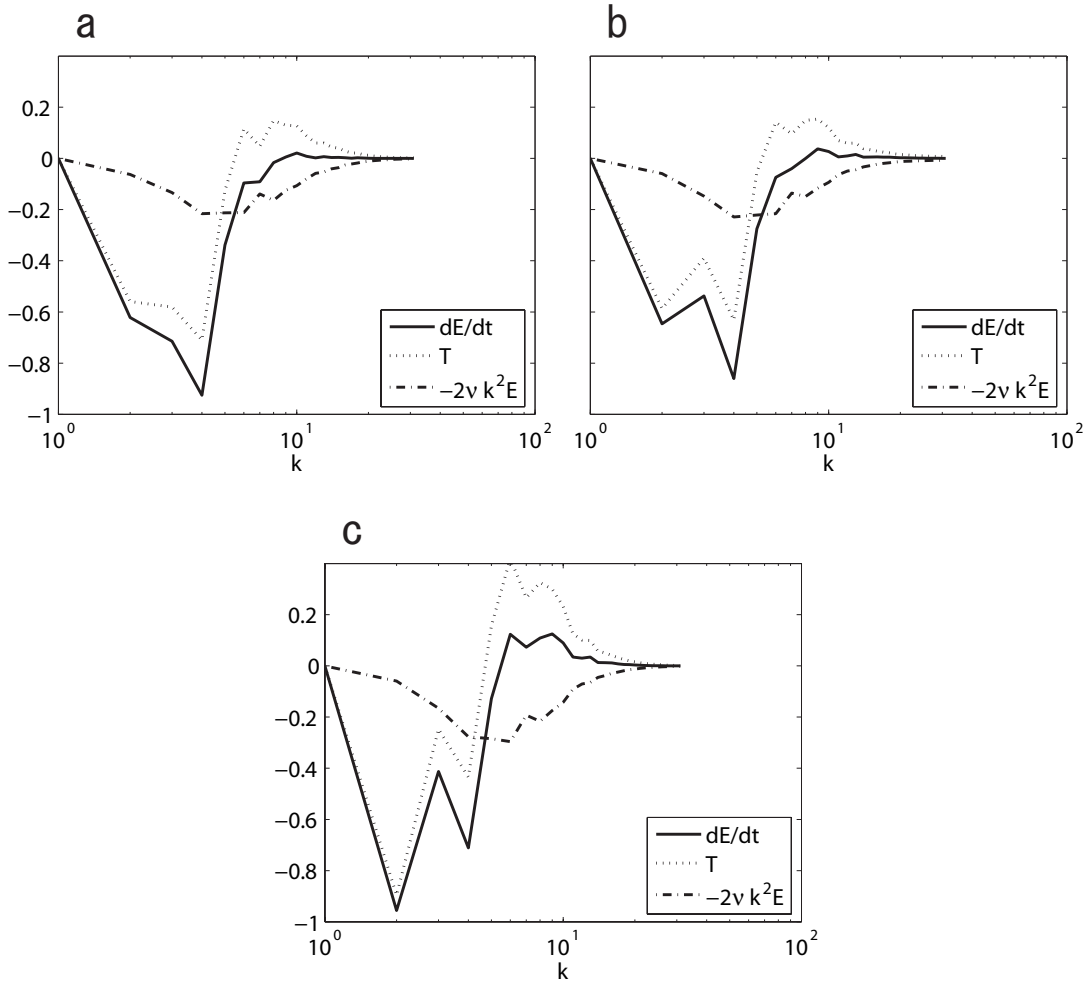

Figure 3.9: Energy Spectrum Equation Budget. (a) SGM. (b) PSE. (c) CSM.

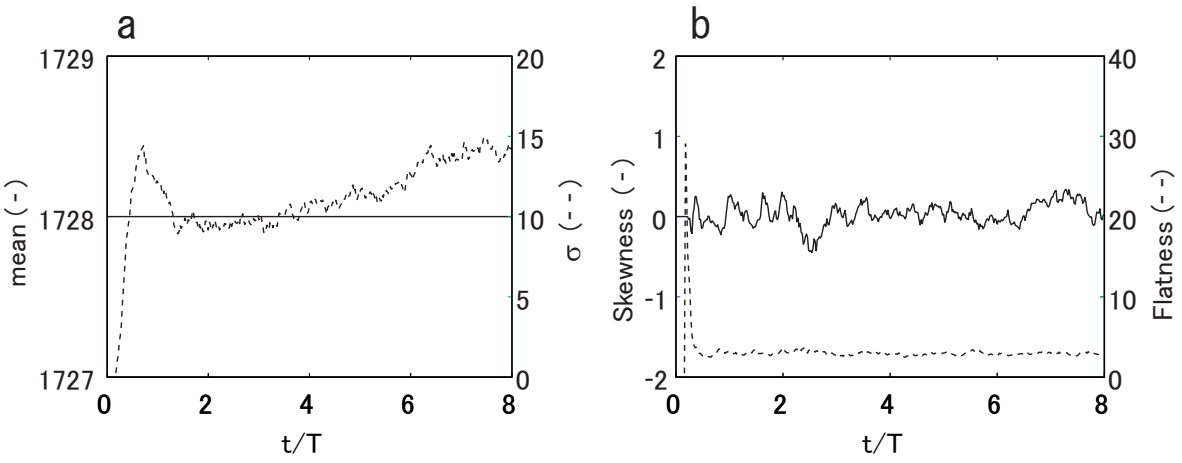

Figure 3.10: Statistics of the Particle Distribution. (a) Mean & RMS. (b) Skewness & Flatness.

particles in the 26 neighboring boxes the total should be $27 \times 64 = 1728$. This value differs between dense regions and sparse regions, and our concern is exactly how large this difference is, and how this changes as the calculation proceeds. Fig. 3.10 shows the mean, standard deviation, skewness, and flatness of the particle density distribution. The mean value is always 1728, since the total number of particles does not change. The standard deviation is 0 for the initially uniform distribution, and grows rapidly at the earlier stages of the calculation. However, the increment becomes moderate at later stages and the final value is still less than 1% of the mean. The skewness fluctuates between -0.5 and 0.5, and the flatness jumps at the first few time steps but remains close to 3 otherwise, which is common for an initially uniform distribution subject to random movement.

Next, a standard remeshing technique is used to maintain the uniformity of particles. The M'_4 function is used as the interpolation formula.

$$M'_4(x) = \begin{cases} 0, & \text{if } |x| > 2, \\ \dfrac{1}{2}(2-|x|)^2(1-|x|), & \text{if } 1 \le |x| \le 2 \\ 1 - \dfrac{5x^2}{2} + \dfrac{3|x|^3}{2}, & \text{if } |x| \le 1 \end{cases} \tag{3.11}$$

The remeshing is performed every 10 times steps, which corresponds to t/T=0.2. Judging from Fig. 3.10, the standard deviation of the particle density distribution should remain less than 0.1% of the mean. The kinetic energy spectra for the remeshed PSE at $Re_\lambda = 25$ and $N = 64^3$ are shown in Fig.3.11. The PSE without remeshing and SGM

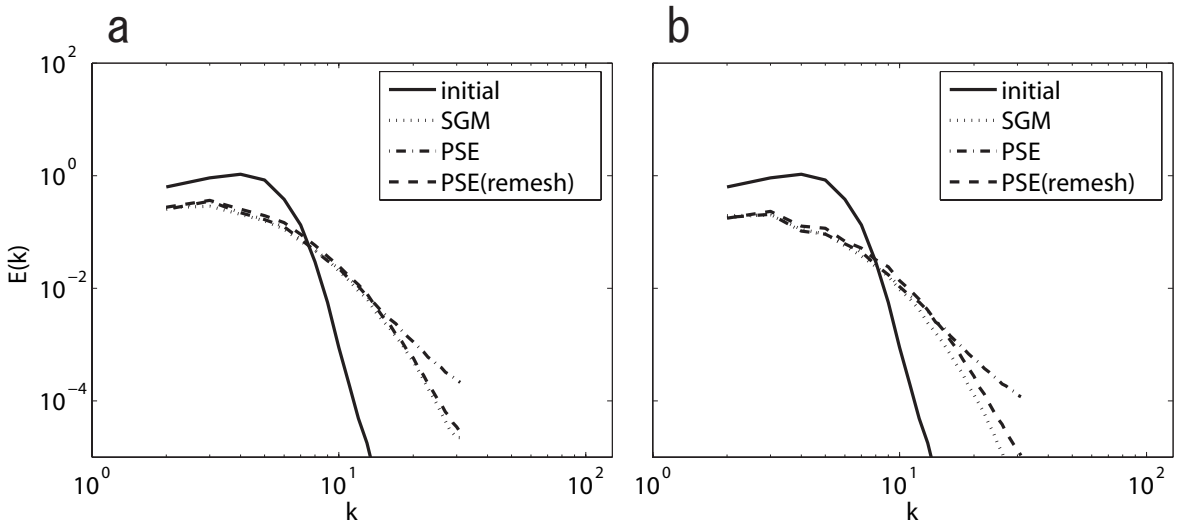

Figure 3.11: Kinetic Energy Spectra for PSE with remeshing. (a) Spectra at $t/T = 2$. (b) Spectra at $t/T = 4$.

are also plotted as reference. The remeshed PSE no longer shows the jump at the tail of the spectrum. At $t/T = 2$ it matches the SGM up to the highest wave numbers. At $t/T = 4$ the remeshed PSE slightly over-predicts a broad band of the spectrum, but is much closer to the SGM than the PSE without remeshing.

The time change of statistical values for the remeshed PSE are plotted in Fig. 3.12. The decay of kinetic energy has improved slightly at the end but is still different from that of the SGM. This supports our assumption that this error is caused by the error in stretching calculations, and has nothing to do with Lagrangian distortion of particles. Furthermore, when the remeshing is performed the velocity derivative skewness shows strange behavior at the end. The homogeneous isotropic turbulence is a flow field with minimum Lagrangian distortion effects. For this particular flow, the only effect of remeshing seems to be the suppression of the noise at the tail of the energy spectrum, and a small improvement in the kinetic energy decay.

3.3.6 Spatial Adaptation in CSM

The CSM is able to calculate accurately for a limited time, and diverges after that. This behavior is not only well known, but is also mathematically predictable [45]. The core radius eventually becomes too large for a sufficient spatial resolution of the local fluid motion. However, the CSM is known to converge if spatial refinement is performed

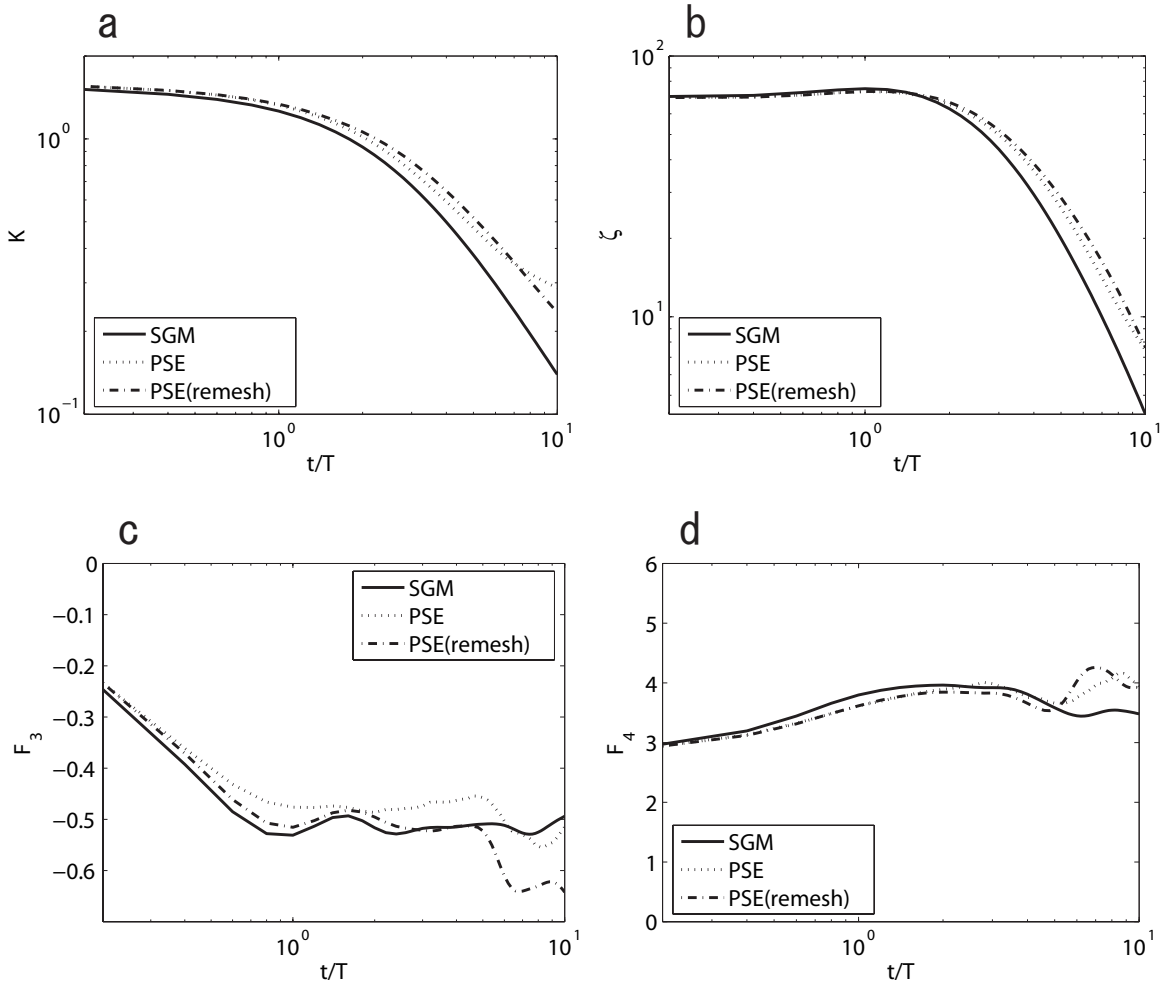

Figure 3.12: Statistical Properties for PSE with remeshing. (a) Kinetic energy. (b) Enstrophy. (c) Skewness. (d) Flatness.

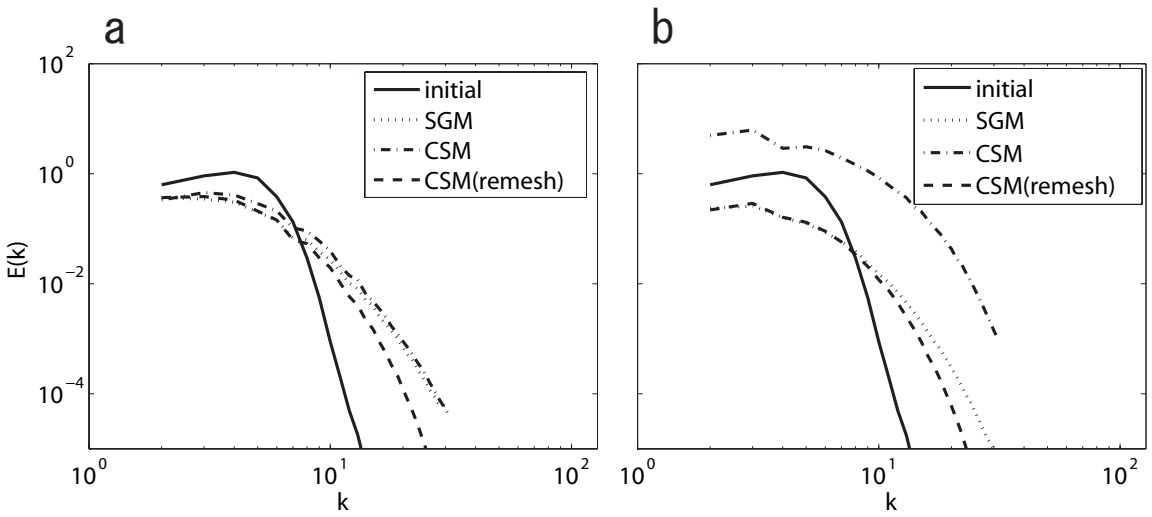

Figure 3.13: Kinetic Energy Spectra for CSM with spatial adaptation. (a) Spectra at $t/T = 2$. (b) Spectra at $t/T = 4$.

either globally [30] or locally [35]. In the present calculations, the use of splitting methods would have been difficult since the calculation cost would become overwhelming for an already spatially well resolved simulation.

One way to perform spatial refinement without increasing the number of elements would be to use the radial basis function interpolation [30] for smaller sized blobs to reproduce the vorticity field. This method has been applied by solving a system of equations given by

$$\boldsymbol{\omega}_i = \sum_{j=1}^{N} \boldsymbol{\alpha}_j \zeta_\sigma, \tag{3.12}$$

for the initial core radius $\sigma = 2\Delta x$. The BICGSTAB method without preconditioning is used for the iteration, and calculated until the L^2 norm error was less than 10^{-3}. The FMM box structure was also used to calculate Eq. (3.12) efficiently inside the BICGSTAB iteration. One spatial adaptation step takes the same amount of time as 5 vortex method time steps. Hence, if the spatial adaptation is performed every 5 time steps, it will double the total calculation time.

The kinetic energy spectra with spatial adaptation for $Re_\lambda = 25$ and $N = 64^3$ are shown in Fig. 3.13, along with the CSM without spatial adaptation and SGM. The spatial adaptation is performed every 10 time steps. 'CSM(remesh)' denotes the CSM with spatial adaptation. At $t/T = 2$ the CSM with spatial adaptation under-estimates the higher wave numbers. However, as the calculation proceeds, the spectrum of the

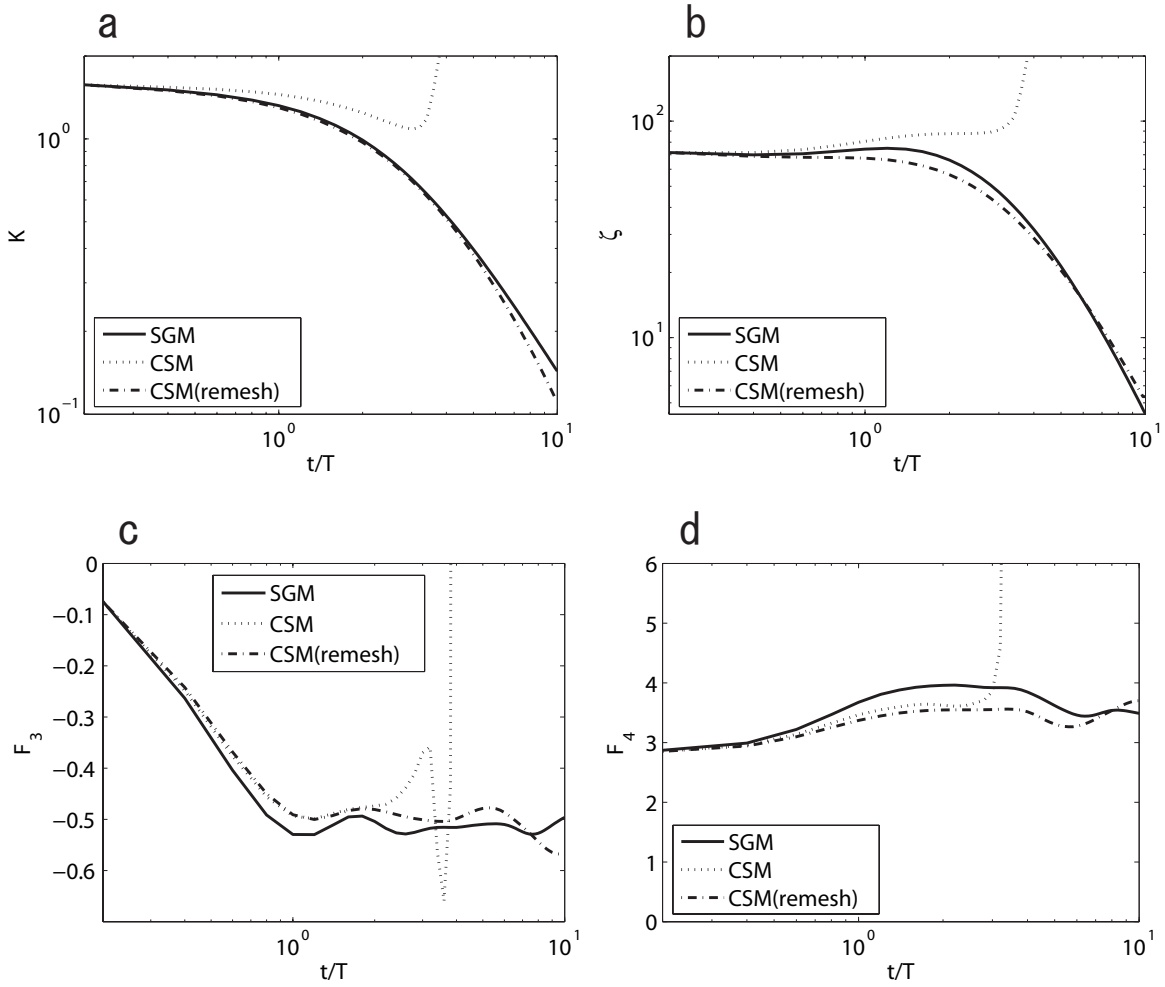

Figure 3.14: Statistical Properties for CSM with spatial adaptation. (a) Kinetic energy. (b) Enstrophy. (c) Skewness. (d) Flatness.

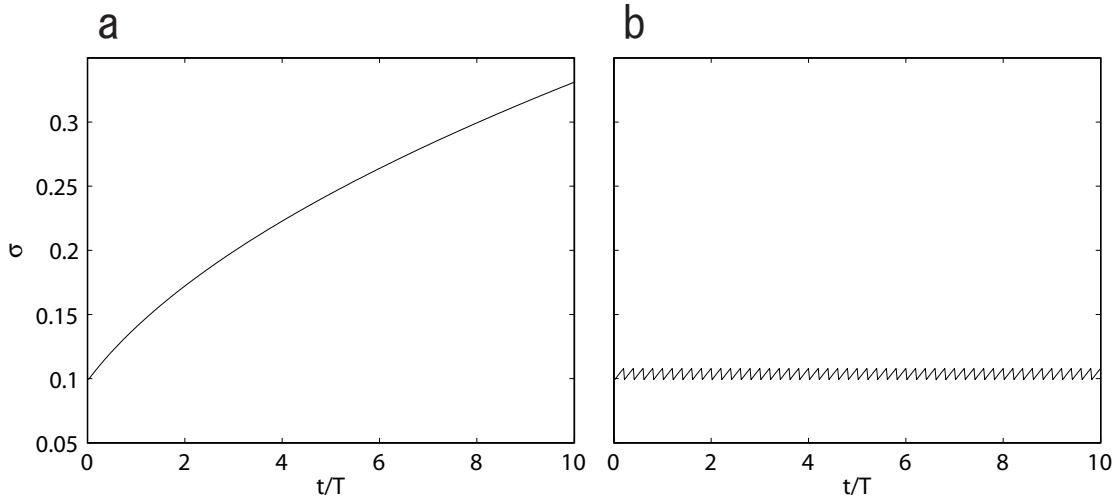

Figure 3.15: Growth of the Core Radius. (a) Without Spatial Adaptation. (b) With Spatial Adaptation.

CSM with spatial adaptation becomes closer to the SGM. This is completely different from the CSM without spatial adaptation, which diverges at $t/T \approx 4$.

Next, the kinetic energy, enstrophy, velocity derivative skewness, and flatness are shown in Fig. 3.14 for the same calculations. The CSM with spatial adaptation almost completely matches the SGM. These results are quite encouraging, and it is fair to say that the core spreading method with spatial adaptation is indeed a very accurate viscous diffusion scheme.

Finally, the growth of the core radius is shown for the cases with and without spatial adaptation in Fig. 3.15. The initial core radius is $2\pi/64 \approx 0.1$ and nearly doubles by the time $t/T = 10$ without spatial adaptation. However, with the spatial adaptation, the core radius increases by only 1%. A thorough investigation of the frequency of spatial adaptation or the optimum overlap ratio range is out of scope of the present investigation. However, we will note that such an investigation is important and maybe inevitable in the future of vortex methods.

3.4 Conclusions

The vortex method is applied to the calculation of a decaying homogeneous isotropic turbulence of $Re_\lambda = 25, 50$ and the results are compared with a spectral method calculation. The core spreading method and particle strength exchange were selected as

the viscous diffusion scheme, and the effect of spatial adaptation was examined. The following conclusions are drawn from the results of our calculations.

For the particle strength exchange, the discrepancy of the kinetic energy spectrum between the vortex method and spectral method is less than 1%, up to the dissipation wave number. The number of elements required however, seems to be much larger than that of the spectral method. Also, the use of remeshing has minimal effect in an isotropic turbulence, where the results with and without remeshing differ only by 0.01%.

The results of the core spreading method are only valid until $t/T \approx 2$ without spatial adaptation. However, the use of the radial basis function interpolation for spatial adaptation proved to be very effective. It not only keeps the calculation from diverging, but allows the core spreading method to calculate the kinetic energy decay at an accuracy close to that of the spectral methods until $t/T \approx 20$. The quantitative difference at $t/T \approx 20$ is approximately 3%.

The overall conclusion corresponding to the initial objective is that the vortex method can calculate the dissipation in the isotropic turbulence correctly if the following conditions are satisfied. The spatial resolution must be satisfactory. If the PSE is used no spatial adaptation is required for this flow. However, if the core spreading method is used, the spatial adaptation must be performed.

Chapter 4

Calculation of Homogeneous Shear Flow

4.1 Introduction

In this section, the homogeneous shear flow is considered. A novel technique for calculating the FMM under shear periodic boundary conditions is presented. Using this technique, the vortex method calculation of the homogeneous shear flow is performed and compared with a finite difference method. The focus of this section is on the ability of vortex methods to reproduce the anisotropy of turbulence, i.e. the ability of spherical vortex blobs to reproduce streaky global vortex structures. The shear-rate is selected so that it matches the maximum shear-rate observed at $y^+ \approx 10$ in near wall flows [46]. Another objective is the assessment of the production of turbulence in vortex methods, i.e. the validation of the vortex stretching term calculation for strongly strained flows. The present calculation of the homogeneous shear flow may be considered as an intermediate validation step, which will fill the gap between the calculation of isotropic turbulence and wall bounded flows.

4.2 Numerical Method

4.2.1 Homogeneous Shear Equations

The Navier-Stokes and pressure Poisson equation for the fluctuating components are

$$\frac{\partial u_i}{\partial t} + f_i = -\frac{1}{\rho}\frac{\partial p}{\partial x_i} + \nu\frac{\partial^2 u_i}{\partial x_j^2}, \tag{4.1}$$

$$\frac{\partial^2 p}{\partial x_i^2} = -\rho\frac{\partial f_i}{\partial x_i}. \tag{4.2}$$

In spectral form they become

$$\frac{\partial \hat{u}_i}{\partial t} + \hat{f}_i = -\frac{1}{\rho}\iota k_i \hat{p} + \nu k^2 \hat{u}_i, \tag{4.3}$$

$$-k^2\hat{p} = -\rho\iota k_j \hat{f}_j. \tag{4.4}$$

f_i is the convection term

$$f_i = u_j\frac{\partial u_i}{\partial x_j}. \tag{4.5}$$

When one considers a mean shear $U_i = Sx_3\delta_{i1}$, only the convection term changes

$$f_i = u_j\frac{\partial u_i}{\partial x_j} + Sx_3\frac{\partial u_i}{\partial x_1} + Su_3\delta_{i1}, \tag{4.6}$$

and the other parts remain the same. Furthermore, if the coordinate transform $X_i = x_i - Stx_3\delta_{i1}$ is performed, the equations for the fluctuating components yields

$$\frac{\partial u_i}{\partial t} + f_i = -\frac{1}{\rho}\left(\frac{\partial p}{\partial x_i} - St\frac{\partial p}{\partial x_1}\delta_{i3}\right) + \nu\left(\frac{\partial^2 u_i}{\partial x_j^2} - 2St\frac{\partial^2 u_i}{\partial x_1\partial x_3} + S^2t^2\frac{\partial^2 u_i}{\partial x_1^2}\right), \tag{4.7}$$

$$\frac{\partial^2 p}{\partial x_i^2} - 2St\frac{\partial^2 p}{\partial x_1\partial x_3} + S^2t^2\frac{\partial^2 p}{\partial x_1^2} = -\rho\left(\frac{\partial f_i}{\partial x_i} - St\frac{\partial f_3}{\partial x_1}\right). \tag{4.8}$$

The spectral from of these equations are

$$\frac{\partial \hat{u}_i}{\partial t} + \hat{f}_i = -\frac{1}{\rho}\left(\iota k_i - St\iota k_1\delta_{i3}\right)\hat{p} + \nu\left(k^2 - 2Stk_1k_3 + S^2t^2k_1^2\right)\hat{u}_i \tag{4.9}$$

$$-\left(k^2 - 2Stk_1k_3 + S^2t^2k_1^2\right)\hat{p} = -\rho\left(\iota k_j\hat{f}_j - St\iota k_1\hat{f}_3\right), \tag{4.10}$$

and the corresponding convection term can be expressed as

$$f_i = u_j\frac{\partial u_i}{\partial x_j} - Stu_3\frac{\partial u_i}{\partial x_1} + Su_3\delta_{i1}. \tag{4.11}$$

4.2.2 Vortex Method for Homogeneous Shear Flows

The flow of interest is an incompressible, turbulent shear flow subject to a mean shear. In the present calculation, the instantaneous velocity and vorticity are decomposed into the time-averaged component and the fluctuating component.

$$\tilde{u}_i = U_i + u_i, \tag{4.12}$$

$$\tilde{\omega}_i = \Omega_i + \omega_i. \tag{4.13}$$

Without loss of generality, one may assume that the mean velocity is unidirectional in the downstream direction x_1 and has a constant shear-rate S in the vertical direction x_3.

$$U_i = S x_3 \delta_{i1}. \tag{4.14}$$

The corresponding transport equation for the fluctuating component of vorticity can be written as

$$\frac{D\omega_i}{Dt} = \omega_j \frac{\partial u_i}{\partial x_j} + S\frac{\partial u_i}{\partial x_2} + S\omega_3\delta_{i1} + \nu\frac{\partial^2 \omega_i}{\partial x_j \partial x_j}, \tag{4.15}$$

where u is also the fluctuating component of velocity. The second and third term on the right hand side of Eq. (4.15) are the additional stretching terms, which reflect the effect of mean shear.

In the present vortex method, Eq. (4.15) is discretized by expressing the vorticity field as a superposition of Gaussian distributions,

$$\zeta_\sigma = \frac{1}{(2\pi\sigma^2)^{3/2}} \exp\left(-\frac{|x|^2}{2\sigma^2}\right), \tag{4.16}$$

where σ is the core radius of the vortex element, and $|x|$ is the distance between two vortex elements. Thus, the vorticity vector at point p is calculated by summing the influence of all particles q, each having a Gaussian distribution,

$$\omega_i^p = \sum_{q=1}^{N} \zeta_\sigma \alpha_i^q, \tag{4.17}$$

where α is the strength of the vortex element.

The velocity is calculated as the sum of the Biot-Savart velocity and the mean shear,

$$u_i^p = \sum_{q=1}^{N} \epsilon_{ijk}\alpha_j^q g_\sigma \frac{\partial G}{\partial x_k^q} + S x_3^p \delta_{i1}, \tag{4.18}$$

where $x_i = x_i^p - x_i^q$ is the distance vector and g_σ is the cutoff function, which has the form

$$g_\sigma = \mathrm{erf}\left(\frac{|x|}{2\sigma}\right) - \sqrt{\frac{2}{\pi}}\frac{|x|}{\sigma}\exp\left(-\frac{|x|^2}{2\sigma^2}\right). \tag{4.19}$$

G is the free space Green's function of the Laplace equation, and its dipole and quadrupole are

$$\frac{\partial G}{\partial x_i} = -\frac{x_i}{4\pi|x|^3}, \tag{4.20}$$

$$\frac{\partial^2 G}{\partial x_i \partial x_j} = -\frac{1}{4\pi}\left(\frac{\delta_{ij}}{|x|^3} - \frac{3x_i x_j}{|x|^5}\right). \tag{4.21}$$

Similarly, the vorticity stretching terms of Eq. (4.15) can be written as

$$\frac{D\alpha_i^p}{Dt} = \sum_{q=1}^{N} \epsilon_{ijk}\alpha_l^p \alpha_j^q \frac{\partial}{\partial x_l^p}\left(g_\sigma \frac{\partial G}{\partial x_k^q}\right) + S\epsilon_{ijk}\alpha_j^q \frac{\partial}{\partial x_2^p}\left(g_\sigma \frac{\partial G}{\partial x_k^q}\right) + S\alpha_3^p \delta_{i1}. \tag{4.22}$$

The diffusion term of Eq. (4.15) is solved by the core spreading method with spatial adaptation.

For the calculation of Eq. (4.18) and Eq. (4.22), the shear periodic boundary condition is enforced by using a shear periodic FMM mentioned in section 4.2.3. Upon calculating the convection, the shear periodic boundary condition requires the elements that move out of the domain in the vertical direction x_3 to consider the shear when re-entering from the other side. For example, the elements that move out of the domain from (x_1, x_2, π) re-enter the domain from $(x_1 - 2\pi St, x_2, -\pi)$, where S is the shear-rate and t is time. The elements that move out of the domain in other directions re-enter from the opposite side by adding or subtracting 2π from the coordinates.

4.2.3 Shear Periodic Fast Multipole Method

The fast multipole method (FMM) has been extended to periodic boundary conditions by Lambert *et al.* [42], where the boundary condition is approximated by using a finite number of periodic images. The shear periodic boundary condition itself has been used in non-equilibrium molecular dynamics.[47] However, to the authors' knowledge, there have been no extensions of the FMM to shear periodic boundary conditions. A novel technique is introduced to extend the FMM to shear periodic boundary conditions.

The flow of calculation of the shear periodic FMM is analogous to that of the periodic FMM. One major difference between the periodic FMM and shear periodic FMM is the treatment of periodic images in the sheared direction. In the case of a non-sheared

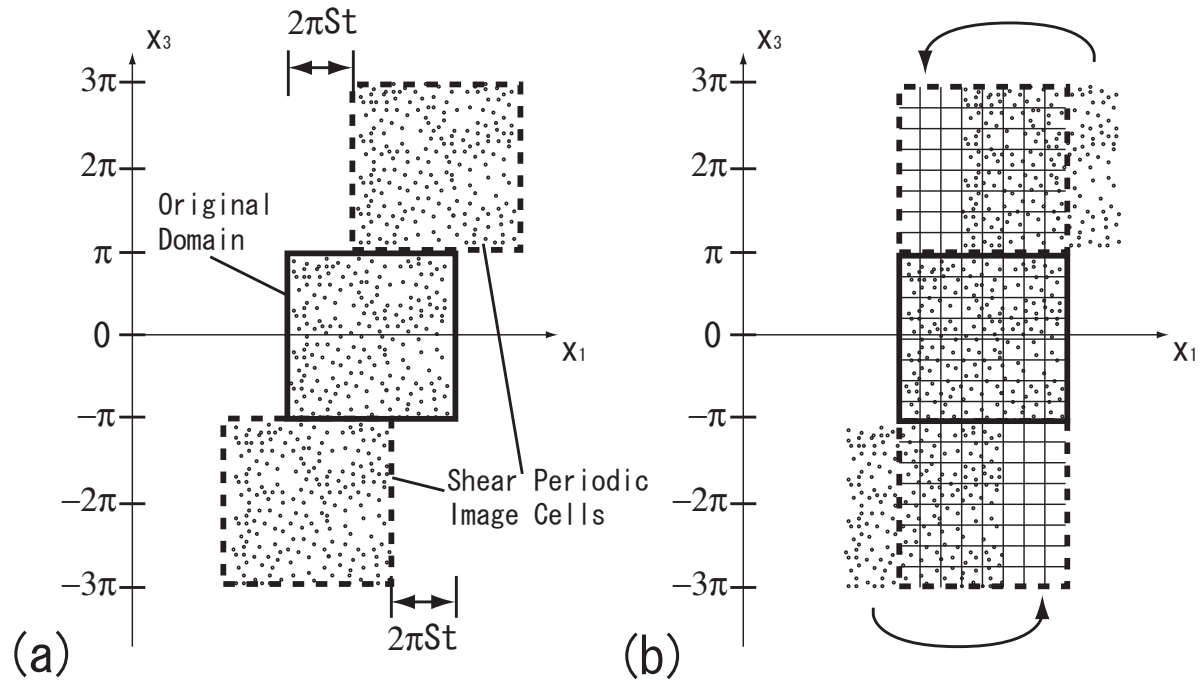

Figure 4.1: Schematic of Element Shifting in Shear Periodic FMM

periodic FMM, the multipole expansions for the periodic image cells are identical to that of the original cell. In other words, the periodicity of the field allows one to use the multipole expansions of the original domain to consider the contribution of the periodic images. However, for the shear periodic FMM, the multipole expansions of the periodic image cells in the sheared direction are not identical to those of the original cell. We shall refer to these cells as "shear periodic image cells".

A schematic of the shear periodic image cells is shown in Fig. 4.1. The solid lines represent the boundary of the original domain $[-\pi, \pi]$. The dashed lines represent the boundary of the shear periodic image cells. Fig. 4.1 (a) describes how the elements inside the shear periodic image cells are shifted. Fig. 4.1 (b) shows how the multipole expansions are calculated on an aligned cell structure. Thus, the elements that fall outside of the domain when shifted, are moved to the other side to fill the cell structure. It is necessary to calculate the multipole expansion for all periodic image cells in the x_3 direction, each with a different shifting distance. The Nth shear periodic image cell in the $\pm x_3$ direction is shifted by $\pm 2\pi NSt$. Thus, the particle to multipole translation is

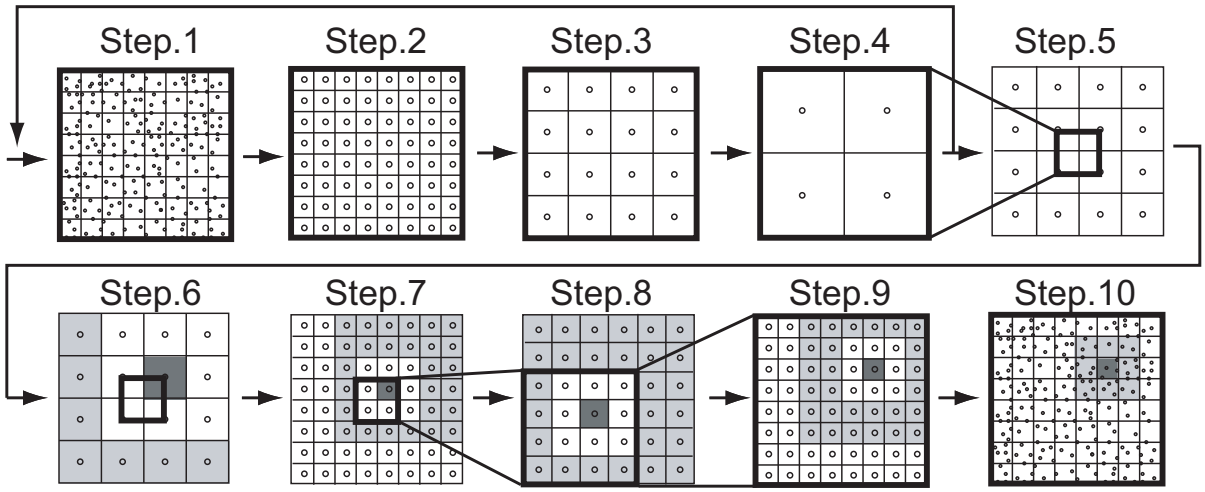

Figure 4.2: Flow of Calculation in Shear Periodic FMM

calculated by

$$X_j = x_j \pm 2\pi N St, \tag{4.23}$$

$$\rho_j = \sqrt{X_j^2 + y_j^2 + z_j^2}, \tag{4.24}$$

$$\alpha_j = \tan^{-1}\left(\frac{y_j}{X_j}\right), \tag{4.25}$$

$$\beta_j = \cos^{-1}\left(\frac{z_j}{\rho_j}\right), \tag{4.26}$$

$$M_n^m = \sum_{j=1}^{N} \boldsymbol{\alpha}_j \rho_j^n Y_n^{-m}(\alpha_j, \beta_j). \tag{4.27}$$

A schematic of the flow of calculation is shown in Fig. 4.2. The heavy lines represent the boundary of the original domain $[-\pi, \pi]$. In step 1, the original calculation domain is repeatedly divided into smaller cells until the optimum level is reached. In step 2, the multipole expansion is calculated at the center of each cell. In steps 3 and 4, the cells are repeatedly grouped, and the multipole expansion is shifted to the center of the larger cells. Steps 1 through 4 are repeated for all shear periodic image cells.

In step 5, the cells are further grouped and the multipole expansions are shifted to the center of larger cells. The cells may be grouped further to account for a larger number of periodic images. In step 6, the multipole expansions are translated to local expansions for non-neighboring cells. For example, the local expansions of the dark grey cell are calculated from the multipole expansions of the light grey cells. The colored boxes are a representation of one interaction list. In steps 7, 8, and 9, the cells are repeatedly

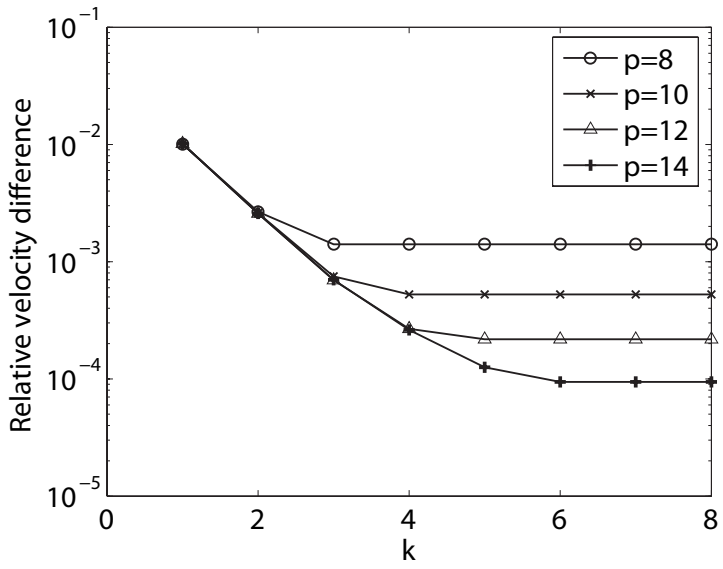

Figure 4.3: Relative Error of the Biot-Savart Calculation for a Different Number of Shear Periodic Image Cells

divided, and the local expansions are translated to the center of these cells. At the same time, the multipole expansions of the newly non-neighboring cells (shown in light grey) are also translated to the divided cells (shown in dark grey). In step 10, the effect of the neighboring cells at the bottom level is calculated by a direct interaction of the particles. If the neighboring cell happens to be a member of the shear periodic image cell, the coordinates of the elements in the cell are accordingly shifted.

The impact of the number of periodic image cells and the order of the multipole expansion on the accuracy is examined. $N = 100$ particles with random coordinates and random strength are placed within a $[-\pi, \pi]^3$ domain and calculated for $2^k \times 2^k \times 2^k$ periodic images . The result of the direct calculation for $k = 8$ is used as a reference value. The results for different orders of multipole expansion p are shown in Fig. 4.3. The relative velocity difference is calculated by taking the L^2 norm of the difference from the reference value. The relative velocity difference decreases as k is increased until it reaches the accuracy limit of the FMM for the given order of multipole expansions. The results are identical to that of the periodic FMM in the isotropic turbulence calculation, which is expected since shifting elements to account for the shear should not introduce additional error to the periodic FMM. For the homogeneous shear flow calculations $p = 10$ and $k = 4$ are selected, which is identical to the homogeneous isotropic turbulence calculation.

The breakdown of the calculation time of the shear periodic FMM is shown in Fig. 4.4.

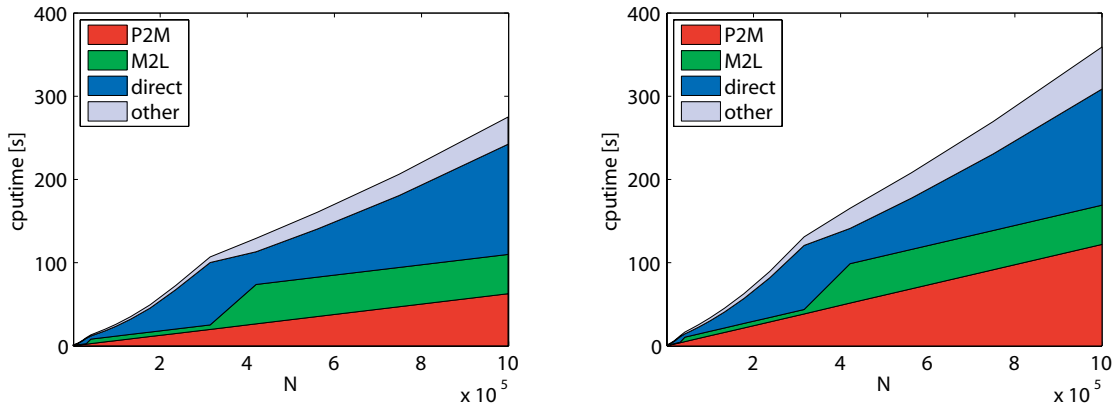

(a) k=4 (b) k=5

Figure 4.4: Breakdown of CPU-time for Different k

Fig. 4.4(a) and Fig. 4.4(b) are the results for $k = 4$ and $k = 5$, respectively. N is the number of particles. P2M, M2L, direct, and others are the cumulative CPU-time of the particle to multipole translation, the multipole to local translation, direct summation, and everything else. The order of the multipole expansion is set to $p = 10$. For a standard periodic FMM the multipole to local translation and direct summation will take up most of the calculation time. However, since the shear periodic FMM requires the particle to multipole translation to be performed for all shear periodic image cells, its percentage rises to 25% and 30% of the total for $k = 4$ and $k = 5$, respectively.

In summary, the present shear periodic FMM adds no further errors to the non-shear periodic FMM, and is able to calculate at this accuracy with only a 30% increase in CPU-time.

4.2.4 Finite Difference Method for Homogeneous Shear Flows

In our present calculations, the finite difference method with shear periodic boundary conditions was used as a reference [48]. For the same mean shear as in Eq. (4.14), the Navier-Stokes equation for the fluctuating component of velocity becomes

$$\frac{\partial u_i}{\partial t} + u_j \frac{\partial u_i}{\partial x_j} + S x_3 \frac{\partial u_i}{\partial x_1} + S u_3 \delta_{i1} = -\frac{1}{\rho}\frac{\partial p}{\partial x_i} + \nu \frac{\partial^2 u_i}{\partial x_j \partial x_j}. \tag{4.28}$$

This equation was solved on a staggered grid using the SMAC method. The fourth-order central difference method was used for the spatial discretization, and the third-order low storage Runge-Kutta method [49] was used for the temporal discretization.

4.3 Calculation Results

The homogeneous shear flow was calculated by the vortex method and the finite difference method, using $N = 64^3, 128^3$ points. The initial Reynolds number based on Taylor's micro scale was $Re_\lambda = 25$. The calculation domain was $[-\pi, \pi]^3$ for both methods.

4.3.1 Initial Condition for Homogeneous Shear Flows

The initial condition of the homogeneous shear flow calculation (for both the vortex method and the finite difference method) were generated from an isotropic turbulence calculation using the finite difference method. First, the initial condition for the isotropic turbulence calculation was generated in Fourier space as a solenoidal isotropic velocity field with random phases and a prescribed energy spectrum [41]. After transforming the velocity to physical space, the isotropic turbulence calculation was performed using the finite difference method until the skewness of the velocity derivative reached a steady-state value of -0.5. The finite difference calculation used this initial condition directly.

The initial condition for the vortex method was generated as follows. First, the vortex elements were placed on the nodes of the finite difference method grid. Then, the vorticity at the grid points were calculated from the initial velocity field using a fourth order central difference method. Following that, the strength of the vortex elements were calculated from the vorticity by using a radial basis function interpolation [30]. The core radius of the vortex elements were set to $2\pi/N$ so that the overlap ratio became $\sigma/dx = 1$. The homogeneity of the present flow field permits the use of a rather small overlap ratio, which allows us to achieve a high spatial resolution using minimum calculation effort.

4.3.2 Test for $S = 0$

In order to validate the codes used in the present calculation, the isotropic turbulence calculation was performed using the following four codes; the pseudo-spectral method code used in the isotropic turbulence calculation (PSM), the vortex method code used in the isotropic turbulence calculation (VM1), the present finite difference method code for the homogeneous shear flow with $S = 0$ (FDM), and the present vortex method code for the homogeneous shear flow with $S = 0$ (VM2). The initial Reynolds number was $Re_\lambda = 25$ and the number of calculation points was $N = 64^3$. The time increment was $\Delta t = 0.005$ for all calculations, which corresponds to $t = 0.25\tau$, where τ is the Kolmogorov time scale.

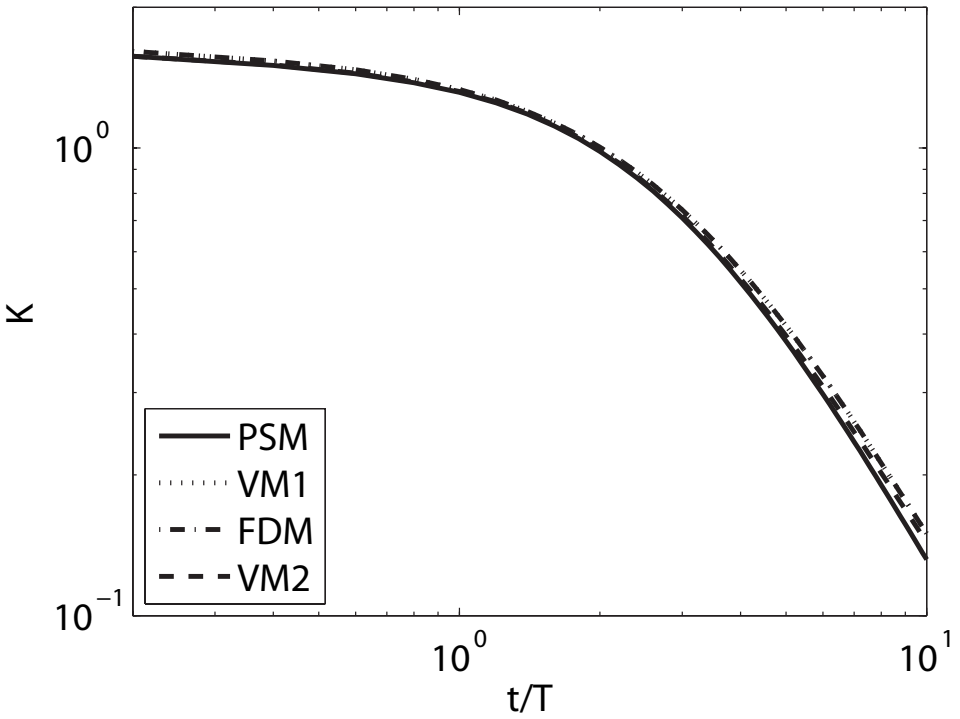

(a) Decay of Kinetic Energy

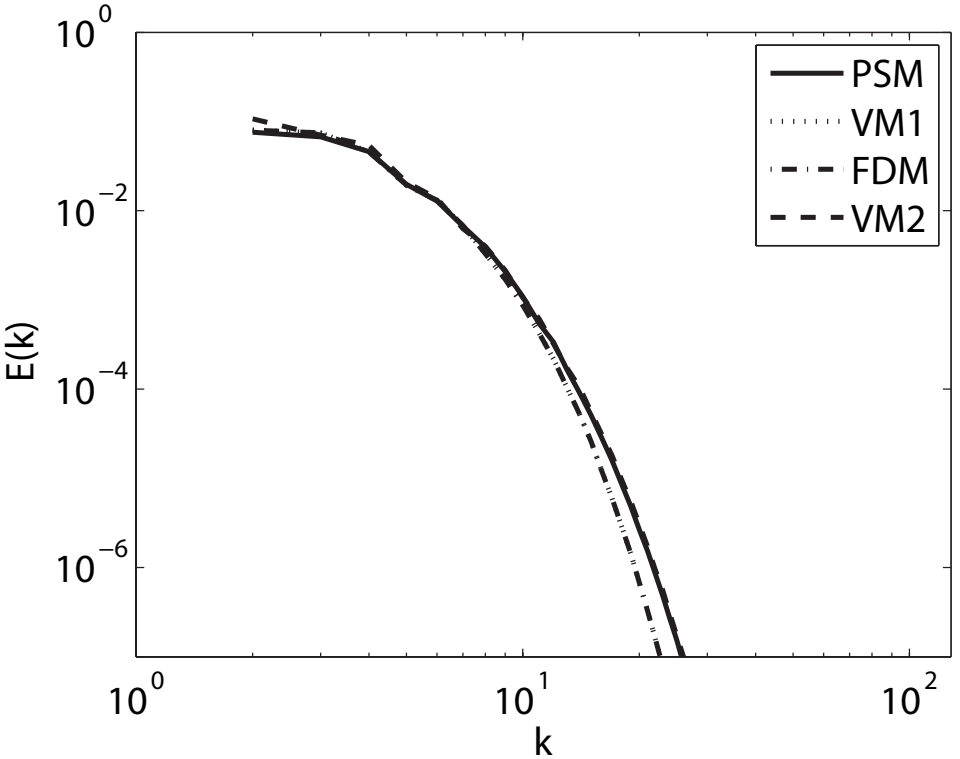

(b) Energy Spectrum at t/T=10

Figure 4.5: Isotropic Turbulence Calculation for $Re_\lambda = 25$, $N = 64^3$

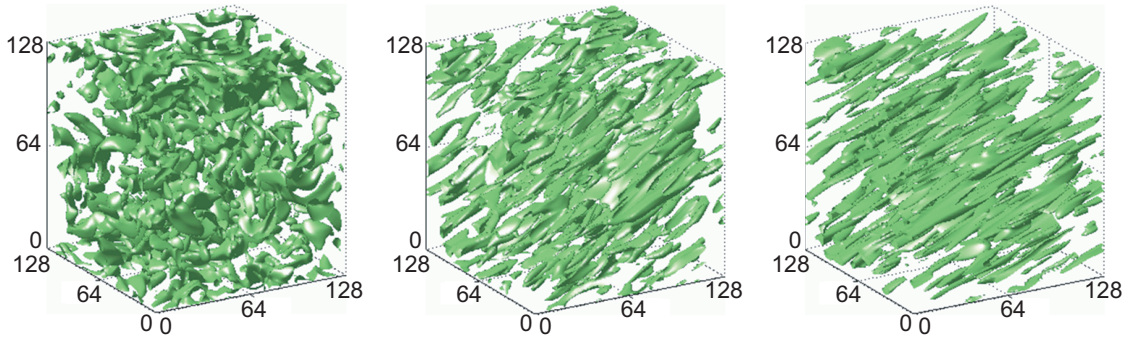

(a) $t^* = 0$ (b) $t^* = 1$ (c) $t^* = 2$

Figure 4.6: Isosurface of II (Finite Difference Method)

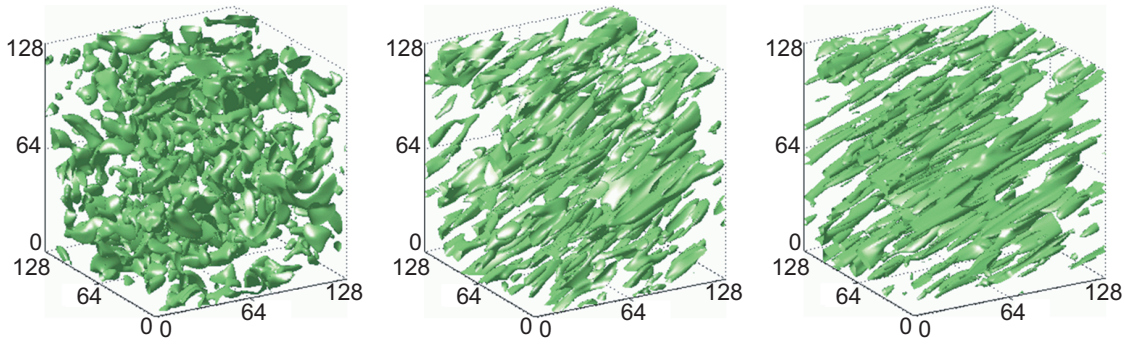

(a) $t^* = 0$ (b) $t^* = 1$ (c) $t^* = 2$

Figure 4.7: Isosurface of II (Vortex Method)

The decay of kinetic energy for the four cases is shown in Fig. 4.5(a). The results of the two vortex method calculations are almost identical. The difference between the pseudo-spectral method and finite difference method is also very small. The energy spectrum at $t/T = 10$ is shown in Fig. 4.5(b), where T is the eddy turnover time $T = 0.25$. There is a visible difference between the results of the vortex methods and the grid-based methods. This is considered to be the result of the cumulative errors in the vortex method calculations. However, considering the fact that the Kolmogorov wavenumber is $k_\eta \approx 20$ for this flow, the discrepancies at the higher wavenumbers do not pose a serious problem to the overall kinetic energy balance.

In summary, the pseudo-spectral method, finite difference method, and vortex method produce similar results for the decaying isotropic turbulence. The match in the kinetic energy decay rate indicates the soundness of the present calculation codes.

4.3.3 Anisotropic Structures

One of the main objectives of the present study is to ascertain the magnitude of anisotropy, which the vortex blob method can handle. Lee *et al.* [46] showed in their pseudo-spectral calculation of the homogeneous shear flow, that a high shear-rate produces streaky structures similar to those observed in the near-wall region of the channel flow DNS by Kim *et al.* [50]. They also investigated the suitable turbulence length scale that can be used to construct a dimensionless and universal shear-rate parameter, which can be used as an indicator of streaky structures for both the homogeneous shear flow and high shear regions near the wall. This dimensionless shear-rate parameter is defined as

$$S^* \equiv \frac{2SK}{\epsilon}, \tag{4.29}$$

where $K = \overline{u_i^2}/2$ is the turbulent kinetic energy and $\epsilon = \nu\overline{u_{i,j}u_{j,i}}$ is the dissipation rate. Lee *et al.* [46] applied this shear-rate parameter to the fully developed channel flow by Kim *et al.* [50] and showed that the maximum is $S^* = 35$ in the viscous sublayer, and decreases to about one-sixth of the maximum in the logarithmic layer. In the present calculation the shear-rate $S = 18$ is chosen so that the shear-rate parameter becomes $S^* \approx 35$.

The qualitative aspects of the present calculations are presented first. The isosurface of the second invariant of the velocity gradient tensor $II = u_{i,j}u_{j,i}$ for the finite difference method and vortex method are shown in Figs. 4.6 and 4.7, respectively. The time t^* is normalized by the shear-rate S. At $t^* = 0$, the flow is isotropic and the structures have no directional preference. At $t^* = 1$, the vortices are strained and the structures begin to show a directional preference. At $t^* = 2$, many streaky structures can be observed. From these results, it has been confirmed that the vortex method can reproduce the streaky structures in high shear flows very well.

4.3.4 Anisotropy Tensors

The Reynolds stress anisotropy tensor is a direct measure of the anisotropy of the velocity fluctuations, and is a more quantitative measure of the ability to reproduce anisotropic turbulence. The normal components of the Reynolds stress anisotropy tensor are shown in Fig. 4.8. FDM(64^3), VM(64^3), FDM(128^3), and VM(128^3) are the finite difference method using a $N = 64^3$ grid, the vortex method using $N = 64^3$ particles, the finite difference method using a $N = 128^3$ grid, and the vortex method using $N = 128^3$ particles. Different markers represent the different normal components of b_{ij}. The overall

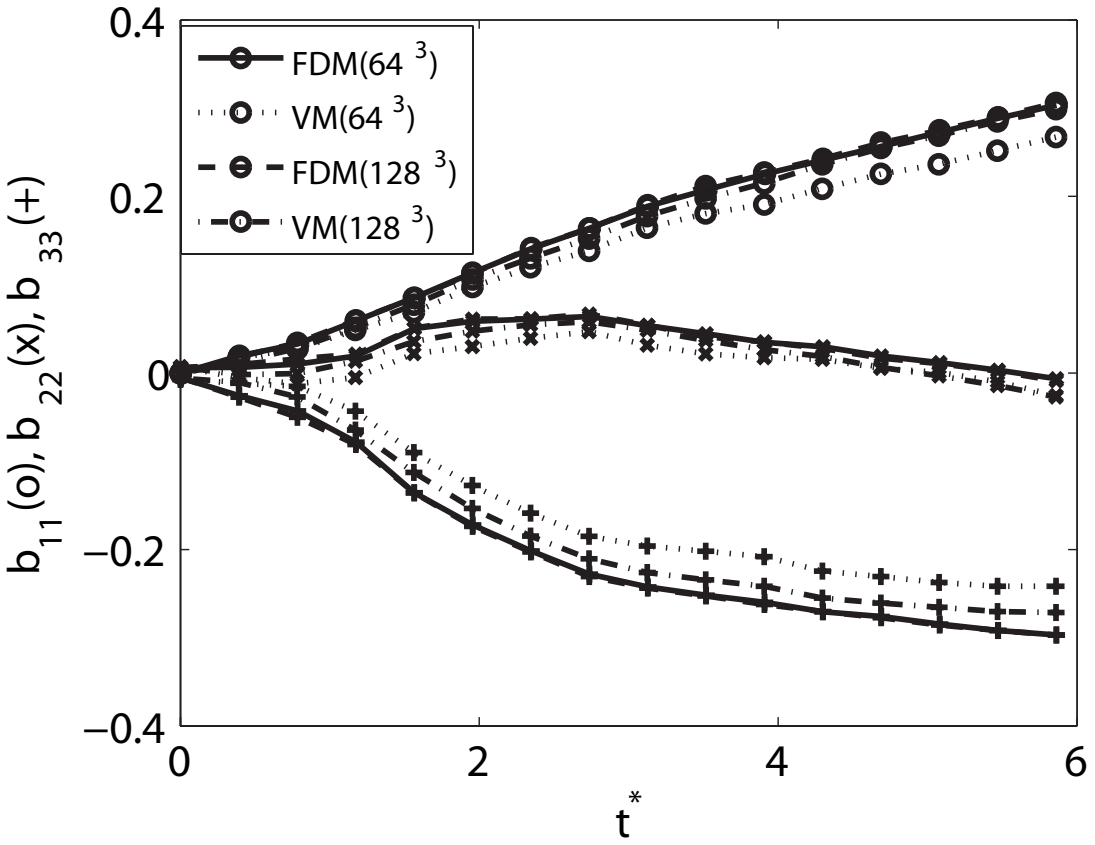

Figure 4.8: The Development of the Reynolds Stress Anisotropy Tensor

behavior of the present vortex method is similar to that of the finite difference method. The results of the two finite difference method calculations are indistinguishable. On the other hand, when the spatial resolution of the vortex method is increased, the difference between the finite difference method and vortex method decreases. The fact that vortex methods require a larger number of elements compared to grid-based methods, is consistent with the observations in the isotropic turbulence calculations.

From these observations, it can be said that the present vortex method code can account for strong anisotropy comparable to that in the viscous sublayer of a near wall flow if the spatial resolution is sufficient. Though, the number of necessary vortex elements may be large compared to grid-based methods.

The anisotropy tensor for the Reynolds stress is

$$b_{ij} = \frac{\overline{u_i u_j}}{\overline{u_k u_k}} - \frac{1}{3}\delta_{ij}. \tag{4.30}$$

4.3.5 Probability Density Functions

The probability density function (PDF) of the Reynolds shear stress u_1u_3 is shown for several time steps in Fig. 4.9. The probability density for the product $x = u_1u_3/\langle u_1u_3\rangle$ of two jointly Gaussian distributions with zero mean is given by

$$P_{u_1u_3}(x) = \frac{|r|}{\pi\sqrt{1-r^2}} \exp\left(\frac{r^2 x}{1-r^2}\right) K_0\left(\left|\frac{rx}{1-r^2}\right|\right), \tag{4.31}$$

where $r = \langle u_1u_3\rangle/\sigma_{u_1}\sigma_{u_3}$ is the correlation coefficient and K_0 is the zeroth order modified Bessel function of the second kind [51]. The solid line corresponds to the PDF of $(x - \langle x\rangle)/\sigma_{x-\langle x\rangle}$, while the dashed line represents the Gaussian joint PDF calculated from Eq. 4.31. FDM and VM are the results of the finite difference method and vortex method both using $N = 128^3$ calculation points. The PDF of the solid line is slightly larger than that of the dashed line at the tails. This is caused by the non-Gaussianity of the velocity components, and has been reported in previous calculations [52]. The results of the finite difference method and vortex method seem, at first glance, quite similar. However, at $t^* = 4$ the PDF of the vortex method is close to the joint Gaussian fit, whereas the PDF of the finite difference method remains non-Gaussian.

The correlation between u_1 and u_3 is examined by plotting the joint PDF in Fig. 4.10. The isoprobability contours are logarithmically spaced, and are separated by factors of 10. A strong negative correlation is observed in both the FDM and VM. The shapes of the third and fourth contour lines from the center are slightly different, which is consistent with the difference observed in the previous $P(u_1u_3)$ plots. The skewness and flatness of u_1u_3 are $S_{FDM} = -4.87$, $F_{FDM} = 26.3$, and $S_{VM} = -4.92$, $F_{VM} = 25.4$ for the finite difference method and vortex method, respectively.

In Fig. 4.11 the PDF of ω_1, ω_2 and ω_3 at $t^* = 4$ are shown. The dashed curve represents the Gaussian distribution. The streamwise vorticity ω_1 remains symmetric, but the spanwise component ω_2 and transverse component ω_3 are skewed toward the positive direction. Furthermore, for ω_2 the negative side is steeper than the Gaussian distribution and the positive side is flatter. The asymmetry of the PDF of ω_2 reflects the generation of vorticity in the positive direction due to the mean shear. ω_3 matches the Gaussian distribution near the origin, but deviates from the Gaussian at the tails. These characteristics are similar to the observations made by Kida & Tanaka [53] in their pseudo-spectral method calculation. The PDFs of vorticity shown in Fig. 4.11 show a close resemblance between the finite difference method and vortex method.

From these observations, it is fair to say that both the instantaneous and statistical features of the anisotropy are accurately calculated in the present vortex method. Our

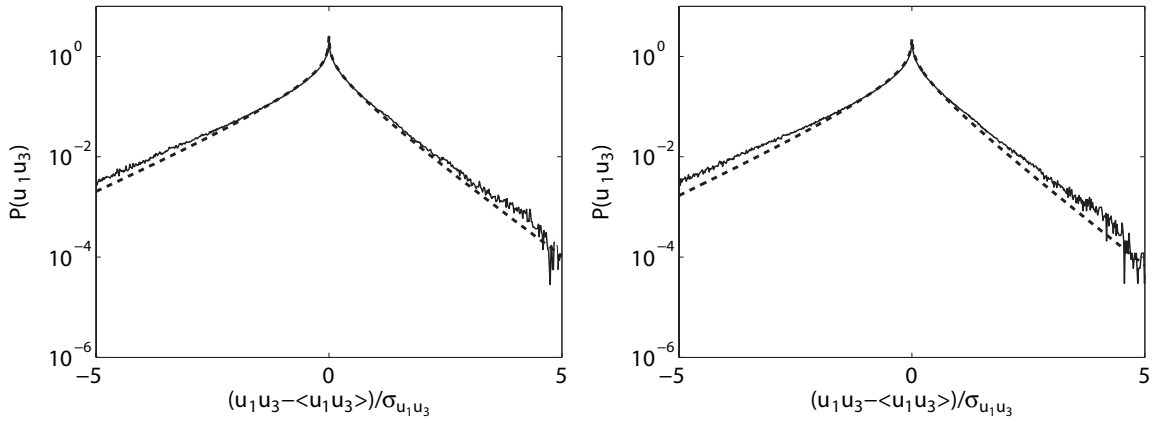

(a) $t^* = 0$ (FDM)

(b) $t^* = 0$ (VM)

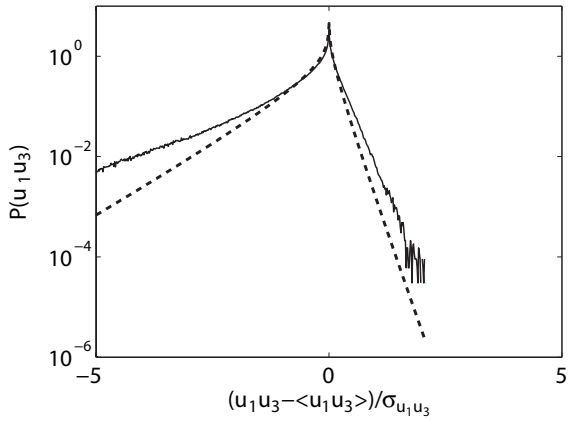

(c) $t^* = 2$ (FDM)

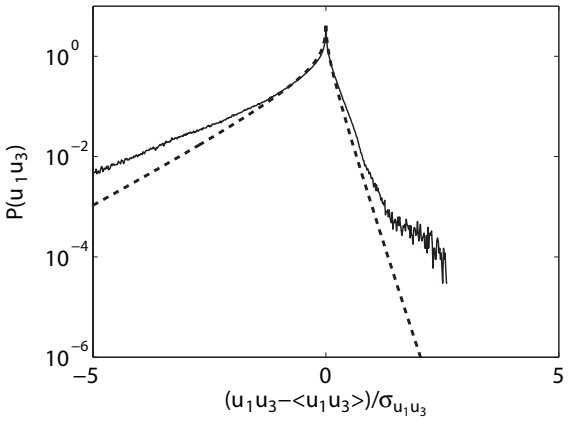

(d) $t^* = 2$ (VM)

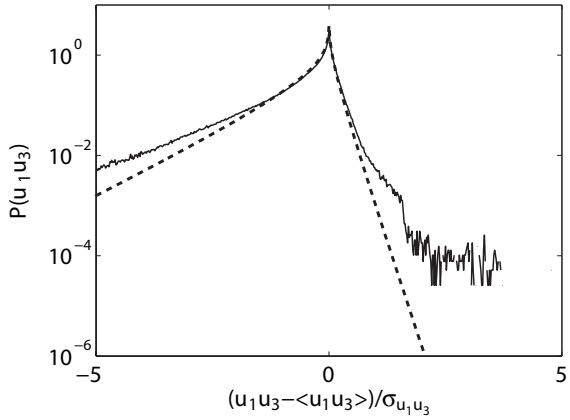

(e) $t^* = 4$ (FDM)

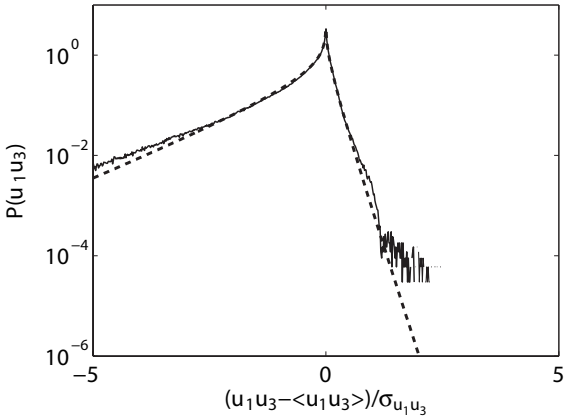

(f) $t^* = 4$ (VM)

Figure 4.9: PDF of u_1u_3

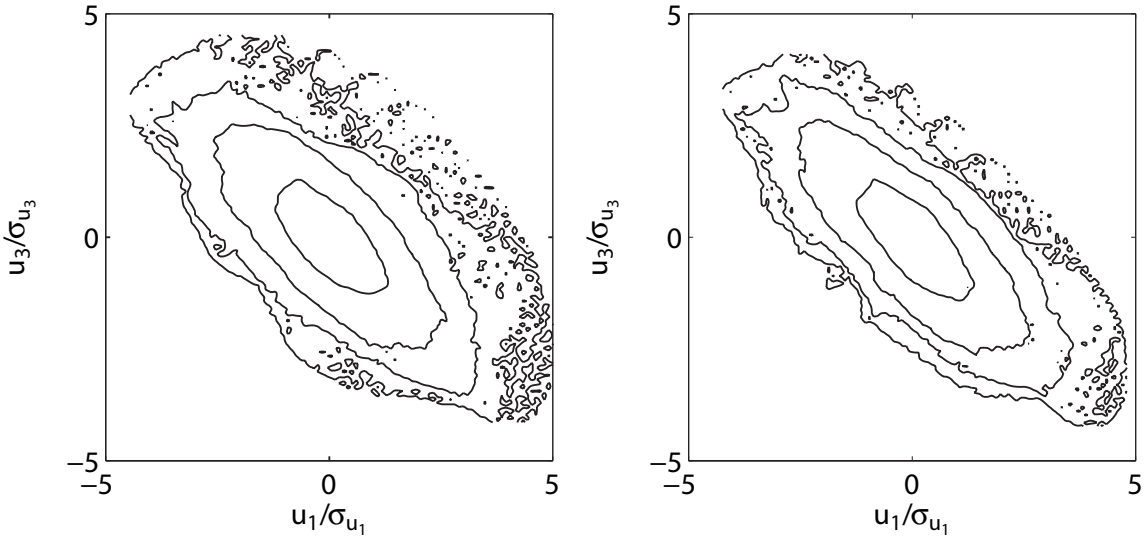

(a) FDM (b) VM

Figure 4.10: Joint PDF of u_1 and u_3 at $t^* = 4$

argument that the vortex method can reproduce globally anisotropic structures using locally isotropic elements has been supplemented from a statistical viewpoint by confirming the reproducibility of the global non-Gaussian turbulence using elements with local Gaussian smoothing.

4.3.6 Energy Spectrum Equation

The remaining objective of the present investigation is the quantitative assessment of the ability of vortex methods to calculate the balance between production, transfer, and dissipation in the homogeneous shear flow. Since the production was not present in the isotropic turbulence, its quantitative assessment is of interest for the present homogeneous shear calculation.

The energy spectrum equation for the homogeneous shear flow can be written as

$$\frac{\partial K}{\partial t} = \underbrace{Sk_1\frac{\partial K}{\partial k_3} - S\mathcal{E}_{13}}_{\mathcal{P}} + \underbrace{\iota k_k \mathcal{T}_{ik,i}}_{\mathcal{T}} - \underbrace{2\nu k^2 K}_{\epsilon}, \tag{4.32}$$

where $\mathcal{E}_{ij}$ and $\mathcal{T}_{ij,k}$ are the two point double and triple velocity correlation tensors in wavenumber space, respectively. (see Appendix D for details) K is the kinetic energy $K \equiv \frac{1}{2}\mathcal{E}_{ii}$, S is the shear-rate defined in Eq. (4.14), k is the wavenumber, and ν is the kinematic viscosity. Each term on the right hand side of Eq. (4.32) is associated with

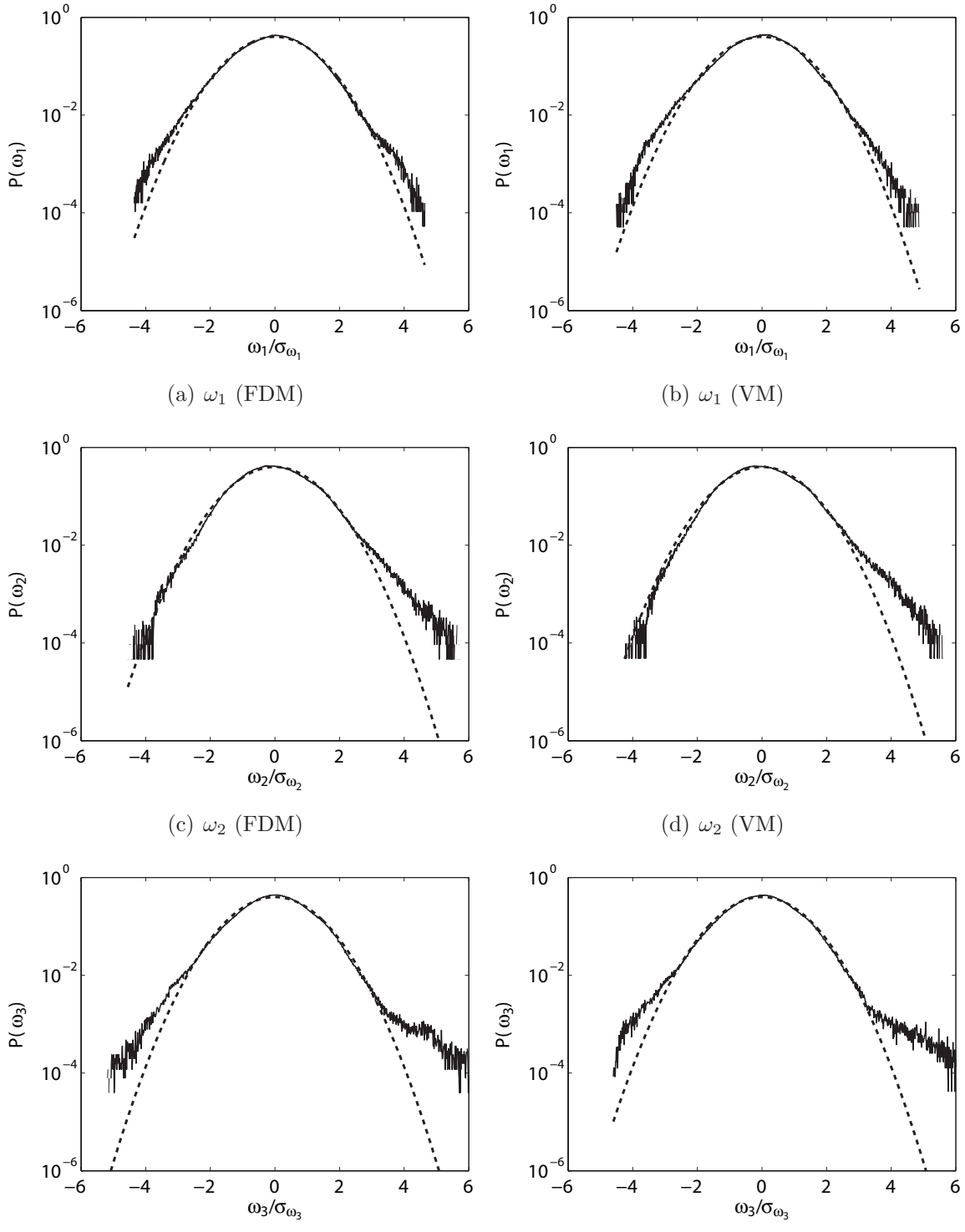

(a) ω_1 (FDM)

(b) ω_1 (VM)

(c) ω_2 (FDM)

(d) ω_2 (VM)

(e) ω_3 (FDM)

(f) ω_3 (VM)

Figure 4.11: PDF of ω_1, ω_2 and ω_3 at $t^* = 4$

an actual physical process. $\mathcal{P}$ represents the production, $\mathcal{T}$ represents the transfer, and ϵ represents the dissipation of the kinetic energy.

The budget of the above mentioned energy spectrum equation at $t^* = 2$ for the finite difference method and vortex method is shown in Fig. 4.12. Although there are quantitative differences in the two plots, the overall tendency is very similar. First, the production has a peak at lower wavenumbers and vanishes at higher wavenumbers. This corresponds to the fact that the mean shear mainly influences the large structures of turbulence. Secondly, the transfer term has a large negative value at lower wavenumbers and has a positive value at higher wavenumbers. This reflects the fact that the energy drawn from the larger structures is gradually cascaded down to the smaller structures. Furthermore, the dissipation term has a negative peak at higher wavenumbers, although not too high for the present calculation at $Re_\lambda = 25$. Finally, the change rate of kinetic energy shows an energy surplus, which is consistent with the fact that the total kinetic energy increases over time.

In summary, the vortex method can correctly calculate the contribution of the individual terms of the energy spectrum equation in the homogeneous shear flow. This rules out the possibility of errors canceling out to produce a plausible decay rate of kinetic energy in the vortex method calculations.

4.4 Conclusions

The FMM has been extended to periodic boundary conditions with shear. Using this shear periodic FMM, the vortex method has been applied to the calculation of a homogeneous shear turbulence, and compared with a finite difference code under identical calculation conditions.

The asymptotic behavior of the error in the present shear periodic FMM is identical to that of the periodic FMM without shear. The increase in CPU-time caused by the additional calculation of the shear periodic image cells is approximately 30% of the total CPU-time of the FMM.

The vortical structures observed in the isosurface plots of the second invariant of the velocity derivative tensor were in good accordance between the two methods. The difference of the normal components of the anisotropy tensor of the Reynolds stress between the vortex method and finite difference method is approximately 10% for $N = 64^3$ and 3% for $N = 128^3$. This indicates that the present vortex method can quantitatively match the results of the finite difference method if the spatial resolution is sufficient. Using

isotropic vortex blobs does not prevent the vortex method from accurately calculating anisotropic turbulence, because the flow is, to some extent, locally isotropic.

The probability density function for u_1u_3 differ by 1% at $t^* = 4$ between the vortex method and finite difference method. The agreement between the finite difference method and vortex method for the probability density functions shows that the vortex method reproduces the statistical aspects of the strongly sheared turbulence, accurately. Furthermore, the budget of the energy spectrum equation shows that the details of the energy transfer are also properly calculated in the present vortex method. The production differs approximately 5%, and the dissipation differs around 2%, while the discrepancy in the transfer term is approximately 10%.

From these observations, it is fair to conclude that the present vortex method is valid for solving flows with a shear-rate parameter of $S^* \approx 35$, which is equal to the maximum value observed in a fully developed channel flow. This allows us to rule out the possibility of any detrimental effects caused by the mean shear, when validating the vortex method for near-wall flows in the future. This also indicates the necessity of developing higher-order elliptic smoothing functions to match the convergence properties of grid-based methods.

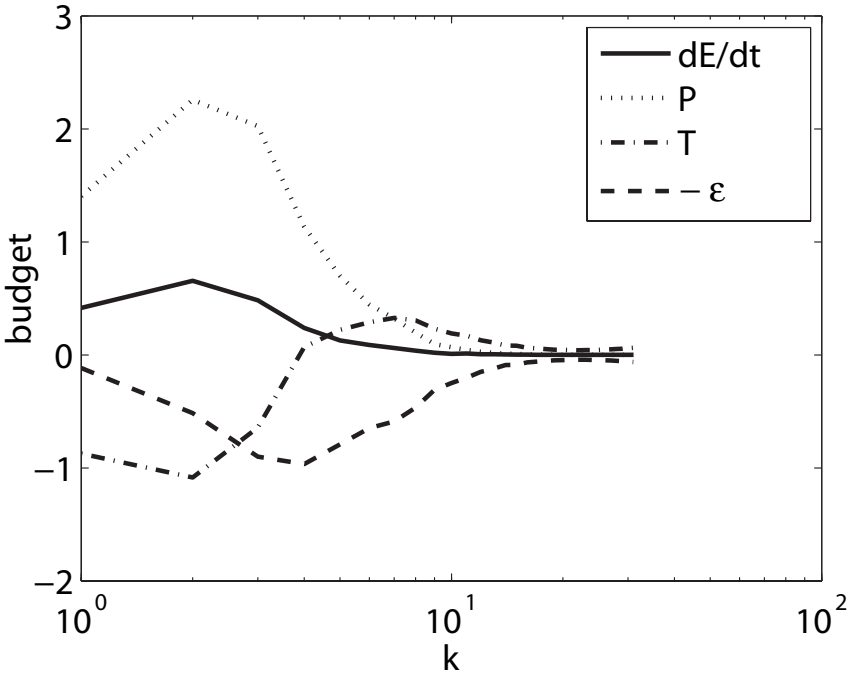

(a) FDM

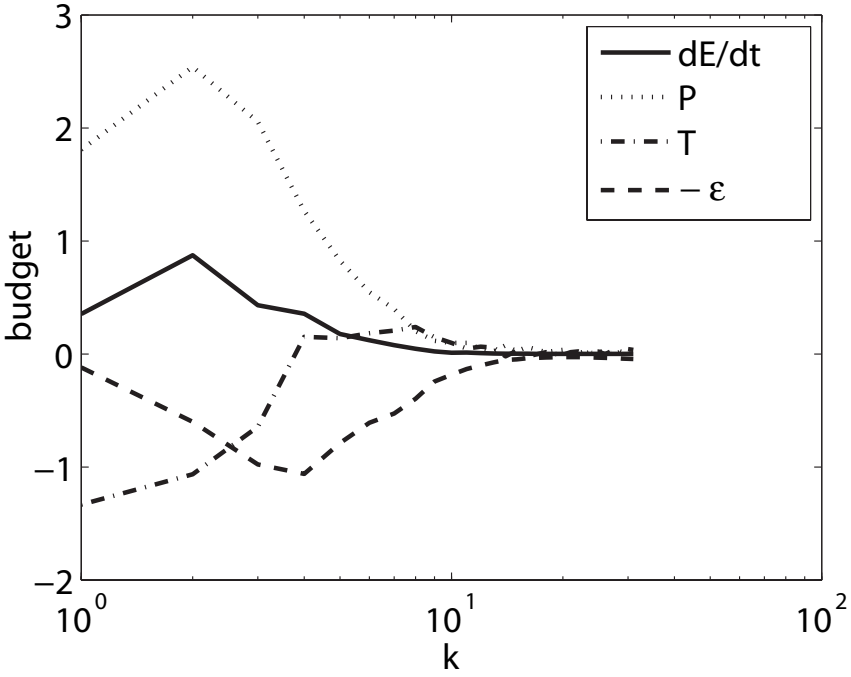

(b) VM

Figure 4.12: Budget of the Energy Spectrum Equation at $t^* = 2$

Chapter 5

Calculation of Channel Flow

5.1 Introduction

It has been over a decade since vortex methods were recognized as an interesting alternative to finite difference and spectral methods for the direct numerical simulation of turbulence. Yet, the successful application of vortex methods during the past decade has been limited to particular flows where the vorticity has a compact support and where the convection of vorticity is dominant, *e.g.* bluff body wakes,[21] and aircraft wakes.[54] [55] The solution of these flows by a finite difference method would require a larger calculation domain to impose the proper boundary conditions, and smaller time steps to satisfy the numerical stability conditions. Therefore, these flows serve the purpose of showing the comparative advantage of vortex methods over conventional grid based methods.

The fully developed turbulent channel flow on the other hand, has been thoroughly studied during the past two decades using finite difference and spectral methods, but scarcely calculated by vortex methods. Unlike the above mentioned external flows, vorticity fills the entire flow domain, so vortex methods do not have any advantage in terms of the size of the calculation domain. Furthermore, the periodicity in the streamwise and spanwise direction offer an advantage for grid based methods, but not for particle based vortex methods. Therefore, the turbulent channel flow is a challenging flow field for vortex methods in a relative sense. However, validating the performance of vortex methods by comparing the results with grid based direct numerical simulations for the channel flow shall help quantify the necessary spatial resolution near solid boundaries, and also facilitate the development of more efficient near wall treatment in vortex methods. The simplicity of the geometry and the availability of reference calculations shall prove to be convenient when analyzing the general performance of vortex methods near

solid boundaries.

Vortex methods face multiple challenges in the vicinity of a solid boundary. First, the vorticity-velocity formulation requires the vortex method to enforce a boundary condition for vorticity at the wall, which implicitly satisfies the no-slip condition for velocity. Accurately enforcing this boundary condition is crucial to vortex methods, since the entire calculation is strongly influenced by the vorticity at the wall.

Lighthill [56] used the concept of a factional step algorithm to describe the generation of vorticity at a solid boundary. However, he did not mention how this vorticity enters the fluid adjacent to the wall or how the vortex panel strength may be incorporated in a vorticity boundary condition. Chorin [10] incorporated the vorticity boundary condition into the random walk approach by creating vortex blobs at the boundary, which posses a vortex strength that enforces the no-slip boundary condition. This vortex strength obtained by dividing the strength of the vortex panel by a length equal to the elementary discretization length on the body. However, the use of radially symmetric blobs in the vicinity of a wall introduced an artificial smoothing region for the vorticity field. Chorin later proposed a vortex sheet method based on the Prandtl boundary layer equations. This method caused oscillations at the interface where the sheets turn into blobs. Moreover, this approximation does not hold for separated flows.

In terms of calculating the correct amount of vorticity at the wall, Wu [59] proposed a method that multiplies the strength of the vortex panel by the mesh size in the normal direction to obtain the vorticity on the body. Kinney and his co-workers [57] [58] envisioned the strength of the vortex panel as equivalent to a vorticity flux over a small time interval. Anderson [60] formed a Neumann boundary condition by suggesting that the time derivative of vorticity must be admissible. In this formulation the values of the vorticity on the boundary are coupled with both the velocity and vorticity in the fluid domain, which are in turn conditioned by the boundary values of the vorticity. Cottet [61] introduced an alternative formulation, where the boundary values of the velocity are represented in terms of the vorticity through the Poincaré formula.

Cottet [62] and Koumoutsakos *et al.* [19] independently proposed a fractional step method to replace the no-slip boundary condition with an equivalent vorticity flux condition. Cottet presented the algorithm as an extension of Chorin's vorticity creation algorithm, whereas Koumoutsakos *et al.* viewed it as an extension of the vorticity creation process envisioned by Lighthill [56] and formulated by Kinney and co-workers. [57] [58] In this method, the no-through boundary condition is accounted for by the distribution of vortex panels, and the strength of the vortex panels are distributed into the

flow by translating its strength into a Neumann boundary condition for the vorticity equation. Bernard [63] proposed a similar method, which uses the Fishlov's method to calculate the diffusion in the vicinity of the boundary for smooth vortex sheets.

Ploumhans & Winckelmans [20] improved the method by Koumoutsakos *et al.* by performing the spatial integration analytically, which results in better performance when the spatial resolution is low. A correction is also made to enforce conservation in the case where the spatial distribution of the particles are not well aligned with the vortex panels. Ploumhans *et al.* [21] then extended the method to three dimensional flows.

Another challenge regarding the near wall treatment of vortex methods is the effective use of anisotropic elements. In the vicinity of a solid boundary, both the velocity and vorticity have a large gradient in the direction normal to the boundary. Therefore, the calculation points must be closely spaced in the direction normal to the boundary. This causes the optimum shape of the vortex blobs to become anisotropic. There still remains ample room for investigation regarding the effective use of spatially varying anisotropic elements in vortex methods.

Marshall & Grant [64] used anisotropic vortex blobs with aspect ratios as high as 15 : 1, and obtained favorable results for the Blasius boundary layer. Cottet *et al.* [17] derived a consistent approximation using variable size vortex particles by combining several local mappings. Bergdorf *et al.* [65] extended this method to dynamically refine the computational domain and adapt accordingly its particle discretization. Two methods are proposed: one that pertains to r-adaptive finite element methods and another that is reminiscent of adaptive mesh refinement used in finite difference methods. Rossi [28] proposes an alternative adaptive vortex blob method, which can achieve fourth-order spatial accuracy using deforming basis functions. The method to evaluate the Biot-Savart integral for the elliptical Gaussian functions is also shown by Rossi. [66]

The present study aims to address the two issues mentioned above; the vorticity boundary condition and the use of adaptive vortex elements in a systematic manner, and thereby provide a guideline for the solution of the near wall problems in vortex methods. The turbulent channel flow is selected as a test case because of its simple geometry and the availability of numerical and experimental data, which can be used as both an initial condition and reference. It has become clear during the course of the investigation that a straightforward implementation of the methods proposed above, is not sufficient to reproduce the results of the finite difference method for more than one wash-out time. Therefore, the immediate goal is to extend the duration of quantitative agreement between the two methods, by improving the near wall calculation of the vortex

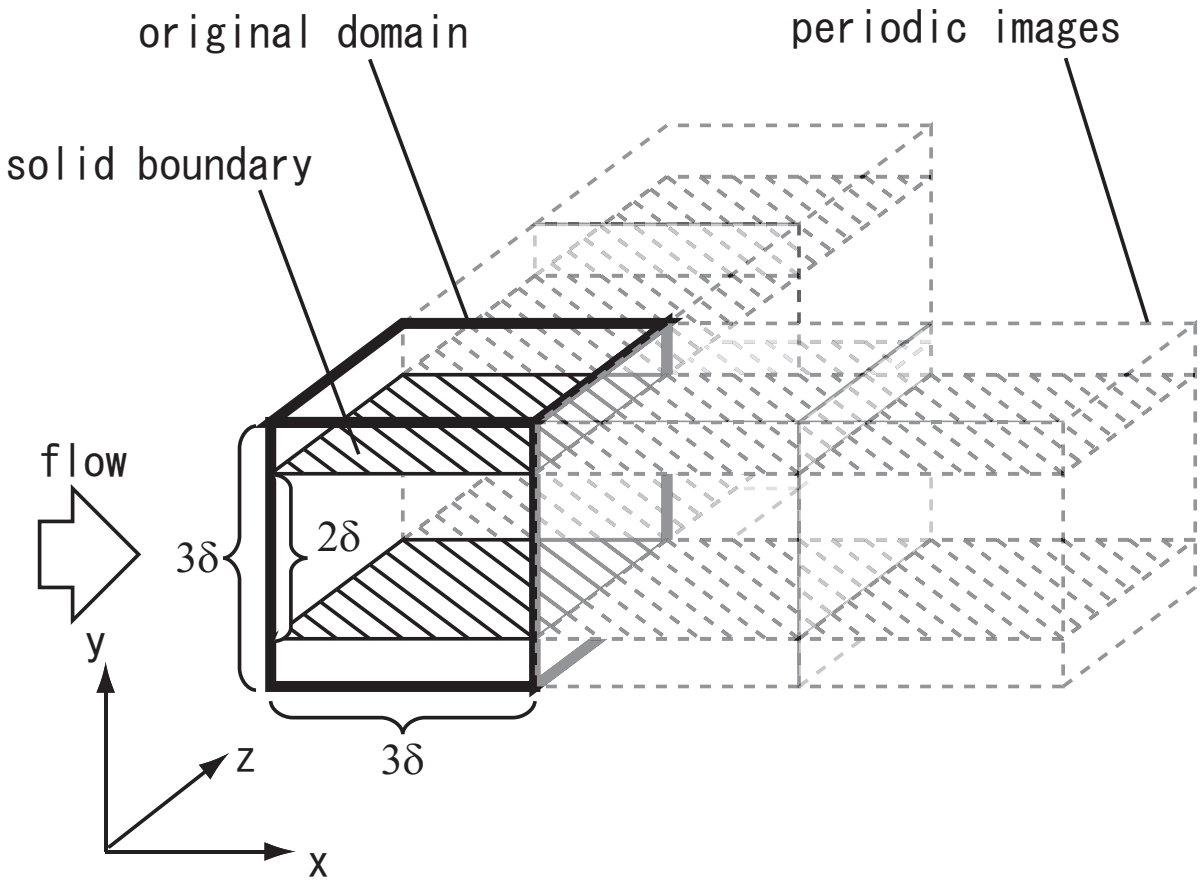

Figure 5.1: Schematic of the two-way periodic FMM

method.

5.2 Numerical Method

5.2.1 Two-Way Periodic Fast Multipole Method

The fast multipole method (FMM) has been extended to periodic boundary conditions by Lambert et al. [42]. They use a oct-tree structure for the subdomains, but group the periodic cells using a $3^k \times 3^k \times 3^k$ structure, where k is the number of periodic image cells per dimension. In the present FMM, a $2^k \times 2^k \times 2^k$ structure was used by leaving the original domain divided, while grouping with the outer cells. This allows the use of the original oct-tree structure of the FMM throughout the entire calculation. Thus, the complexity and error bounds directly follow that of the original FMM.

In the present calculation, the periodic FMM is modified to assume periodicity in only

two directions. A schematic of the two-way periodic FMM is shown in Fig. 5.1 along with the geometry of the flow field. The channel calculation is periodic in the streamwise (x) and spanwise (z) direction, while it has solid boudnaries in the transverse (y) direction. The size of the domain is $3\delta \times 2\delta \times 3\delta$, where δ is the channel half-width. The present calculation uses 32 periodic images per dimension, so the approximated domain size is $96\delta \times 2\delta \times 96\delta$. Similar to the results of our previous calculations, the calculation time to calculate for the $96\delta \times 2\delta \times 96\delta$ case is only 1% larger than the calculation time to calculate the $3\delta \times 2\delta \times 3\delta$ case (non-periodic boundary conditions). This is because the periodic image cells are grouped into one large multipole moment and calculated using the multipole-to-local translation of the FMM.

5.2.2 Vortex Method for Channel Flows

The present vortex method is an extention of the code used for the homogeneous isotropic turbulence, and the homogeneous shear flow. The primary difference is the boundary condition in the transverse (y) direction. The originally periodic boundary condition becomes a solid boundary as shown in Fig. 5.1. Due to this change, the vortex method must now account for the vorticity boundary condition at the wall. This boundary condition can be obtained from the diffusion part of the vorticity equation

$$\frac{D\boldsymbol{\omega}}{Dt} = \nu\nabla^2\boldsymbol{\omega}, \tag{5.1}$$

where ν is the kinematic viscosity and $\boldsymbol{\omega}$ is the vorticity vector. Taking the volume integral results in

$$\int_\Omega \frac{D\boldsymbol{\omega}}{Dt} d\Omega = \int_\Omega \nu\nabla^2\boldsymbol{\omega} d\Omega. \tag{5.2}$$

Taking into account the fact that t and ν are not a function of $\mathbf{x}$, we have

$$\frac{D\int_\Omega \boldsymbol{\omega} d\Omega}{Dt} = \int_\Omega \nabla\cdot(\nu\nabla\boldsymbol{\omega}) d\Omega. \tag{5.3}$$

Applying, Stokes' theorem to the left hand side and the divergence theorem to the right hand side yields

$$\frac{D\int_\Gamma \boldsymbol{\gamma} d\Gamma}{Dt} = \int_\Gamma \mathbf{n}\cdot(\nu\nabla\boldsymbol{\omega}) d\Gamma. \tag{5.4}$$

Therefore, we have

$$\int_\Gamma \frac{D\boldsymbol{\gamma}}{Dt} d\Gamma = \int_\Gamma \nu\frac{\partial\boldsymbol{\omega}}{\partial\mathbf{n}} d\Gamma, \tag{5.5}$$

on the boundary, and Eq. (5.2) in the entire domain. The solution to this integral equation can be expressed by a set of equations

$$\begin{cases} -\frac{1}{2}\boldsymbol{\mu} + \nu \int_\Gamma \frac{\partial G}{\partial \mathbf{n}} \boldsymbol{\mu} d\Gamma = \frac{D\boldsymbol{\gamma}}{Dt}, \\ \frac{D\boldsymbol{\omega}}{Dt} = \int_\Gamma G\boldsymbol{\mu} d\Gamma. \end{cases} \tag{5.6}$$

The first equation determines the diffusion potential $\boldsymbol{\mu}$, while the second equation determines the evolution of the vorticity. G is the Green's function of the diffusion equation and can be expressed as

$$G = \frac{1}{4\pi\nu t} \exp\left(-\frac{|\mathbf{x}|^2}{4\nu t}\right). \tag{5.7}$$

Substituting this Green's function into Eq. (5.6) and integrating for piecewise elements of size h with the wall normal direction being y yields

$$\frac{D\boldsymbol{\omega}}{Dt} = \frac{D\boldsymbol{\gamma}}{Dt} \frac{1}{2\sqrt{\pi}} \frac{1}{\sqrt{4\nu t}} \exp\left(-\frac{y^2}{4\nu t}\right) \left[\mathrm{erfc}(s)\right]_{(x-h/2)/\sqrt{4\nu t}}^{(x+h/2)/\sqrt{4\nu t}} \tag{5.8}$$

$$\left[\mathrm{erfc}(s)\right]_{(z-h/2)/\sqrt{4\nu t}}^{(z+h/2)/\sqrt{4\nu t}}. \tag{5.9}$$

For the present case where the wall is flat the rate of change of the panel strength is equivalent to the spurious slip at the wall that occurs every time step $\frac{D\boldsymbol{\gamma}}{Dt} = \frac{2\mathbf{u}_{slip}}{\Delta t}$. [55] When the mid-point rule $\left(t = \frac{\Delta t}{2}\right)$ is used for the time integration, the vortex strength due to the vorticity flux at the wall becomes

$$\Delta\boldsymbol{\alpha}_i = \int_0^{\Delta t} \int_{x_i-h_i/2}^{x_i+h_i/2} \int_{y_i-h_i/2}^{y_i+h_i/2} \int_{z_i-h_i/2}^{z_i+h_i/2} \frac{D\boldsymbol{\omega}_i}{Dt} dx dy dz dt \tag{5.10}$$

$$\begin{aligned} &= \sum_{j=1}^{N} 2\nu\mathbf{u}_{slip} \left[\mathrm{erfc}\left(\frac{y_{ij} - h_j/2}{\sqrt{2\nu\Delta t}}\right) - \mathrm{erfc}\left(\frac{y_{ij} + h_j/2}{\sqrt{2\nu\Delta t}}\right)\right] \\ &\left[\mathrm{ierfc}\left(\frac{x_{ij} + h_j}{\sqrt{2\nu\Delta t}}\right) + \mathrm{ierfc}\left(\frac{x_{ij} - h_j}{\sqrt{2\nu\Delta t}}\right) - 2\mathrm{ierfc}\left(\frac{x_{ij}}{\sqrt{2\nu\Delta t}}\right)\right] \\ &\left[\mathrm{ierfc}\left(\frac{z_{ij} + h_j}{\sqrt{2\nu\Delta t}}\right) + \mathrm{ierfc}\left(\frac{z_{ij} - h_j}{\sqrt{2\nu\Delta t}}\right) - 2\mathrm{ierfc}\left(\frac{z_{ij}}{\sqrt{2\nu\Delta t}}\right)\right], \end{aligned} \tag{5.11}$$

where

$$\mathrm{ierfc}(x) = \frac{1}{\pi}\exp(-x^2) - x\mathrm{erfc}(x).$$

$\mathrm{erfc}(x)$ is the complementary error function

$$\frac{2}{\sqrt{\pi}} \int_x^\infty e^{-t^2} dt. \tag{5.12}$$

It will be shown in section 5.3 that this method induces a quantitatively correct vorticity flux at the wall for the parameters used in the present calculations.

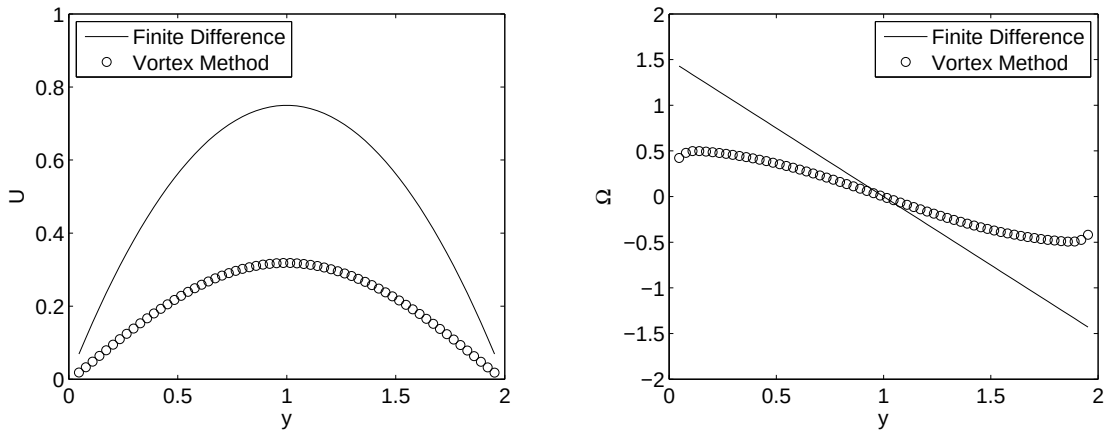

Figure 5.2: (a) Velocity distribution (b) Vorticity distirbution

5.2.3 Finite Difference Method for Channel Flows

The present finite difference calculation is based on the code by Fukagata et al.[67] The Navier-Stokes equation is discretized by using a energy conservative second-order scheme. [68, 69] The time integration is performed by the low storage third-order Runge-Kutta/Crank-Nicolson (RK3/CN) scheme, [70] along with the delta-form fractional step method. [71] The Poisson equation is solved by using the FFT in the streamwise and spanwise directions, and the tridiagonal matrix solver in the wall-normal direction.

5.3 Poiseuille Flow

The accuracy of the present wall boundary condition is tested for a laminar channel flow (Poiseuille Flow). The number of calculation points is $64 \times 64 \times 64$ in the $3\delta \times 2\delta \times 3\delta$ domain. The velocity distribution of a Poiseuille flow was given as the inital condition. The vortex elements were equally spaced, and the initial vortex strength $\boldsymbol{\alpha}$ was calculated by solving a system of equations for the Biot-Savart law using the BICGSTAB method. The bulk Reynolds number is set to $Re_b = U_b h/\nu = 10$, where

$$U_b = \frac{1}{2}\int_{-h/2}^{h/2} U dy \tag{5.13}$$

is the bulk velocity, h is the channel width, and ν is the kinematic viscosity. The $\Delta t = 0.02$ was determined from the CFL condition.

The results after 1000 time steps without the vorticity boundary condition is shown in Fig. 5.2. Note that initially, the velcoity and vorticity distribution of the vortex method

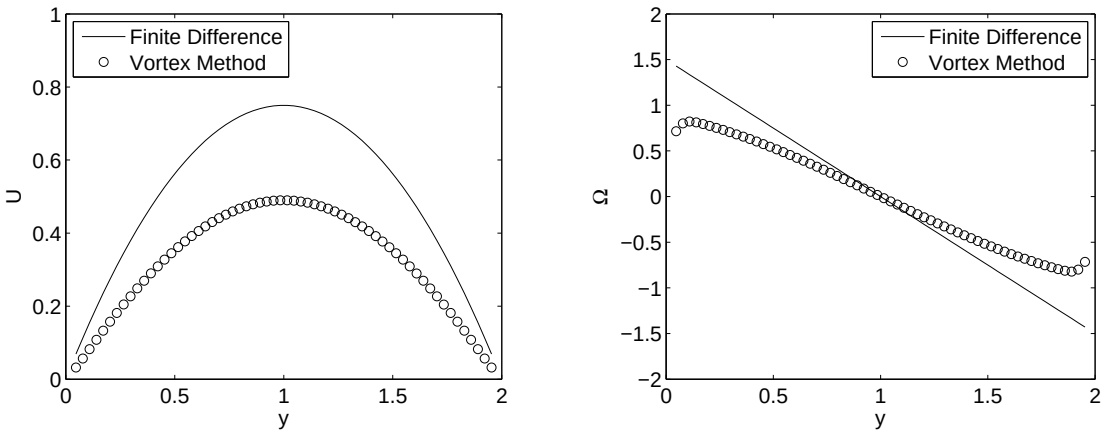

Figure 5.3: (a) Velocity distribution (b) Vorticity distirbution

match that of the Poiseuille flow (and the finite difference solution). As the calculation proceeds, the velocity of the vortex method decreases. This is caused by the lack of a driving force to maintain the channel flow. For the finite difference calculation, the mean pressure gradient appears as a force term in the Navier-Stokes equation. However, in the vorticity equation this term vanishes. By thinking of the driving force of the channel flow in terms of vorticity, it can be seen that it is necessary to give a proper vorticity flux at the solid boundary.

The results after 1000 times steps with the vorticity boundary condition is shown in Fig. 5.3. The velocity of the vortex method still decreases. This is the result of a straightforward implementation of the method shown in section 5.2.2. The suprious slip $\mathbf{u}_{slip}$ for this case is simply the result of calculating the Biot-Savart law to obtain the velocity at the wall points. As mentioned above, the vorticity equation itself does not contain a driving force, which drives the channel flow. The method shown in section 5.2.2 is merely a solution of this vorticity equation, with the proper boundary conditions. Note however, that the present solution equal to that of a zero pressure gradient (decelerating) channel with a Poiseuille initial condition. It has been comfirmed that the finite difference method gives the same results when the mean pressure gradient is set to zero. This is an important fact because the results shown in Fig. 5.3 are the solution to the Navier-Stokes equation (without a mean pressure gradient), whereas the results in Fig. 5.2 are not.

A method which will produce the results equivalent to solving the Navier-Stokes equation with the mean pressure gradient is shown below. When calculating the $\mathbf{u}_{slip}$, a constant velocity is added to the streamwise component. When this is done every time step, it produces the vorticity flux necessary for sustaining the flow rate. The

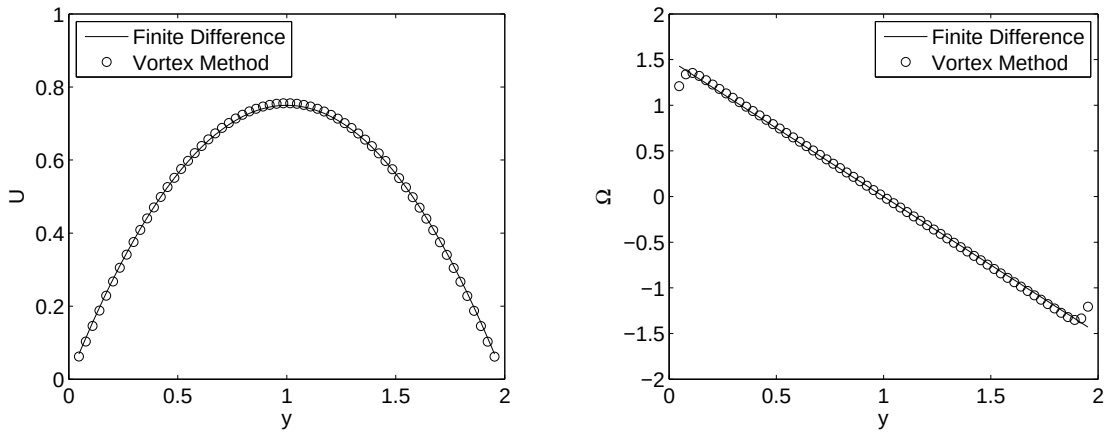

Figure 5.4: (a) Velocity distribution (b) Vorticity distirbution

results after 1000 time steps with the slip velocity correction is shown in Fig. 5.4. The results match the Poiseuille velocity profile. Therefore, the method shown in section 5.2.2 is satisfactory for enforcing the proper vorticity boundary condition at the wall, but requires modification of the slip velocity for internal flows, which are driven by the vorticy flux at the wall.

5.4 Turbulent Channel Flow

Following the results of the laminar calculations, the bulk Reynolds number is now increased to $Re_b = 5600$ for a turbulent channel flow calculation. The number of calculation points was $128 \times 128 \times 128$, and the size of the domain was kept to $3\delta \times 2\delta \times 3\delta$. First the finite difference method was executed until it achived an equilibrium state. The vortex method calculation and the reference calculation using the finite difference method were initialized by using this velocity field. The $\Delta t = 0.02$ was determined from the CFL condition of the finite difference method, and the vortex method used the same Δt. Remeshing was performed every 10 time steps to ensure the overlap of particles. The core radius was set to $\sigma = \Delta x = 3\delta/128$, which results in a overlap of 1 in the x and z direction, and 1.5 in the y direction.

The reproducibility of the initial condition of the turbulent channel flow using vortex elements is shown in the following plots. First the isosurface of the second invariant of the velocity gradient tensor are compared in Fig. 5.5. There are no notable differences in the shape of the isosurfaces, and even the small scale structures are reproduced.

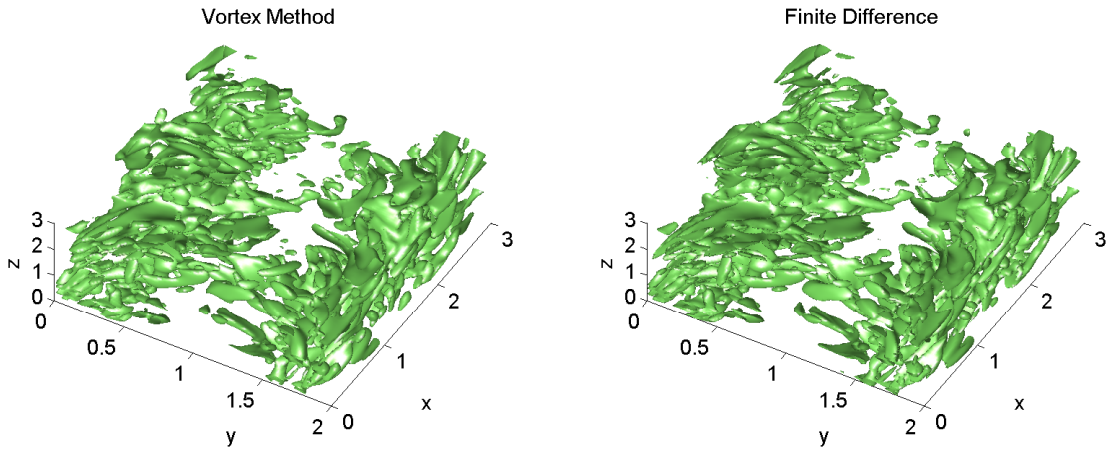

Figure 5.5: (a) Finite Difference (b) Vortex Method

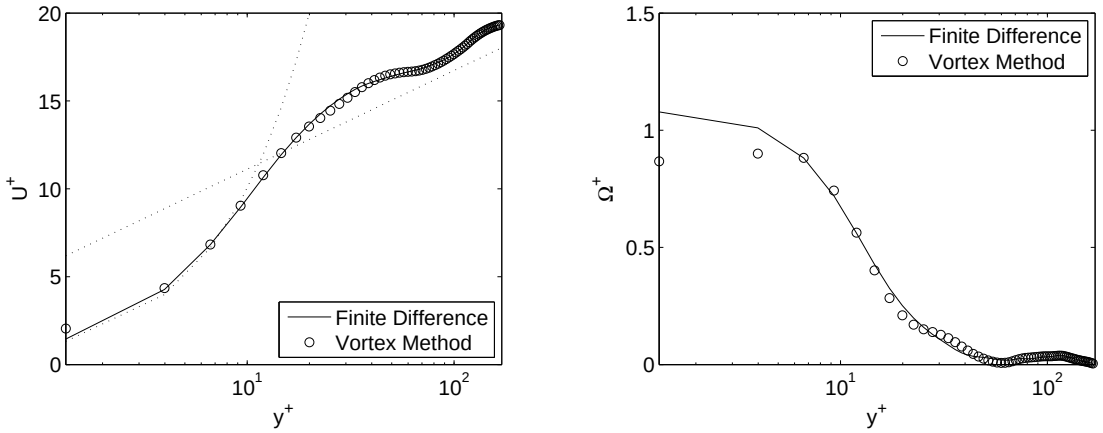

Figure 5.6: (a) Mean velocity (b) Mean Vorticity

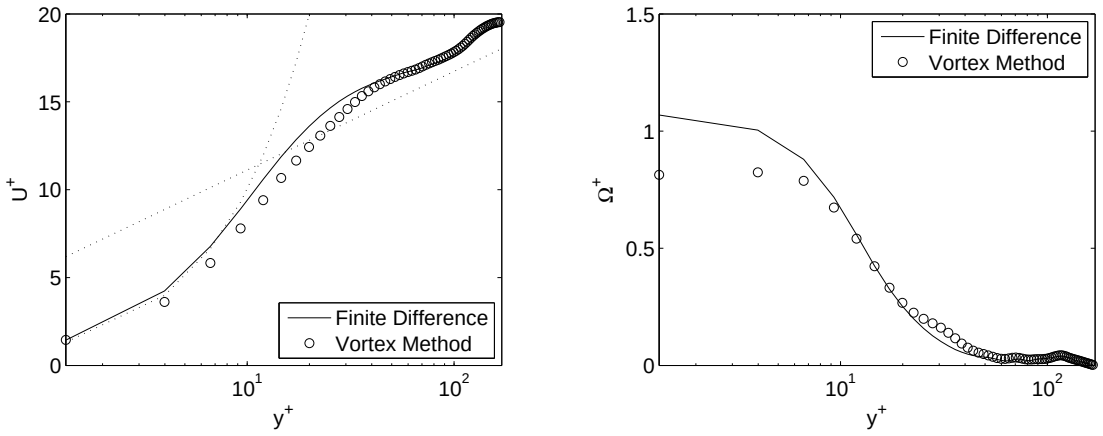

Figure 5.7: (a) Mean velocity (b) Mean Vorticity

The spatially averaged velocity and vorticity distirbution in the wall normal direction are shown in Fig. 5.6. The velcoity distribution matches completely between the two methods but is not on the $U^+ = \frac{1}{0.41}\log(y^+) + 5.5$. This is the problem in the finite difference method, where the near wall resolution and domain size are far from ideal. The restriction comes from the fact that the present vortex method cannot handle unequally-spaced elements, and will be addressed in the future. The focus is on the agreement between the finite difference method and vortex method. Another troubling feature is the deficit of vorticity very close to the wall. This is caused by the fact that there are no elements on the other side of the wall because the superposed vorticity decreases due to the absent sources. Previous studies [21, 55] use image particles to circumvent this problem. However, this is not a general solution for vortex methods with complex geometries.

The spatially averaged velocity and vorticity distirbution at $t = 2$ (100 time steps) are shown in Fig. 5.7. This is not a very long time in terms of wash out time, which is around 1. Nevertheless, the calculation blows-up shortly after this time so it is necessary to assess the problem using these results first. From Fig. 5.7(a) a velocity deficit can be observed in the buffer layer ($y^+ \approx 20 - 30$). In Fig. 5.7(b) a vorticity surplus can be seen in the same region. At this point, it is difficult to conjecture the true cause of this error. Thus, a parameter study for all adjustable parameters is performed in order to ascertain the ones that affect the results.

The accuracy of the discretization is the first thing to check. The time step size is changed to $\Delta t = 0.01$. The velocity and vorticity distribution at $t = 2$ (100 time steps) are shown in Fig. 5.8. The results do not change at all. Thus, it is fair to say that the

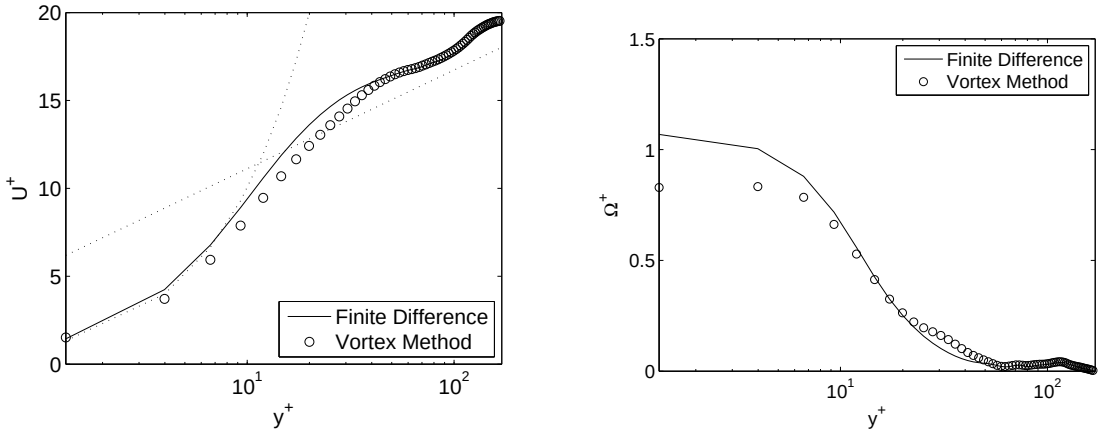

Figure 5.8: (a) Mean velocity (b) Mean Vorticity (Δt halfed)

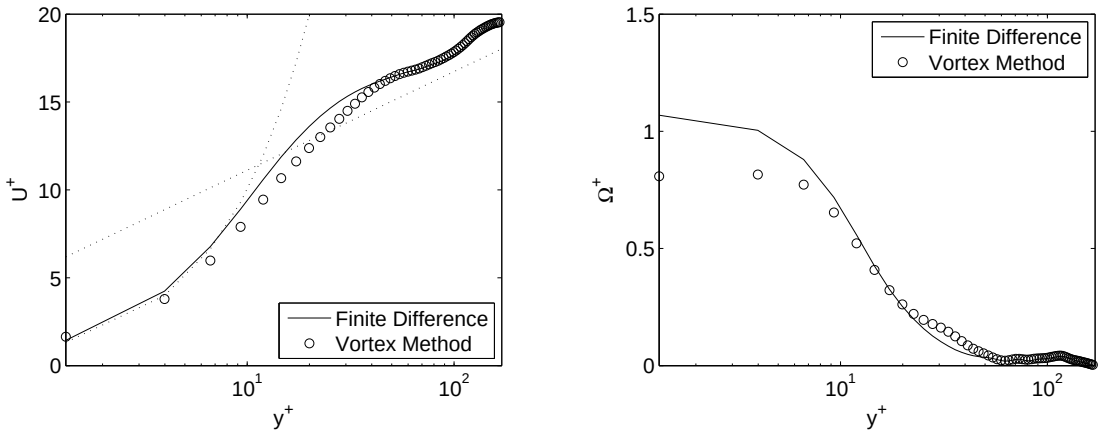

Figure 5.9: (a) Mean velocity (b) Mean Vorticity (frequent remeshing)

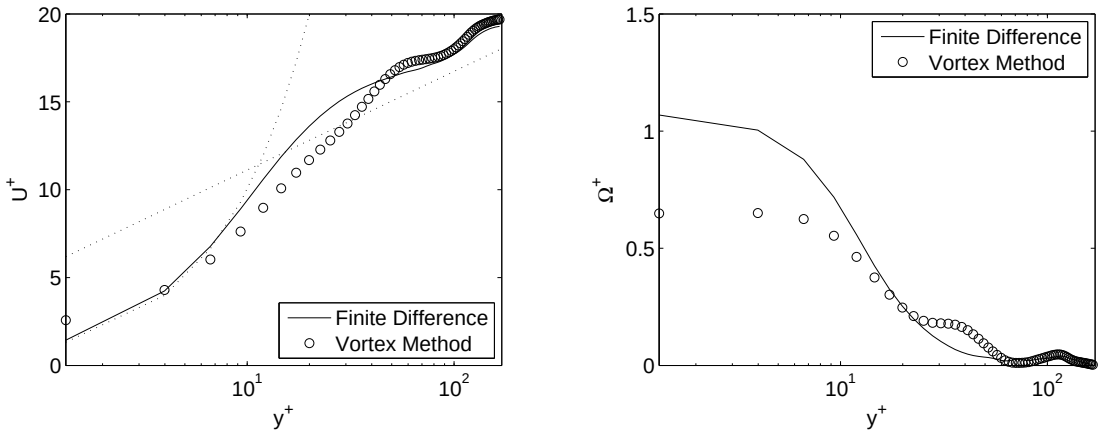

Figure 5.10: (a) Mean velocity (b) Mean Vorticity (larger overlap)

time step size is not the cause of the present error. Next, the frequency of remeshing is increased from every 10 steps to every 5 steps. This is also a common cause of error in vortex methods. The same results for the same time are shown in Fig. 5.9. Again, there is no notable improvement in the results. Therefore, it has been shown that the remeshing frequency is also not a primary contributor to the present velcoity deficit.

Another common cause of error in vortex methods is the overlap ratio of elements. The core radius is changed from Δx to $1.5\Delta x$ to check this. As seen in Fig. 5.10, the velocity deficit and vorticity surplus increase for this case. The core radius is the sole factor that determines the spatial resolution in vortex method calculations. Thus, the core radius must be kept small for higher spatial resolution, which requires the use of more vortex elements because they must overlap to acheive convergence. In the present case, enlarging the core radius decreased the accuracy of the calculation significantly. Therefore, the spatial resolution is a candidate for the contributing factors of the present problem.

Finally, a transposed scheme is used for the stretching term calculation. [16] This scheme has been known to produce smaller vorticity divergence. The velocity and vorticity distribution at $t = 2$ (100 time steps) are shown in Fig. 5.11. The results clearly improve for this case. The velocity mathces completely, and the vorticity matches except near the wall, for which the cause is known.

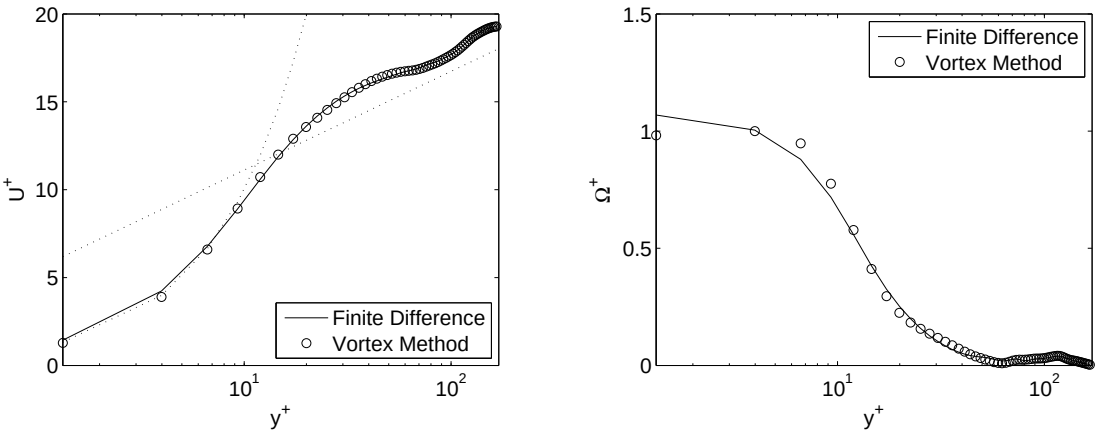

Figure 5.11: (a) Mean velocity (b) Mean Vorticity (transpose stretching)

5.5 Conclusions

The vortex method is compared with a finite differnce method for the direct numerical simulation of a turbulent channel of $Re_b = 5600$ ($Re_\tau = 180$). The fast multipole method (FMM) is modified to handle the periodic boundary conditions in the x and z direction, while retaining the free field boundary condition in the y (wall normal) direction. The calculation time for the periodic images was less than 1% of the entire FMM.

The present Neumann boundary condition of vorticity has been validated using the Poiseuille flow, where the necessity of an additional velocity slip to drive the internal flow was revealed. The quantitative accuracy of the present wall boundary condition can be seen from the results of the Poiseuille flow, where the difference between the vortex method calculation and the analytical solution is approximately 1%.

For the turbulent channel flow, the straightforward implementation of our method produces a large velocity deficit in the buffer layer, which results in a blow-up. The calculation using $N = 128^3$ elements, a time step size of $\Delta t = 0.02$, remeshing every 10 steps, a overlap ratio of $\sigma/\Delta x = 1$, and using the standard stretching scheme results in a 10% difference in the velocity profile between the vortex method and finite difference method.

A parameter study was performed in order to evaluate the sensitivity of each parameter. First, changing Δt changes the results by 0.1% at $t = 2$ and the discrepancy between the vortex method and finite difference method is still 10%. Second, changing the remeshing frequency changes the results by 0.5%. Third, increasing the overlap ratio for the same number of particles has a detrimental effect, and the results change by 50%

at $t = 2$. The difference between the velocity profile grows to 20% for this case. FInally, the transpose stretching scheme improves the results, and the difference between the vortex method and finite difference method drops to 0.5% at $t = 2$.

It is still necessary to increase the calculation time and also account for the vorticity deficit near the wall. These problems could be solved with the help of anisotropic vortex elements, and will be the foremost task in future studies.

Chapter 6

Conclusions

6.1 Achievements and Findings

The vortex method has been applied to the homogeneous isotropic turbulence, homogeneous shear flow, and turbulent channel flow, and compared with finite difference and spectral method calculations under the same conditions. The overall conclusions from the three calculations can be summarized as follows.

The main focus of the homogeneous turbulence calculation was to assess the ability of vortex methods to dissipate the kinetic energy properly. All results from the present calculations indicate that the vortex method can predict the dissipation rate correctly, if the following conditions are satisfied. First of all, the spatial resolution must be sufficient. The spectral method can stably calculate for $Re_\lambda = 50$ using $N = 64^3$ points, but the vortex method requires at least $N = 128^3$. Also, if the core spreading method is used, some form of spatial adaptation must be performed to keep the blob sizes from growing.

It maybe worth noting that the isotropic turbulence is a special case, where the Lagrangian distortion of particles remains small. Therefore, one must be carful when interpreting the present results to more general flows. Nevertheless, it has been made clear that the dissipation can be calculated accurately using vortex methods for a three dimensional turbulence.

The objective of the homogeneous shear flow calculation was to add the assessment of production into the above mentioned validation process. The anisotropy of the Reynolds stress showed that the present vortex method can quantitatively match the results of the finite difference method if the spatial resolution is sufficient. Using isotropic vortex blobs did not prevent the vortex method from accurately calculating anisotropic turbulence, because the flow was, to some extent, locally isotropic. The agreement between the finite

difference method and vortex method for the probability density functions showed that the vortex method reproduces the statistical aspects of the strongly sheared turbulence, accurately. Furthermore, the budget of the energy spectrum equation showed that the details of the energy transfer were also properly calculated in the present vortex method.

Finally, the channel flow was calculated in order to validate the wall boundary condition and near wall behavior of vortex methods. The previous two test cases served as an extremely useful reference to rule out the causes of discrepancy between the vortex method and finite difference methods. For the laminar case, our solution matched that of the Poiseuille profile for an arbitrarily long time. The agreement of the velocity profile for the laminar channel flow is an indicator of the successful implementation of the wall boundary conditions in our vortex method. However, for the turbulent channel flow, a straightforward implementation of the vortex method used in the previous two flows remained stable for a limited amount of time (one wash-out time). As was the case for the previous two test cases, the lack of spatial resolution is the most plausible explanation for this behavior. Due to the limitation of computational resources it was not possible to increase the number of vortex elements to confirm this. The use of spatially varying elliptic vortex elements could be a solution to this problem, and its development would be an interesting direction for future vortex methods.

In summary, the following facts were revealed for the first time from the results of the present validation process.

1. The discrepancy of the kinetic energy spectrum between the vortex method and spectral method is less than 1%, up to the dissipation wave number

2. The use of remeshing has minimal effect in an isotropic turbulence, where the results with and without remeshing differ only by 0.01%.

3. The new spatial adaptation technique allows the core spreading method to produce the same results as spectral methods until $t/T \approx 20$, where quantitative difference at $t/T \approx 20$ is approximately 3%

4. The difference of the normal components of the anisotropy tensor of the Reynolds stress between the vortex method and finite difference method is approximately 10% for the homogeneous shear flow at $S^* \approx 35$

5. Vortex methods can correctly predict the production, transfer, and dissipation of the kinetic energy, in the strongly sheared turbulence, where the production differs

approximately 5%, and the dissipation differs around 2%, while the discrepancy in the transfer term is approximately 10%

6. The present wall vortex boundary condition can reproduce and sustain the velocity profile of the Poiseuille flow, where the difference between the vortex method calculation and the analytical solution is approximately 1%

7. A straightforward implementation of the present vortex method technique causes the turbulent channel flow calculation to blow up after one wash-out time

8. The transpose stretching scheme improves the results, and the difference between the vortex method and finite difference method drops from 10% to 0.5% at $t = 2$

6.2 Future Work

The present validation studies have shown that the production and dissipation of turbulence can be handled accurately using vortex methods. Furthermore, the accuracy of the vortex methods indeed improves when the spatial resolution is increased. However, the present results indicate that the number of elements required to accurately calculate turbulence of a given Reynolds number is larger than finite difference and spectral methods.

6.2.1 Higher Order Spatial Discretization

The use of higher order smoothing functions is a possible candidate for achieving the necessary accuracy with minimum effort. This is an open area of research in many particle methods. This includes the use of elliptic vortex elements with a principal axis that can point in any direction.[28] These elements may also vary in size to adopt to the local particle density and ensure the overlap condition in all regions. [17] The radial basis function interpolation may allow the calculation of the vortex strength of such vortex elements. [30] The homogeneous isotropic turbulence maybe used as a test case to construct these high order elements.

6.2.2 Large Eddy Simulation

The above problem can also be solved by using sub-grid-scale (SGS) turbulence modeling, *i.e.* large eddy simulation (LES). There have already been a few attempts to incorporate

SGS models into vortex methods. [55] The homogeneous isotropic turbulence would be a natural selection for the flow field for validating SGS models. It would be interesting to compare the energy spectrum of the results of the present spectral method and the vortex method, with and without the SGS models. The homogeneous isotropic turbulence can also be used as a test case to construct these SGS models.

6.2.3 Fast N-body Solvers

These issues are also directly connected to the performance of fast N-body solvers, which determine the speed of the vortex method calculation. The efficiency of such fast N-body solvers on the next generation of highly data-parallel processors is of prime importance. There are plenty of techniques to efficiently parallelize grid based fast Poisson solvers, so the data-parallel architecture of the next generation processors may or may not be an advantage for particle based methods. Though, it is important to pursue further parallel efficiency of fast N-body solvers.

6.2.4 Turbulent Channel Flow

There is still some room for improvement regarding the turbulent channel flow calculation. The results of the vortex method only match that of the finite difference method for one wash-out time. The parameter study has shown that the transpose stretching scheme yields relatively favorable results, but the vorticity divergence seems to become exceedingly large for this case. This was not observed in the previous homogeneous flow calculations, and its cause is not well understood.

6.2.5 Application to Complex Flows

The three flow fields mentioned above are test cases for validating the vortex method, and can be used to validate new methods, new smoothing functions, and new SGS models in the future. At the same time, it is important to apply these methods to actual engineering applications to determine the effectiveness of vortex methods, and also establish the foundation of reliability based on these results.

Appendix A

Integral Equations

Unlike finite difference methods, where the differential equations are discretized directly, vortex methods transform the differential equations into integral equations before they are discretized. This approach is supported by a strong mathematical background, which consists of Fredholm integral equations, Green's functions, and Green's identities. Understanding the essence of these theories will enable one to predict the outcome of vortex method simulations to a greater extent, and also speed up the process of constructing novel algorithms for vortex methods. Studying vortex methods without understanding the above mentioned concepts would be like studying finite difference methods without knowing partial differential equations, Taylor expansions, or linear algebra. Therefore, in this chapter the minimum requirements to understand how the vortex method is justified from a mathematical viewpoint are presented.

A.1 Green's Functions

Let us consider the following Poisson equation at point $\mathbf{x}_i$.

$$\nabla^2 \mathbf{u}(\mathbf{x_i}) = \mathbf{f}(\mathbf{x_i}), \tag{A.1}$$

where $\mathbf{u}$ is the solution and $\mathbf{f}$ is the source term. By defining an operator $\mathcal{L} \equiv \nabla^2$, the equation can be written as

$$\mathcal{L}\mathbf{u}(\mathbf{x_i}) = \mathbf{f}(\mathbf{x_i}). \tag{A.2}$$

It is useful to define such an operator because the following approach is better explained with the help of the inverse operator $\mathcal{L}^{-1}$. This inverse operator is defined such that $\mathbf{L}\mathbf{L}^{-1} = \mathcal{I}$, where $\mathcal{I}$ is the identity operator. Since, the operator $\mathcal{L}$ is a differential operator, one may assume that $\mathcal{L}^{-1}$ is an integral operator. Then, the solution to Eq. (A.1)

can be written as

$$\mathbf{u}(\mathbf{x}_i) = \int G(\mathbf{x}_i, \mathbf{x}_j)\mathbf{f}(\mathbf{x}_j)d\mathbf{x}_j, \tag{A.3}$$

where G is the kernel of the integral operator, *i.e.* Green's function. This integral equation is called the Fredholm equation of the first kind. It integrates the sources at all points $\mathbf{x}_j$ to obtain the solution at $\mathbf{x}_i$. Also, from the property of the inverse operator, we have the relation

$$\mathcal{L}\mathcal{L}^{-1}\mathbf{u}(\mathbf{x}_i) = \mathbf{u}(\mathbf{x}_i). \tag{A.4}$$

This equation can be viewed as $\mathcal{L}^{-1}\mathbf{u}$ being the solution and $\mathbf{u}$ being the source term. In this case, the integral equation can be written as

$$\mathcal{L}^{-1}\mathbf{u}(\mathbf{x}_i) = \int G(\mathbf{x}_i, \mathbf{x}_j)\mathbf{u}(\mathbf{x}_j)d\mathbf{x}_j, \tag{A.5}$$

Then, one can write

$$\mathbf{u}(\mathbf{x}_i) = \mathcal{L}\mathcal{L}^{-1}\mathbf{u}(\mathbf{x}_i) = \int \mathcal{L}G(\mathbf{x}_i, \mathbf{x}_j)\mathbf{u}(\mathbf{x}_j)d\mathbf{x}_j. \tag{A.6}$$

This results in a relation between the solution $\mathbf{u}(\mathbf{x}_i)$ and the source $\mathbf{u}(\mathbf{x}_j)$. If this result is to be true for all continuous functions $\mathbf{u}$ it follows that $\mathcal{L}G(\mathbf{x}_i, \mathbf{x}_j)$ must be zero whenever $\mathbf{x}_i \neq \mathbf{x}_j$, and when $\mathbf{x}_i = \mathbf{x}_j$ the integral on the right must reduce identically to $\mathbf{u}(\mathbf{x}_i)$. This means that

$$\mathcal{L}G(\mathbf{x}_i, \mathbf{x}_j) = \delta(\mathbf{x}_i - \mathbf{x}_j), \tag{A.7}$$

where δ is the Dirac's δ-function. The kernel of the integral operator, which satisfies the above relation is called the Green's function of the differential operator $\mathcal{L}$.

A.2 Green's Identities

Suppose ϕ and ψ are arbitrary scalar values. Vector derivative identities yield

$$\nabla \cdot (\phi\nabla\psi) = \phi\nabla^2\psi + \nabla\phi \cdot \nabla\psi, \tag{A.8}$$

$$\nabla \cdot (\psi\nabla\phi) = \psi\nabla^2\phi + \nabla\psi \cdot \nabla\phi. \tag{A.9}$$

By integrating both sides and applying the divergence theorem, Eq. (A.8) becomes

$$\int_\Gamma \mathbf{n} \cdot (\psi\nabla\phi)d\Gamma = \int_\Omega (\psi\nabla^2\phi + \nabla\psi \cdot \nabla\phi)d\Omega. \tag{A.10}$$

This is the Green's first identity for scalars. Subtracting Eq. (A.9) from Eq. (A.8) yields

$$\nabla \cdot (\phi\nabla\psi - \psi\nabla\phi) = \phi\nabla^2\psi - \psi\nabla^2\phi. \tag{A.11}$$

Integrating both sides and applying the divergence theorem gives

$$\int_\Gamma \mathbf{n}\cdot(\phi\nabla\psi-\psi\nabla\phi)d\Gamma=\int_\Omega(\phi\nabla^2\psi-\psi\nabla^2\phi)d\Omega. \tag{A.12}$$

This is the Green's second identity for scalars. Now suppose $\mathbf{A}$ and $\mathbf{B}$ are arbitrary vectors. Vector derivative identities for dot products yield

$$\nabla\cdot(\mathbf{A}\nabla\cdot\mathbf{B})=(\nabla\cdot\mathbf{A})(\nabla\cdot\mathbf{B})+\mathbf{A}\cdot\nabla(\nabla\cdot\mathbf{B}), \tag{A.13}$$

$$\nabla\cdot(\mathbf{B}\nabla\cdot\mathbf{A})=(\nabla\cdot\mathbf{B})(\nabla\cdot\mathbf{A})+\mathbf{B}\cdot\nabla(\nabla\cdot\mathbf{A}). \tag{A.14}$$

By integrating both sides and applying the divergence theorem, Eq. (A.13) becomes

$$\int_\Gamma \mathbf{n}\cdot(\mathbf{A}\nabla\cdot\mathbf{B})d\Gamma=\int_\Omega\left[(\nabla\cdot\mathbf{A})(\nabla\cdot\mathbf{B})+\mathbf{A}\cdot\nabla(\nabla\cdot\mathbf{B})\right]d\Omega. \tag{A.15}$$

This is the Green's first identity for vector dot products. Subtracting Eq. (A.14) from Eq. (A.13) yields

$$\nabla\cdot(\mathbf{A}\nabla\cdot\mathbf{B}-\mathbf{B}\nabla\cdot\mathbf{A})=\mathbf{A}\cdot\nabla(\nabla\cdot\mathbf{B})-\mathbf{B}\cdot\nabla(\nabla\cdot\mathbf{A}). \tag{A.16}$$

Integrating both sides and applying the divergence theorem gives

$$\int_\Gamma \mathbf{n}\cdot(\mathbf{A}\nabla\cdot\mathbf{B}-\mathbf{B}\nabla\cdot\mathbf{A})d\Gamma=\int_\Omega\left[\mathbf{A}\cdot\nabla(\nabla\cdot\mathbf{B})-\mathbf{B}\cdot\nabla(\nabla\cdot\mathbf{A})\right]d\Omega. \tag{A.17}$$

This is the Green's second identity for vector dot products. On the other hand, Vector derivative identities for cross products yield

$$\nabla\cdot(\mathbf{A}\times\nabla\times\mathbf{B})=(\nabla\times\mathbf{A})\cdot(\nabla\times\mathbf{B})-\mathbf{A}\cdot\nabla\times(\nabla\times\mathbf{B}), \tag{A.18}$$

$$\nabla\cdot(\mathbf{B}\times\nabla\times\mathbf{A})=(\nabla\times\mathbf{B})\cdot(\nabla\times\mathbf{A})-\mathbf{B}\cdot\nabla\times(\nabla\times\mathbf{A}). \tag{A.19}$$

This can be easily derived from

$$\nabla\cdot(\mathbf{A}\times\mathbf{B})=(\nabla\times\mathbf{A})\cdot\mathbf{B}-\mathbf{A}\cdot(\nabla\times\mathbf{B}). \tag{A.20}$$

By integrating both sides and applying the divergence theorem, Eq. (A.18) becomes

$$\int_\Gamma \mathbf{n}\cdot(\mathbf{A}\times\nabla\times\mathbf{B})d\Gamma=\int_\Omega\left[(\nabla\times\mathbf{A})\cdot(\nabla\times\mathbf{B})-\mathbf{A}\cdot\nabla\times(\nabla\times\mathbf{B})\right]d\Omega. \tag{A.21}$$

This is the Green's first identity for vector cross products. Subtracting Eq. (A.18) from Eq. (A.19) gives

$$\nabla\cdot(\mathbf{A}\times\nabla\times\mathbf{B}-\mathbf{B}\times\nabla\times\mathbf{A})=\mathbf{B}\cdot\nabla\times(\nabla\times\mathbf{A})-\mathbf{A}\cdot\nabla\times(\nabla\times\mathbf{B}). \tag{A.22}$$

Integrating both sides and applying the divergence theorem gives

$$\int_\Gamma \mathbf{n} \cdot (\mathbf{A} \times \nabla \times \mathbf{B} - \mathbf{B} \times \nabla \times \mathbf{A}) d\Gamma$$
$$= \int_\Omega \left[\mathbf{B} \cdot \nabla \times (\nabla \times \mathbf{A}) - \mathbf{A} \cdot \nabla \times (\nabla \times \mathbf{B})\right] d\Omega. \tag{A.23}$$

This is the Green's second identity for vector cross products. There is only one type of Green's identity for scalars because the double vector derivative can only be applied to a scalar as a combination of a gradient and divergence. However, there are two types of Green's identities for vectors because the double vector derivative can be applied to a vector as a combination of a gradient and divergence and also a double curl. The relation between these two are

$$\nabla \times (\nabla \times \mathbf{A}) = \nabla(\nabla \cdot \mathbf{A}) - \nabla^2 \mathbf{A}. \tag{A.24}$$

Substituting this relation to the right hand side of Eq. (A.22) and adding Eq. (A.16) results in

$$\nabla \cdot (\mathbf{A}\nabla \cdot \mathbf{B} - \mathbf{B}\nabla \cdot \mathbf{A} + \mathbf{A} \times \nabla \times \mathbf{B} - \mathbf{B} \times \nabla \times \mathbf{A}) = \mathbf{A} \cdot \nabla^2 \mathbf{B} - \mathbf{B} \cdot \nabla^2 \mathbf{A}. \tag{A.25}$$

Integrating both sides and applying the divergence theorem gives

$$\int_\Gamma \mathbf{n} \cdot (\mathbf{A}\nabla \cdot \mathbf{B} - \mathbf{B}\nabla \cdot \mathbf{A} + \mathbf{A} \times \nabla \times \mathbf{B} - \mathbf{B} \times \nabla \times \mathbf{A}) d\Gamma$$
$$= \int_\Omega (\mathbf{A} \cdot \nabla^2 \mathbf{B} - \mathbf{B} \cdot \nabla^2 \mathbf{A}) d\Omega. \tag{A.26}$$

This is a unique form of the Green's second identity for vectors, and is the relation commonly used to derive the general Biot-Savart equation.

A.3 Generalized Biot-Savart Equation

The Poisson equation for velocity can be easily obtained from the vector relation

$$\nabla \times \nabla \times \mathbf{u} = \nabla(\nabla \cdot \mathbf{u}) - \nabla^2 \mathbf{u}. \tag{A.27}$$

For an incompressible flow ($\nabla \cdot \mathbf{u} = 0$) this reduces to

$$\nabla^2 \mathbf{u} = -\nabla \times \boldsymbol{\omega}. \tag{A.28}$$

The analogy is very similar to that of the Poisson equation for pressure, where the continuity equation is also used as an extra constraint during the derivation. Solving

these Poisson equations can be thought of as a relaxation process in order to achieve continuity.

For the weighted residual formulation with the fundamental solution G as the weighting function, the Poisson equation becomes

$$\int_\Omega G\nabla^2\mathbf{u}d\Omega = -\int_\Omega G(\nabla\times\boldsymbol{\omega})d\Omega. \tag{A.29}$$

From Green's second identity for scalars Eq. (A.17) one obtains

$$\int_\Omega \mathbf{u}\nabla^2 G d\Omega + \int_\Gamma \mathbf{n}\cdot\left[G\nabla\mathbf{u} - (\nabla G)\mathbf{u}\right]d\Gamma = -\int_\Omega G(\nabla\times\boldsymbol{\omega})d\Omega, \tag{A.30}$$

and from the definition of the fundamental solution the first term becomes $-\mathbf{u}$ for an interior point, $-1/2\mathbf{u}$ for a boundary point, and zero for an exterior point. One should be careful upon using the Green's identity for scalars when $\mathbf{u}$ is actually a vector. The only part effected by this inconsistency is the second term of the surface integral $(\nabla G)\mathbf{u}$. Direct substitution of $\phi = G$ and $\psi = \mathbf{u}$ to Eq. (A.17) yields $\mathbf{u}\nabla G$, but this conflicts with the fact that the normal vector must act on ∇ and not $\mathbf{u}$ so it must be $(\nabla G)\mathbf{u}$. The right hand side of Eq. (A.30) contains $\nabla\times\boldsymbol{\omega}$, so this differential operator acting on $\boldsymbol{\omega}$ is quite annoying. This can be removed by the use of vector identities, and the result is called the generalized Biot-Savart law. The generalized Biot-Savart law can be derived directly from Eq. (A.30), and also from Green's second identity for vectors Eq. (A.26). This may seem like a simple exercise, but the discrepancies in the formulation among the many researchers of the vortex method is quite confusing and must be generalized in some way. Therefore, a detailed derivation is given here to clarify the relation between Eq. (A.30) and the general Biot-Savart law, and also a straightforward derivation from Eq. (A.26) is shown as means to give some physical insight into the problem.

Derivation from equation Eq. (A.30)

By applying the vector identity $\phi(\nabla\times\mathbf{A}) = \nabla\times(\phi\mathbf{A}) + \mathbf{A}\times\nabla\phi$ to Eq. (A.30) one has

$$\int_\Omega \mathbf{u}\nabla^2 G d\Omega + \int_\Gamma \mathbf{n}\cdot\left[G\nabla\mathbf{u} - (\nabla G)\mathbf{u}\right] + \mathbf{n}\times(G\boldsymbol{\omega})d\Gamma = -\int_\Omega(\boldsymbol{\omega}\times\nabla G)d\Omega. \tag{A.31}$$

Using the definition $\boldsymbol{\omega} = \nabla\times\mathbf{u}$, the vector equation inside the boundary integral becomes

$$\mathbf{n}\cdot G\nabla\mathbf{u} - \mathbf{n}\cdot(\nabla G)\mathbf{u} + \mathbf{n}\times(G\nabla\times\mathbf{u}). \tag{A.32}$$

G is a scalar and may be taken outside of the vector equation unless it is differentiated so

$$-\mathbf{n}\cdot(\nabla G)\mathbf{u} + G\left[\mathbf{n}\cdot\nabla\mathbf{u} + \mathbf{n}\times(\nabla\times\mathbf{u})\right]. \tag{A.33}$$

Applying the vector identity $\mathbf{A}\cdot\nabla\mathbf{B}+\mathbf{A}\times(\nabla\times\mathbf{B})=\mathbf{A}\nabla\cdot\mathbf{B}+(\mathbf{A}\times\nabla)\times\mathbf{B}$ to the second and third term gives

$$-\mathbf{n}\cdot(\nabla G)\mathbf{u}+G\left[\mathbf{n}\nabla\cdot\mathbf{u}+(\mathbf{n}\times\nabla)\times\mathbf{u}\right]. \tag{A.34}$$

For an incompressible flow $\nabla\cdot\mathbf{u}=0$, so the second term can be deleted. Furthermore, using the vector identity $\phi(\mathbf{n}\times\nabla)\times\mathbf{A}=(\mathbf{n}\times\nabla)\times(\phi\mathbf{A})-(\mathbf{n}\times\nabla\phi)\times\mathbf{A}$ on the third term yields

$$-\mathbf{n}\cdot(\nabla G)\mathbf{u}+(\mathbf{n}\times\nabla)\times(G\mathbf{u})-(\mathbf{n}\times\nabla G)\times\mathbf{u}. \tag{A.35}$$

The second term can be erased by recalling that $\int_\Gamma(\mathbf{n}\times\nabla)\times\mathbf{A}d\Gamma=\int_\Omega(\nabla\times\nabla)\times\mathbf{A}d\Omega=0$. The result is

$$-\mathbf{n}\cdot(\nabla G)\mathbf{u}-(\mathbf{n}\times\nabla G)\times\mathbf{u}. \tag{A.36}$$

Finally, from the vector identity $(\mathbf{A}\cdot\mathbf{B})\mathbf{C}+(\mathbf{A}\times\mathbf{B})\times\mathbf{C}=(\mathbf{A}\cdot\mathbf{C})\mathbf{B}+(\mathbf{A}\times\mathbf{C})\times\mathbf{B}$ one obtains

$$-(\mathbf{n}\cdot\mathbf{u})\nabla G-(\mathbf{n}\times\mathbf{u})\times\nabla G, \tag{A.37}$$

so the entire equation looks like

$$\int_\Omega\mathbf{u}\nabla^2G d\Omega-\int_\Gamma\left[(\mathbf{n}\cdot\mathbf{u})\nabla G+(\mathbf{n}\times\mathbf{u})\times\nabla G\right]d\Gamma=-\int_\Omega(\boldsymbol{\omega}\times\nabla G)d\Omega. \tag{A.38}$$

This is the general Biot-Savart law. The details of this equation will be discussed after showing another form of derivation.

Derivation from equation Eq. (A.26)

This sequence requires the use of the vector potential $\boldsymbol{\Psi}$ and the vector fundamental solution $\mathbf{G}=\nabla G\times\mathbf{a}$, where $\mathbf{a}$ is an arbitrary unit vector. The vector potential satisfies the following relations.

$$\nabla\cdot\boldsymbol{\Psi}=0, \tag{A.39}$$

$$\nabla\times\boldsymbol{\Psi}=\mathbf{u}, \tag{A.40}$$

$$\nabla^2\boldsymbol{\Psi}=-\boldsymbol{\omega}. \tag{A.41}$$

The first constraint is called the Coulomb gauge and is necessary for $\boldsymbol{\Psi}$ to be a unique potential. The second is the definition of $\boldsymbol{\Psi}$ and the third can be derived from the first two. The vector fundamental solution also has similar properties such as

$$\nabla\cdot\mathbf{G}=0, \tag{A.42}$$

$$\nabla\times\mathbf{G}=\nabla(\mathbf{a}\cdot\nabla G)+\mathbf{a}\nabla^2G, \tag{A.43}$$

$$\nabla^2\mathbf{G}=\nabla\times(\mathbf{a}\nabla^2G). \tag{A.44}$$

These three relations are the subsequence of vector identities. By substituting $\mathbf{\Psi}$ and $\mathbf{G}$ into the Green's second identity for vectors Eq. (A.26) one obtains

$$\begin{aligned}&\int_\Gamma \mathbf{n}\cdot(\mathbf{\Psi}\nabla\cdot\mathbf{G}-\mathbf{G}\nabla\cdot\mathbf{\Psi}+\mathbf{\Psi}\times\nabla\times\mathbf{G}-\mathbf{G}\times\nabla\times\mathbf{\Psi})d\Gamma\\&=\int_\Omega(\mathbf{\Psi}\cdot\nabla^2\mathbf{G}-\mathbf{G}\cdot\nabla^2\mathbf{\Psi})d\Omega.\end{aligned}\tag{A.45}$$

Using the relations Eq. (A.39) through Eq. (A.44) along with the definition $\mathbf{G}=\nabla G\times\mathbf{a}$, this equation becomes

$$\begin{aligned}&\int_\Gamma \underbrace{\mathbf{n}\cdot\left\{\mathbf{\Psi}\times\left[\nabla(\mathbf{a}\cdot\nabla G)+\mathbf{a}\nabla^2 G\right]\right\}}_{(a)}-\underbrace{\mathbf{n}\cdot[(\nabla G\times\mathbf{a})\times\mathbf{u}]}_{(b)}d\Gamma\\&=\int_\Omega\underbrace{\mathbf{\Psi}\cdot\nabla\times(\mathbf{a}\nabla^2 G)}_{(c)}+\underbrace{(\nabla G\times\mathbf{a})\cdot\boldsymbol{\omega}d\Omega}_{(d)}.\end{aligned}\tag{A.46}$$

We will first deal with part (a). $\nabla^2 G$ is zero at the boundary so the boundary integral of $\mathbf{a}\nabla^2 G$ is zero. Applying the vector identity $\mathbf{A}\times\nabla\phi=-\nabla\times(\phi\mathbf{A})+\phi\nabla\times\mathbf{A}$ to the remaining term gives

$$(a)=-\int_\Gamma\mathbf{n}\cdot\nabla\times[(\mathbf{a}\cdot\nabla G)\mathbf{\Psi}]\,d\Gamma+\int_\Gamma\mathbf{n}\cdot[(\mathbf{a}\cdot\nabla G)\nabla\times\mathbf{\Psi}]\,d\Gamma.\tag{A.47}$$

The first term can be erased by recalling that $\int_\Gamma\mathbf{n}\cdot\nabla\times\mathbf{A}d\Gamma=\int_\Omega\nabla\cdot\nabla\times\mathbf{A}d\Omega=0$. From the definition of the vector potential the remaining term becomes

$$\int_\Gamma\mathbf{n}\cdot[\mathbf{u}(\mathbf{a}\cdot\nabla G)]\,d\Gamma,\tag{A.48}$$

and can also be rewritten in the form

$$\int_\Gamma(\mathbf{n}\cdot\mathbf{u})\nabla G\cdot\mathbf{a}d\Gamma.\tag{A.49}$$

Part (b) requires only one transformation, which makes use of the vector identity $\mathbf{A}\cdot[(\mathbf{B}\times\mathbf{C})\times\mathbf{D}]=[(\mathbf{D}\times\mathbf{A})\times\mathbf{B}]\cdot\mathbf{C}$. The result is

$$(b)=\int_\Gamma[(\mathbf{u}\times\mathbf{n})\times\nabla G]\cdot\mathbf{a}d\Gamma.\tag{A.50}$$

Part (c) is transformed by the vector identity $\mathbf{A}\cdot(\nabla\times\mathbf{B})=(\nabla\times\mathbf{A})\cdot\mathbf{B}-\nabla\cdot(\mathbf{A}\times\mathbf{B})$, which yields

$$(c)=\int_\Omega(\nabla\times\mathbf{\Psi})\cdot(\mathbf{a}\nabla^2 G)-\nabla\cdot\left[\mathbf{\Psi}\times(\mathbf{a}\nabla^2 G)\right]d\Omega.\tag{A.51}$$

Applying the definition of the vector potential to the first term and the divergence theorem to the second gives

$$\int_\Omega \mathbf{u}\nabla^2 G \cdot \mathbf{a} d\Omega - \int_\Gamma \mathbf{n} \cdot \left[\mathbf{\Psi} \times (\mathbf{a}\nabla^2 G)\right] d\Gamma. \tag{A.52}$$

Here again, the boundary integral of $\mathbf{a}\nabla^2 G$ is zero so

$$\int_\Omega \mathbf{u}\nabla^2 G \cdot \mathbf{a}. \tag{A.53}$$

Finally, part (d) is transformed using $(\mathbf{A} \times \mathbf{B}) \cdot \mathbf{C} = (\mathbf{C} \times \mathbf{A}) \cdot \mathbf{B}$, which gives

$$(d) = \int_\Omega (\boldsymbol{\omega} \times \nabla G) \cdot \mathbf{a}. \tag{A.54}$$

When these results are summarized the final equation is

$$\int_\Gamma (\mathbf{n} \cdot \mathbf{u})\nabla G \cdot \mathbf{a} - [(\mathbf{u} \times \mathbf{n}) \times \nabla G] \cdot \mathbf{a} d\Gamma = \int_\Omega \mathbf{u}\nabla^2 G \cdot \mathbf{a} + (\boldsymbol{\omega} \times \nabla G) \cdot \mathbf{a} d\Omega. \tag{A.55}$$

Since $\mathbf{a}$ is an arbitrary vector it can be removed from the equation, therefore end up with an equation identical to Eq. (A.38). For the sake of clarity, the equation is shown again.

$$\int_\Omega \mathbf{u}\nabla^2 G d\Omega - \int_\Gamma [(\mathbf{n} \cdot \mathbf{u})\nabla G + (\mathbf{n} \times \mathbf{u}) \times \nabla G] \, d\Gamma = -\int_\Omega (\boldsymbol{\omega} \times \nabla G) d\Omega.$$

Here again, the first term becomes $-\mathbf{u}$ for an interior point, $-1/2\mathbf{u}$ for a boundary point, and zero for an exterior point. The second term on the left hand side represents the contribution to/of the boundary values, where $\mathbf{n} \cdot \mathbf{u}$ is the velocity normal to the boundary, and $\mathbf{n} \times \mathbf{u}$ is the velocity tangent to the boundary.

Appendix B

Alternative Forms of Equations

B.1 Alternative Smoothing Functions

In a numerical sense, calculating the exponential functions and error functions for a N-body calculation is time consuming, and the Gaussian function is not the only choice for the smoothing function. Smoothing functions only need to satisfy certain moment properties

$$\begin{cases} \int \zeta_\sigma(\mathbf{x})d\mathbf{x} = 1 & \\ \int \mathbf{x}^{\mathbf{i}}\zeta_\sigma(\mathbf{x})d\mathbf{x} = 0 & 1 \leq |\mathbf{i}| \leq r-1 \\ \int |\mathbf{x}|^r|\zeta_\sigma(\mathbf{x})|d\mathbf{x} < \infty. & \end{cases}$$

Winckelmans *et al.*[40] gives a thorough review of the many different forms of two dimensional and three dimensional smoothing functions. A list of smoothing functions is

shown below.

$2-D$	*Low order algebraic*	$\frac{1}{\pi}\frac{\sigma^2}{(\lvert\mathbf{x}\rvert^2+\sigma^2)^2}$
	High order algebraic	$\frac{2}{\pi}\frac{\sigma^4}{(\lvert\mathbf{x}\rvert^2+\sigma^2)^3}$
	Super algebraic	$\frac{2\sigma^4}{\pi}\frac{2\sigma^2-\lvert\mathbf{x}\rvert^2}{(\lvert x\rvert^2+\sigma^2)^4}$
	Gaussian	$\frac{1}{2\pi\sigma^2}\exp\left(-\frac{\lvert\mathbf{x}\rvert^2}{2\sigma^2}\right)$
	Super Gaussian	$\frac{1}{2\pi\sigma^2}\left(2-\frac{\lvert\mathbf{x}\rvert^2}{2\sigma^2}\right)\exp\left(-\frac{\lvert\mathbf{x}\rvert^2}{2\sigma^2}\right)$
$3-D$	*Low order algebraic*	$\frac{3}{4\pi}\frac{\sigma^2}{(\lvert\mathbf{x}\rvert^2+\sigma^2)^{5/2}}$
	High order algebraic	$\frac{15}{8\pi}\frac{\sigma^4}{(\lvert\mathbf{x}\rvert^2+\sigma^2)^{7/2}}$
	Gaussian	$\frac{1}{2\pi\sigma^{3/2}}\exp\left(-\frac{\lvert\mathbf{x}\rvert^2}{2\sigma^2}\right)$
	Super Gaussian	$\frac{1}{2\pi\sigma^{3/2}}\left(\frac{5}{2}-\frac{\lvert\mathbf{x}\rvert^2}{2\sigma^2}\right)\exp\left(-\frac{\lvert\mathbf{x}\rvert^2}{2\sigma^2}\right)$

The functions can be expressed in radial symmetric form by defining

$$\zeta(\rho) = 2^{d-1}\pi\sigma^d\zeta_\sigma(|\mathbf{x}|)$$

where $\rho = |\mathbf{x}|/\sigma$, and d is the dimension. In this case the moment properties can be written as

$$\begin{cases} \int \zeta(\rho)\rho^{d-1}d\rho = 1 \\ \int \zeta(\rho)\rho^{d-1}\rho^s d\rho = 0 & 2 \le s \le r-1 \\ \int |\zeta(\rho)|\rho^{d-1}\rho^r d\rho < \infty, \end{cases}$$

and the list of smoothing functions is simplified to

$2-D$	*Low order algebraic*	$\dfrac{2}{(\rho^2+1)^2}$
	High order algebraic	$\dfrac{4}{(\rho^2+1)^3}$
	Super algebraic	$4\dfrac{(2-\rho^2)}{(\rho^2+1)^4}$
	Gaussian	$\exp\left(-\dfrac{\rho^2}{2}\right)$
	SuperGaussian	$\left(2-\dfrac{\rho^2}{2}\right)\exp\left(-\dfrac{\rho^2}{2}\right)$
$3-D$	*Low order algebraic*	$\dfrac{3}{(\rho^2+1)^{5/2}}$
	High order algebraic	$\dfrac{15}{2(\rho^2+1)^{7/2}}$
	Gaussian	$\left(\dfrac{2}{\pi}\right)^{1/2}\exp\left(-\dfrac{\rho^2}{2}\right)$
	Super Gaussian	$\left(\dfrac{2}{\pi}\right)^{1/2}\left(\dfrac{5}{2}-\dfrac{\rho^2}{2}\right)\exp\left(-\dfrac{\rho^2}{2}\right)$

The following relations hold between the radial symmetric regularization functions $\zeta(\rho)$, $g(\rho)$, and $G(\rho)$.

$$\begin{aligned}
\zeta(\rho) = \quad & \frac{1}{\rho^{d-1}}\frac{d}{d\rho}g(\rho) = \quad -\frac{1}{\rho^{d-1}}\frac{d}{d\rho}\left(\rho^{d-1}\frac{d}{d\rho}G(\rho)\right) \\
\int_0^\rho \zeta(s)s^{d-1}ds = \quad & g(\rho) = \quad -\rho^{d-1}\frac{d}{d\rho}G(\rho) \\
-\int_0^\rho\int_0^t \zeta(s)s^{d-1}t^{1-d}dsdt = \quad & -\int_0^\rho g(s)s^{1-d}ds = \quad G(\rho)
\end{aligned}$$

Also, the relation between the radial symmetric and non-radial symmetric functions can be summarized as follows.

$$\begin{aligned}
\zeta_\sigma(\mathbf{x}) &= \frac{1}{2^{d-1}\pi\sigma^d}\zeta(\rho) \\
g_\sigma(\mathbf{x}) &= g(\rho) \\
G_\sigma(\mathbf{x}) &= \frac{1}{\sigma^{d-2}}G(\rho).
\end{aligned}$$

A similar analysis can be performed for the PSE kernel. The radial symmetric PSE kernel is defined as

$$\eta(\rho) = 2^{d-1}\pi\sigma^d\eta_\sigma(\mathbf{x}).$$

The moment properties of the PSE kernel are

$$\begin{cases} \int \eta(\rho)\rho^4 d\rho = 3 \\ \int \eta(\rho)\rho^4\rho^s d\rho = 0 & 2 \le s \le r-1 \\ \int |\eta(\rho)|\rho^4\rho^r d\rho < \infty, \end{cases}$$

The relation between the radial symmetric PSE kernel and radial symmetric cutoff function is

$$\eta(\rho) = -\frac{1}{\rho}\frac{d\zeta}{d\rho}.$$

Thus, the three dimensional high order algebraic PSE kernel is

$$\eta(\rho) = \frac{105}{2(\rho^2+1)^{9/2}}.$$

This can be rewritten in non-radial-symmetric form as

$$\eta_\sigma(\mathbf{x}) = \frac{105}{8\pi}\frac{\sigma^6}{(|\mathbf{x}|^2+\sigma^2)^{9/2}}.$$

The moment properties of non-radial-symmetric PSE kernels are

$$\begin{cases} \int x_i x_j \eta_\sigma(\mathbf{x}) d\mathbf{x} = \delta_{ij} \\ \int x_i^{i_1} x_j^{i_2} \eta_\sigma(\mathbf{x}) d\mathbf{x} = 0 & i_1 + i_2 = 1 \quad or \quad 3 \le i_1 + i_2 \le r+1 \\ \int |\mathbf{x}|^{r+2} \eta_\sigma(\mathbf{x}) d\mathbf{x} < \infty, \end{cases}$$

The relation between the non-radial-symmetric PSE kernel and non-radial-symmetric cutoff function is

$$\eta_\sigma(\mathbf{x}) = -\frac{\nabla\zeta_\sigma(\mathbf{x})\cdot\mathbf{x}}{|\mathbf{x}|^2/\sigma^2}.$$

B.2 Alternative Form of the Stretching Term

B.2.1 Stretching Term in Perturbation Form

The assumption here is that the mean velocity is unidirectional in the downstream direction x_1 and has a constant shear-rate S in the vertical direction x_3.

$$U_i = S x_3 \delta_{i1}. \tag{B.1}$$

The equations become confusing in vector notation so index notation is used here. The vectors asociated with the target points are denoted with the superscript p, and the source

points with q, in order to avoid confsion between the two. Using these conventions the vector Biot-Savart equation

$$\mathbf{u} = \int \boldsymbol{\omega} \times \nabla G, \tag{B.2}$$

can be written as

$$u_i^p = \int \epsilon_{ijk} \omega_j^q \frac{\partial}{\partial x_k} G. \tag{B.3}$$

The Green's function quadrupole is derrived by

$$\begin{aligned}
\frac{\partial}{\partial x_l}\frac{\partial}{\partial x_k} G &= \frac{\partial}{\partial x_l}\left(\frac{\partial r}{\partial x_k}\frac{\partial G}{\partial r}\right) \\
&= -\frac{\partial}{\partial x_l}\left(x_k \frac{1}{4\pi r^3}\right) \\
&= -\frac{\partial x_k}{\partial x_l}\frac{1}{4\pi r^3} - x_k \frac{\partial r}{\partial x_l}\frac{\partial}{\partial r}\left(\frac{1}{4\pi r^3}\right) \\
&= -\frac{\delta_{kl}}{4\pi r^3} - x_k \frac{x_l}{r}\frac{-3}{4\pi r^4} \\
&= -\frac{\delta_{kl}}{4\pi r^3} + 3 x_k x_l \frac{1}{4\pi r^5},
\end{aligned} \tag{B.4}$$

where the following relations have been used.

$$\begin{aligned}
\frac{\partial r}{\partial x_i} &= \frac{x_i}{r} \\
\frac{\partial G}{\partial r} &= -\frac{1}{4\pi r^2} \\
\frac{\partial x_i}{\partial x_j} &= \delta_{ij}.
\end{aligned}$$

Using Eq. (B.3) and Eq. (B.4) the stretching term can be discretized as

$$\begin{aligned}
\frac{D\omega_i^p}{Dt} &= \omega_l^p \frac{\partial^p}{\partial x_l} u_i^p \\
&= \omega_l^p \frac{\partial^p}{\partial x_l} \int \epsilon_{ijk} \omega_j^q \frac{\partial^q}{\partial x_k} G \\
&= \int \epsilon_{ijk} \omega_l^p \omega_j^q \frac{\partial^p}{\partial x_l}\frac{\partial^q}{\partial x_k} G \\
&= \int \frac{\epsilon_{ijk}\omega_j^p \omega_k^q}{4\pi r^3} + \frac{3\epsilon_{ijk}\omega_j^q x_k^q \omega_l^p x_l^p}{4\pi r^5}.
\end{aligned} \tag{B.5}$$

The transposed version of the above equation is

$$\begin{aligned}
\frac{D\omega_i^p}{Dt} &= \omega_l^p \frac{\partial^p}{\partial x_i} u_l^p \\
&= \int \frac{\epsilon_{ijk}\omega_j^p \omega_k^q}{4\pi r^3} + \frac{3\epsilon_{jkl}\omega_j^q x_k^q \omega_l^p x_i^p}{4\pi r^5}.
\end{aligned} \tag{B.6}$$

Also, by considering a mean shear $U_i = Sx_3\delta_{i1}$, the stretching term becomes

$$\begin{aligned}\frac{D\omega_i^p}{Dt} &= \omega_l^p \frac{\partial^p}{\partial x_l} u_i^p + \omega_3^p S\delta_{i1} + S\frac{\partial^p u_i^p}{\partial x_2} \\ &= \int \frac{\epsilon_{ijk}\omega_j^p\omega_k^q}{4\pi r^3} + \frac{3\epsilon_{ijk}\omega_j^q x_k^q \omega_l^p x_l^p}{4\pi r^5} \\ &+ S\int -\frac{\epsilon_{ij2}\omega_j^q}{4\pi r^3} + \frac{3\epsilon_{ijk}\omega_j^q x_k^q x_2^p}{4\pi r^5} + S\omega_3^p\delta_{i1}.\end{aligned} \tag{B.7}$$

The transposed version of this equation is

$$\begin{aligned}\frac{D\omega_i^p}{Dt} &= \omega_l^p \frac{\partial^p}{\partial x_i} u_l^p + \omega_1^p S\delta_{i3} + S\frac{\partial^p u_2^p}{\partial x_i} \\ &= \int \frac{\epsilon_{ijk}\omega_j^p\omega_k^q}{4\pi r^3} + \frac{3\epsilon_{jkl}\omega_j^q x_k^q \omega_l^p x_i^p}{4\pi r^5} \\ &+ S\int -\frac{\epsilon_{2ji}\omega_j^q}{4\pi r^3} + \frac{3\epsilon_{2jk}\omega_j^q x_k^q x_i^p}{4\pi r^5} + S\omega_1^p\delta_{i3}.\end{aligned} \tag{B.8}$$

B.3 Stretching Term on the MDGRAPE

On the MDGRAPE the equation

$$(\boldsymbol{\alpha}_i \cdot \mathbf{r}_{ij})(\mathbf{r}_{ij} \times \boldsymbol{\alpha}) \tag{B.9}$$

can be calculated by either

$$\begin{array}{c}(\boldsymbol{\alpha}_i \cdot \mathbf{r}_i)(\mathbf{r}_{ij} \times \boldsymbol{\alpha}_j) - (\boldsymbol{\alpha}_i \cdot \mathbf{r}_j)(\mathbf{r}_{ij} \times \boldsymbol{\alpha}_j), \\ \downarrow \qquad\quad \downarrow \qquad \downarrow \\ 3 \qquad\quad 3 \quad \times \quad 3\end{array} \tag{B.10}$$

or

$$\begin{array}{c}(\boldsymbol{\alpha}_i \cdot \mathbf{r}_{ij})(\mathbf{r}_i \times \boldsymbol{\alpha}_j) - (\boldsymbol{\alpha}_i \cdot \mathbf{r}_{ij})(\mathbf{r}_j \times \boldsymbol{\alpha}_j). \\ \downarrow \qquad\qquad\qquad \downarrow \\ 6 \qquad\qquad\qquad 3\end{array} \tag{B.11}$$

The transposed equation

$$[\boldsymbol{\alpha}_i \cdot (\mathbf{r}_{ij} \times \boldsymbol{\alpha}_j)]\mathbf{r}_{ij}, \tag{B.12}$$

can be calculated by either

$$\begin{matrix} [\boldsymbol{\alpha}_i \cdot (\mathbf{r}_i \times \boldsymbol{\alpha}_j)]\mathbf{r}_{ij} - [\boldsymbol{\alpha}_i \cdot (\mathbf{r}_j \times \boldsymbol{\alpha}_j)]\mathbf{r}_{ij}, \\ \downarrow \qquad\qquad\qquad \downarrow \\ 6 \qquad\qquad\qquad 3 \end{matrix} \tag{B.13}$$

or

$$\begin{matrix} [\boldsymbol{\alpha}_i \cdot (\mathbf{r}_{ij} \times \boldsymbol{\alpha}_j)]\mathbf{r}_i - [\boldsymbol{\alpha}_i \cdot (\mathbf{r}_{ij} \times \boldsymbol{\alpha}_j)]\mathbf{r}_j. \\ \downarrow \ \downarrow \qquad\qquad\qquad \downarrow \ \downarrow \\ 3 \times 3 \qquad\qquad\qquad 3 \times 3 \end{matrix} \tag{B.14}$$

Appendix C

Fast Multipole Method

Trading accuracy for speed is quite common in N-body problems, the basic idea is to find a way to systematically approximate the far field using minimum effort. Due to the dedication of numerous pursuers, remarkable algorithms have been developed in the past few decades. Among them, the most often referred to are the "tree code" by Barnes and Hut[22], and the "Fast Multipole Method (FMM)" by Greengard and Rokhlin[23]. The tree code has a theoretical calculation cost of $O(N \log N)$, whereas the FMM has a cost of $O(N)$. This does not mean the FMM is invariably faster than the tree code, but there is a break even point where the $N \log N$ slope crosses the N. The location of this break even point depends strongly on the details of the algorithm, and also how efficiently the program is written, and sometimes even the compiler or hardware being used. One should carefully consider the accuracy required, and choose the order of multipole moments needed to obtain this accuracy, and depending on the number of moments, faster translation methods using Rotation, FFT, Matrix Decomposition may need to be taken into consideration.

In this section, the details of the algorithm, and how to efficiently program it are mentioned, along with the additional ideas needed for implementing the FMM in vortex methods. Furthermore, a technique that allows the FMM to be used on the MDGRAPE-3 (a special purpose board for calculating N-body calculations at a peak speed of 330 GFlops/board) is proposed.

C.1 Box Structure

Both the tree code and FMM construct box structures around the particles they wish to calculate. The bookkeeping must be done systematically and the translation of informa-

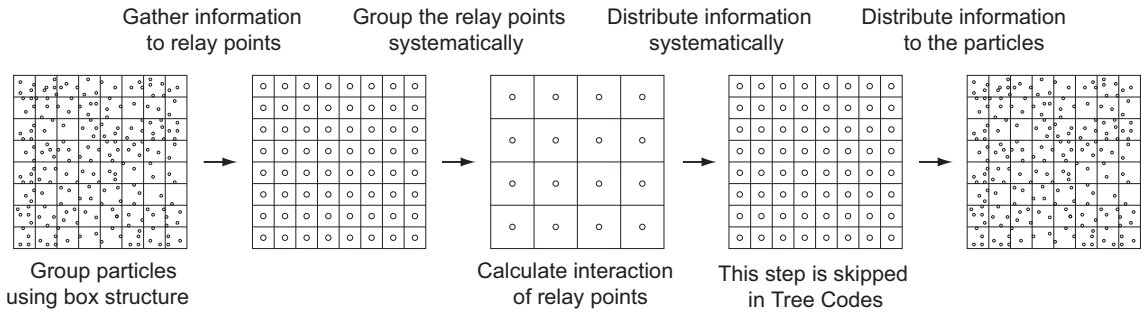

Figure C.1: Flow of calculation

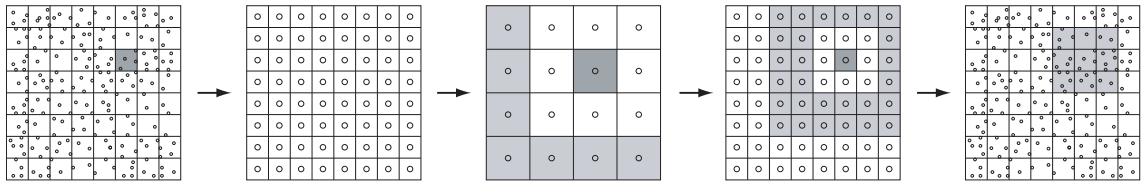

Figure C.2: Example of the calculation sequence

tion within these box structures must be done efficiently. A method to construct such box structures is introduced first. Then, it will be shown how the data is transferred within this structure, and how the bookkeeping is done.

A very rough schematic of the flow of calculation is shown in Fig. C.1.The tree code and FMM first form a box structure, which divides the particles into groups. The information of the particles belonging to a certain box are gathered to a relay point at the center of the box. Then this information is passed on to coarser levels, at which the interaction between well separated boxes is calculated. The tree code directly distributes the results to the well separated particles, as to where the FMM first distributes the results to finer levels, and then to the particles.

The basic idea behind these methods is that the influence of far particles do not have to be subtilized. This concept does not support the interaction between neighboring boxes, because they would be influencing particles within a distance comparable to that of what they represent. Thus, the calculation sequence becomes slightly complicated, as shown in Fig. C.2. Suppose one wishes to calculate the influence of all particles onto the particles in the dark grey box. The particle information is gathered and sequentially passed on to the coarser relay points. At the coarsest level the influence of the light grey boxes on the dark grey box is calculated. At the next level the influence of the remaining

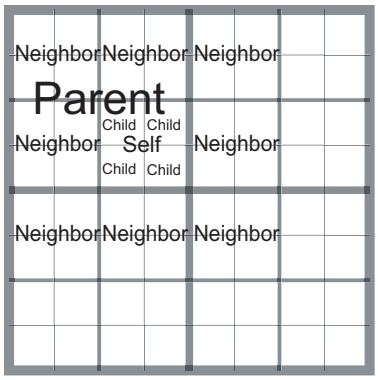

Figure C.3: Hierarchy of boxes

boxes, which are now non-neighboring are calculated. At the finest level the remaining neighbor boxes are calculated by direct particle interaction. This example is based on the FMM, but the only difference for a tree code would be the third and fourth picture, where the dark grey box would consist of particles instead of a relay point.

The data structure and bookkeeping of the tree code and FMM should be constructed to effectively handle the procedures in Fig. C.2. First, in order to pass on the information between levels, it is essential that one can readily find the corresponding relay points of the coarser and finer levels. Such boxes are defined as parents and children, as shown in Fig. C.3. The indexing shown in Fig. C.4 is ideal for this case. Suppose that d is the number of dimensions one is calculating in, and n is the global index of the box. The corresponding index of the parent box is always $n/2^d$, and the indices of the children are $2^d n + i$, where $i = 0, ..., 2^d - 1$. At the same time, it is necessary to find the position of each relay point and also acknowledge neighbor boxes. This is easier if one uses an indexing like the one in Fig. C.5. Suppose that $xmin$, $xmax$, $ymin$ and $ymax$ represent the size of the calculation domain (the level 0 box), (n_x, n_y) denotes the coordinate index, and l is the box level. The position of a relay point can be calculated by

$$\begin{aligned} x &= xmin + (xmax - xmin)2^{-l}(n_x + 2^{-1}), \\ y &= ymin + (ymax - ymin)2^{-l}(n_y + 2^{-1}), \end{aligned} \tag{C.1}$$

and the coordinate index of the neighbors are obvious. Now, one wonders if there could be a relation between these two indexing methods. The answer is yes. The global index

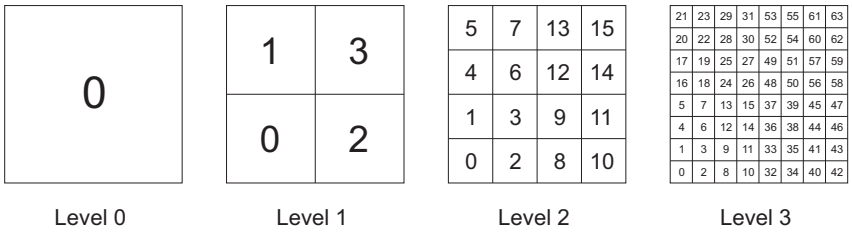

Figure C.4: Global indexing in 2-D

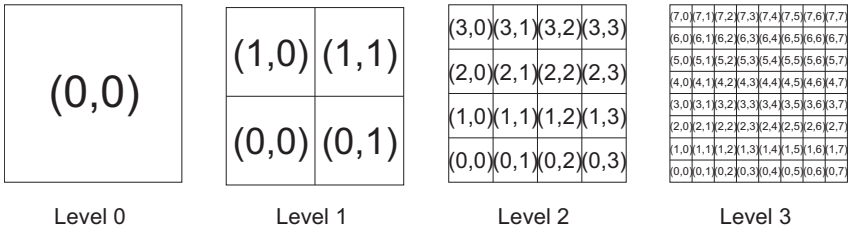

Figure C.5: Coordinate indexing in 2-D

can be obtained from coordinate indices by calculating

$$n = \sum_{i=0}^{l-1} \big[\mod (n_x/2^i, 2) 2^{(di+1)} + \mod (n_y/2^i, 2) 2^{di} \big], \tag{C.2}$$

and the vice versa by

$$\begin{aligned} n_x &= \sum_{i=0}^{l-1} \mod (n/2^{(di+1)}, 2) 2^i, \\ n_y &= \sum_{i=0}^{l-1} \mod (n/2^{di}, 2) 2^i. \end{aligned} \tag{C.3}$$

The extension to the 3-D case is straightforward, and the relations are

$$\begin{aligned} n = \sum_{i=0}^{l-1} \big[& \mod (n_x/2^i, 2) 2^{(di+1)} + \mod (n_y/2^i, 2) 2^{di} \\ + & \mod (n_z/2^i, 2) 2^{(di+2)} \big], \end{aligned} \tag{C.4}$$

Figure C.6: Basic concept of the multipole expansion in 1-D

$$\begin{aligned} n_x &= \sum_{i=0}^{l-1} \mod (n/2^{(di+1)}, 2)2^i, \\ n_y &= \sum_{i=0}^{l-1} \mod (n/2^{di}, 2)2^i, \\ n_z &= \sum_{i=0}^{l-1} \mod (n/2^{(di+2)}, 2)2^i. \end{aligned} \tag{C.5}$$

The beauty of this indexing method lies in its ability to find the corresponding group of particles or relay points with minimum complexity and memory requirements.

C.2 Formulation

The formulation and basic ideas underlying are the same for both the tree code and FMM. Here, the formulation of only the FMM is explained, since everything the tree code needs is also used in the FMM. First, a very simple 1-D example is presented, which illustrates the general concept of these methods. Then, by using complex variables this concept is extended to a 2-D case. After that, the concept is extended to 3-D with the use of spherical harmonics. Then, a faster translation method is introduced, which makes use of the rotation of spherical harmonics. Finally, the two subspecies of FMM, which do not use multipoles are shown.

C.2.1 1-D case

Let us first consider a case where x_i and x_j represent two separate points in a 1 dimensional space. By introducing a third point x_* somewhere near x_j, the function takes the form

$$\frac{1}{x_i - x_j}. \tag{C.6}$$

Using the third point x_*, this can be rewritten

$$\frac{1}{x_i - x_j} = \frac{1}{x_i - x_*} \frac{1}{\left(1 - \frac{x_j - x_*}{x_i - x_*}\right)}. \tag{C.7}$$

The Mclaurin expansion of $\frac{1}{1-t}$ has the form of

$$\frac{1}{1-t} = \sum_{k=0}^{\infty} t^k, \tag{C.8}$$

by substituting $\frac{x_j - x_*}{x_i - x_*}$ into t, Eq. (C.7) becomes

$$\frac{1}{x_i - x_j} = \frac{1}{x_i - x_*} \sum_{k=0}^{\infty} \left(\frac{x_j - x_*}{x_i - x_*} \right)^k = \sum_{k=0}^{\infty} (x_i - x_*)^{-(k+1)} (x_j - x_*)^k. \tag{C.9}$$

Now if one considers the calculation between N particles, where

$$\Phi(x_i) = \sum_{j=1}^{N} \frac{1}{x_i - x_j}, \tag{C.10}$$

is preformed for each target particle i, It can be seen that a straight forward calculation would have the cost of $O(N^2)$. By considering the relation in Eq. (C.9), this equation can be rewritten as

$$\Phi(x_i) = \sum_{k=0}^{\infty} \underbrace{(x_i - x_*)^{-(k+1)}}_{(a)} \sum_{j=1}^{N} \underbrace{(x_j - x_*)^k}_{(b)}. \tag{C.11}$$

Part (a) does not involve j particles so it can be taken outside of the summation for j. In the same way, part (b) does not involve i particles so this part need not be computed for every i particle. So the moments of the j particles around $*$ are calculated to obtain

$$M_k = \sum_{j=1}^{N} (x_j - x_*)^k. \tag{C.12}$$

By truncating the Mclaurin expansion at a finite order p, k needs to be calculated only from 0 to $p-1$. So the calculation cost of this part is $O(pN)$. Then this M_k can be used to calculate

$$\Phi(x_i) = \sum_{k=0}^{p-1} (x_i - x_*)^{-(k+1)} M_k. \tag{C.13}$$

This equation must be calculated for N particles, so the calculation cost of this equation is also $O(pN)$. The resulting total cost is $O(pN)$, so if p is some where around 10 and N is about 10^6 the calculation cost can be reduced 10^5 times. Of course this is a special case, where a single point $*$ could be used as a relay point for all j particles. This is impossible because the Mclaurin expansion assumes that

$$\frac{|x_j - x_*|}{|x_i - x_*|} \ll 1, \tag{C.14}$$

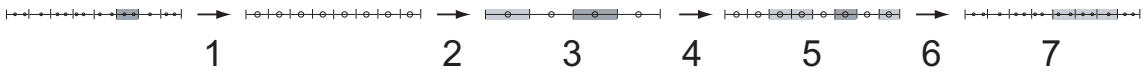

Figure C.7: Details of the calculation sequence in 1-D

and it is obvious that no single point $*$ can be close to all particles simultaneously. In the actual case, more than one relay point is used, as shown in the previous chapter. These relay points are actually called the origin of the multipole expansion, meaning that the multipole moments are calculated by using these points as the origin. One can always define either of the following two equations for any set of i and j particles, except the for the case where i and j are extremely close to each other.

$$\Phi(x_i) = \sum_{k=0}^{p-1}(x_i - x_*)^{-(k+1)} \underbrace{\sum_{j=1}^{N}(x_j - x_*)^k}_{M_k}, \qquad |x_j - x_*| \ll |x_i - x_*|\,, \tag{C.15}$$

$$\Phi(x_i) = \sum_{k=0}^{p-1}(x_i - x_*)^{k} \underbrace{\sum_{j=1}^{N}(x_j - x_*)^{-(k+1)}}_{L_k}, \qquad |x_j - x_*| \gg |x_i - x_*|\,. \tag{C.16}$$

Eq. (C.15) is called the multipole expansion, whereas Eq. (C.16) is called the local expansion. "Multipole" is sometimes replaced by the words "Singular", "Outer" or "Far Field", and "Local" is sometimes called "Regular", "Inner" or "Near Field", but they all mean the same thing.

In the previous section, an example of the calculation sequence was shown in Fig. C.2. A 1-D version of this is shown in Fig. C.7, and this time the actual equations being solved are shown. Each number in the figure represents a certain calculation. Step 1. is the multipole expansion, where the M_k at the center of each box is calculated from Eq. (C.12), where j and N are the indices and total number of particles in the corresponding box. As mentioned earlier, Eq. (C.15) is also called the multipole expansion, but the entire equation Eq. (C.15) is never calculated in the actual sequence, only the M_k part is. Thus, the multipole expansion in the actual calculation refers to Eq. (C.12). Step 2. is the multipole to multipole translation, where the M_k of the finer boxes are gathered to form the M_k of the coarser boxes by calculating

$$M_n = \sum_{k=0}^{n} \hat{M}_k (-1)^{n-k} \binom{n}{k} (x_* - \hat{x}_*)^{n-k}, \tag{C.17}$$

where n and k are the indices of the coarse and fine boxes respectively. The *hat* represents the M of the finer boxes, whereas the unmarked M represents the multipole expansion of the coarser boxes. Step 3. is the multipole to local translation, which is preformed at the coarsest level. The L_k induced by the M_k of well separated boxes is calculated by

$$L_n = \sum_{k=0}^{p-1} M_k (-1)^n \binom{n+k}{n} (x_* - \hat{x}_*)^{-(n+k+1)}, \tag{C.18}$$

where the notations follow Eq. (C.17), and p is the order of multipole expansion. Step 4. is the local to local translation, where the L_k of the coarser boxes is distributed to the L_k of the finer ones by calculating

$$L_n = \sum_{k=n}^{p-1} \hat{L}_k \binom{k}{n} (x_* - \hat{x}_*)^{k-n}. \tag{C.19}$$

Here, the *hat* represents the L at coarser boxes, and the unmarked L represents the local expansion of the finer boxes. Step 5. is the multipole to local translation for the remaining boxes at finer levels. When the neighbor boxes are divided into finer boxes, some of them become non-neighbors again, so one must calculate Eq. (C.18) for these remaining boxes. Step 6. is the local expansion, where the L_k is distributed to the particles contained in the corresponding boxes. By the time this calculation takes place, the influence from all particles except the ones in the neighbor and self boxes have been integrated into L_k, so solving Eq. (C.16) for each i particle using the corresponding L_k will account for the effect of these particles. Step 7. is the direct calculation, which calculated Eq. (C.10) for all particles belonging to the neighboring and self boxes at the finest level. By the end of this step, the contribution of all source particles would have been considered.

C.2.2 2-D case

The above mentioned concept can be extended from 1-D to 2-D by making use of complex variables. For the 2-D case the formulations basically follow that of Hrycak & Rokhlin [72], but for the sake of consistency with the 1-D and 3-D case, M_k and L_k will be used instead of a_k and b_k for the expansions, and also z_i and z_j instead of z and z_i. The z in Hrycak & Rokhlin corresponds to both $z_i - z_j$ and $z_i - z_*$ for our case, and z_i used in Hrycak & Rokhlin corresponds to $z_j - z_*$ in our notations. Using such variables, the complex potential function of interest has the form

$$\Phi(z_i) = \sum_{j=1}^{N} \frac{q_j}{z_i - z_j}, \tag{C.20}$$

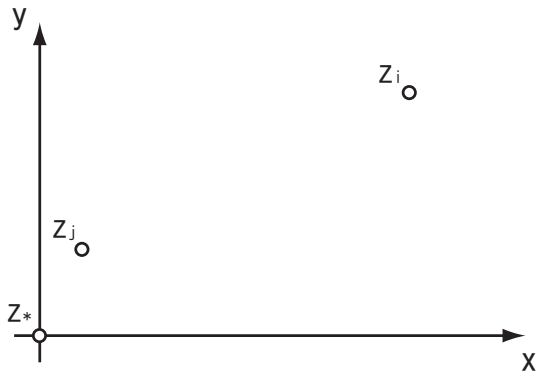

Figure C.8: Basic concept of the multipole expansion in 2-D

where $z = x + iy$ is the complex coordinate and q is the source strength. In likewise manner to the 1-D case the 2-D multipole expansion and local expansion become

$$\Phi(z_i) = \sum_{k=0}^{p-1} (z_i - z_*)^{-(k+1)} \underbrace{\sum_{j=1}^{N} (z_j - z_*)^k}_{M_k}, \qquad |z_j - z_*| \ll |z_i - z_*|, \tag{C.21}$$

$$\Phi(z_i) = \sum_{k=0}^{p-1} (z_i - z_*)^k \underbrace{\sum_{j=1}^{N} (z_j - z_*)^{-(k+1)}}_{L_k}, \qquad |z_j - z_*| \gg |z_i - z_*|. \tag{C.22}$$

The only difference between the 1-D case is that the x has now become z. The translation equations directly follow from the 1-D case to yield

$$M_n = \sum_{k=0}^{p-1} \hat{M}_k (-1)^{n-k} \binom{n}{k} (z_* - \hat{z}_*)^{n-k}, \tag{C.23}$$

$$L_n = \sum_{k=0}^{p-1} M_k (-1)^n \binom{n+k}{n} (z_* - \hat{z}_*)^{-(n+k+1)}, \tag{C.24}$$

$$L_n = \sum_{k=n}^{p-1} \hat{L}_k \binom{k}{n} (z_* - \hat{z}_*)^{k-n}. \tag{C.25}$$

The notations directly follow the 1-D case. The calculation sequence is also identical to the 1-D case. Fig. C.2 is reploted with the sequence numbering in Fig. C.9, and denote the corresponding equations below.

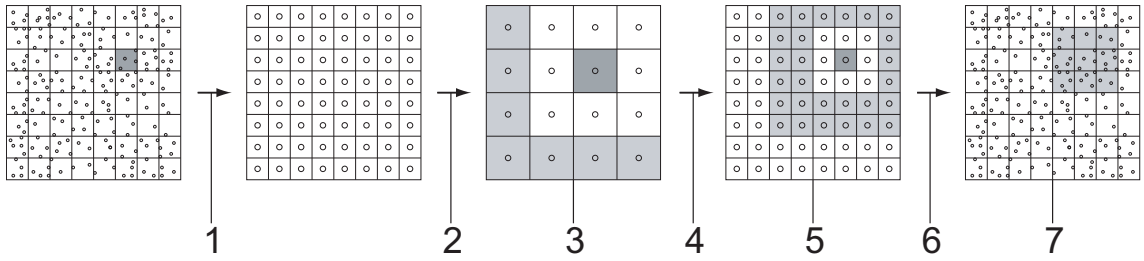

Figure C.9: Details of the calculation sequence in 2-D

Step 1. multipole expansion: Eq. (C.21)
Step 2. multipole to multipole translation: Eq. (C.23)
Step 3. multipole to local translation at coarsest level: Eq. (C.24)
Step 4. local to local translation: Eq. (C.25)
Step 5. multipole to local translation at remaining boxes: Eq. (C.24)
Step 6. local expansion: Eq. (C.22)
Step 7. direct calculation: Eq. (C.20)

C.2.3 3-D case

It is convenient to use spherical coordinates when discussing multipole expansions in 3-D. As seen in Fig. C.10, the origin of the multipole expansion is positioned at the origin of the coordinate frame. Then the two vectors can be defined as

$$\mathbf{x}_i - \mathbf{x}_* = \mathbf{x}_{i*}(r, \theta, \phi), \tag{C.26}$$

$$\mathbf{x}_j - \mathbf{x}_* = \mathbf{x}_{j*}(\rho, \alpha, \beta). \tag{C.27}$$

The vector from the origin $*$ to particle i has a radius of r, a polar angle of θ, and an azimuthal angle ϕ. The vector from the origin $*$ to particle j has a radius of ρ, a polar angle of α, and an azimuthal angle β. Separate variables are used for the i and j particles, since the equations become rather complex for the 3-D case. The conventions used here follow that of Cheng *et al.*[73]. Also, the angle between the two vectors is defined as γ. Using these notations the 3-D potential equation can be written as

$$\Phi(\mathbf{x}_i) = \sum_{j=1}^{N} \frac{\mathbf{q}_j}{|\mathbf{x}_i - \mathbf{x}_j|}. \tag{C.28}$$

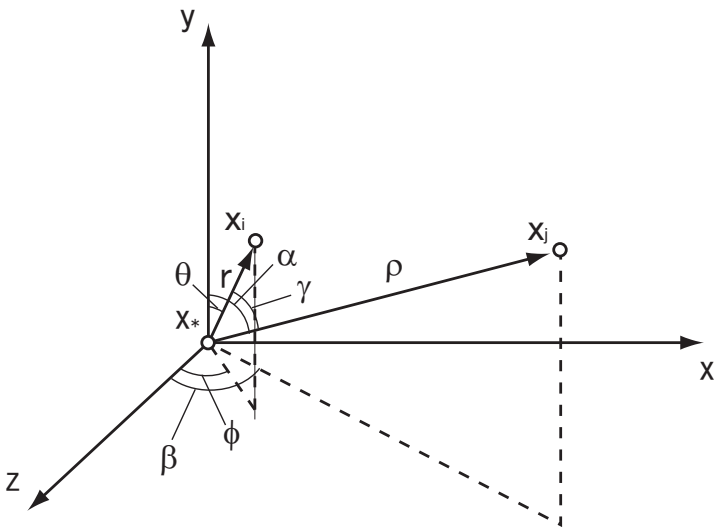

Figure C.10: Basic concept of the multipole expansion in 3-D

A part of this equation can also be rewritten in the form

$$\frac{1}{|\mathbf{x}_i - \mathbf{x}_j|} = \frac{1}{r\sqrt{1 - 2u\mu + \mu^2}}, \tag{C.29}$$

where

$$\mu = \frac{\rho}{r},$$
$$u = \cos(\gamma).$$

Similar to the 1-D and 2-D cases, a series expansion is performed, but this time a specialized expansion for spherical coordinates using Legendre polynomials is used. The Legendre polynomials are solutions to the Legendre's differential equation and may be expressed using Rodrigues' formula

$$P_n(x) = \frac{1}{2^n n!}\frac{d^n}{dx^n}(x^2 - 1)^n. \tag{C.30}$$

What is important here is the property of this function

$$\sum_{n=0}^{\infty} \mu^n P_n(u) = \frac{1}{\sqrt{1 - 2u\mu + \mu^2}}, \tag{C.31}$$

which can be substituted into Eq. (C.29) to yield

$$\frac{1}{|\mathbf{x}_i - \mathbf{x}_j|} = \sum_{n=0}^{\infty} \frac{\rho^n}{r^{n+1}} P_n(u). \tag{C.32}$$

For the 1-D and 2-D case, the equation could be separated into a part involving only i, and another part involving only j, and this was the main benefit of the multipole expansion. At this point of the 3-D analysis this can not be observed. However, when one uses the relation between Legendre polynomials and spherical harmonics

$$P_n(u) = \frac{4\pi}{2n+1} \sum_{m=-n}^{n} Y_n^{-m}(\alpha,\beta) Y_n^m(\theta,\phi), \tag{C.33}$$

it can be seen that this is possible for the 3-D case also. The spherical harmonics are the angular portion of the solution to Laplace's equation in spherical coordinates, and are most commonly defined by

$$Y_n^m(\theta,\phi) = \underbrace{(-1)^m}_{(a)} \underbrace{\sqrt{\frac{2n+1}{4\pi}}}_{(b)} \sqrt{\frac{(n-|m|)!}{(n+|m|)!}} P_n^{|m|}(cos\theta) e^{im\phi}. \tag{C.34}$$

The most confusing factor in 3-D multipole expansion is the fact that, this definition is sometimes performed without (a); the Condon-Shortley phase, or in other cases without (b); the orthonormal basis. Without the Condon-Shortley phase

$$Y_n^{-m} = \overline{Y_n^m}, \tag{C.35}$$

and with the Condon-Shortley phase

$$Y_n^{-m} = (-1)^n \overline{Y_n^m}. \tag{C.36}$$

The overline denotes the complex conjugate. This is only one example of how the definition will effect almost all relations which are derived from this definition. Following the notation of Cheng *et al.*[73], the spherical harmonic without the Condon-Shortley phase and orthonormal basis becomes

$$Y_n^m(\theta,\phi) = \sqrt{\frac{(n-|m|)!}{(n+|m|)!}} P_n^{|m|}(cos\theta) e^{im\phi}. \tag{C.37}$$

In order to calculate the spherical harmonics, the value of the associated Legendre polynomials P_n^m must be determined. The associated Legendre polynomials have a recurrence relation, which require only the information of x to start. The recurrence relations and identities used to generate the full associated Legendre polynomial are

$$(n-m)P_n^m(x) = x(2n-1)P_{n-1}^m(x) - (n+m-1)P_{n-2}^m(x), \tag{C.38}$$

$$P_m^m(x) = (-1)^m(2m-1)!(1-x^2)^{m/2}, \tag{C.39}$$

$$P_{m+1}^m = x(2m+1)P_m^m(x). \tag{C.40}$$

Once the associated Legendre polynomials are calculated, one can obtain the spherical harmonics. The usefulness of the spherical harmonics becomes clear when Eq. (C.28), Eq. (C.32), and Eq. (C.33) are combined to form

$$\Phi(\mathbf{x}_i) = \sum_{n=0}^{p-1} \sum_{m=-n}^{n} r_i^{-n-1} Y_n^m(\theta_i, \phi_i) \underbrace{\left\{ \sum_{j}^{N} \mathbf{q}_j \rho_j^n Y_n^{-m}(\alpha_j, \beta_j) \right\}}_{M_n^m} \tag{C.41}$$

$$\rho \ll r,$$

$$\Phi(\mathbf{x}_i) = \sum_{n=0}^{p-1} \sum_{m=-n}^{n} r_i^n Y_n^m(\theta_i, \phi_i) \underbrace{\left\{ \sum_{j}^{N} \mathbf{q}_j \rho_j^{-n-1} Y_n^{-m}(\alpha_j, \beta_j) \right\}}_{L_n^m} \tag{C.42}$$

$$\rho \gg r.$$

These are the mutipole and local expansions of the 3-D potential equation, respectively. Even though they may seem more complex than the 1-D and 2-D cases, the general idea of separating the part involving only i and only j is the same.

The translation operators are

$$M_j^k = \sum_{n=0}^{j} \sum_{m=-n}^{n} \frac{\hat{M}_{j-n}^{k-m} i^{|k|-|m|-|k-m|} A_n^m A_{j-n}^{k-m} \rho^n Y_n^{-m}(\alpha, \beta)}{(-1)^n A_j^k}, \tag{C.43}$$

$$L_j^k = \sum_{n=0}^{p-1} \sum_{m=-n}^{n} \frac{M_n^m i^{|k-m|-|k|-|m|} A_n^m A_j^k Y_{j+n}^{m-k}(\alpha, \beta)}{(-1)^{j+k} A_{j+n}^{m-k} \rho^{j+n+1}}, \tag{C.44}$$

$$L_j^k = \sum_{n=j}^{p-1} \sum_{m=-n}^{n} \frac{\hat{L}_n^m i^{|m|-|k|-|m-k|} A_{n-j}^{m-k} A_j^k \rho^{n-j} Y_{n-j}^{m-k}(\alpha, \beta)}{A_n^m}, \tag{C.45}$$

where

$$A_n^m = \frac{(-1)^n}{(n-m)!(n+m)!}. \tag{C.46}$$

A 3-D version of Fig. C.9 will not be presented, because the calculation sequence is identical, where the equations will be noted by just the sequence numbers below.

Step 1. multipole expansion: Eq. (C.41)
Step 2. multipole to multipole translation: Eq. (C.43)
Step 3. multipole to local translation at coarsest level: Eq. (C.44)
Step 4. local to local translation: Eq. (C.45)
Step 5. multipole to local translation at remaining boxes: Eq. (C.44)

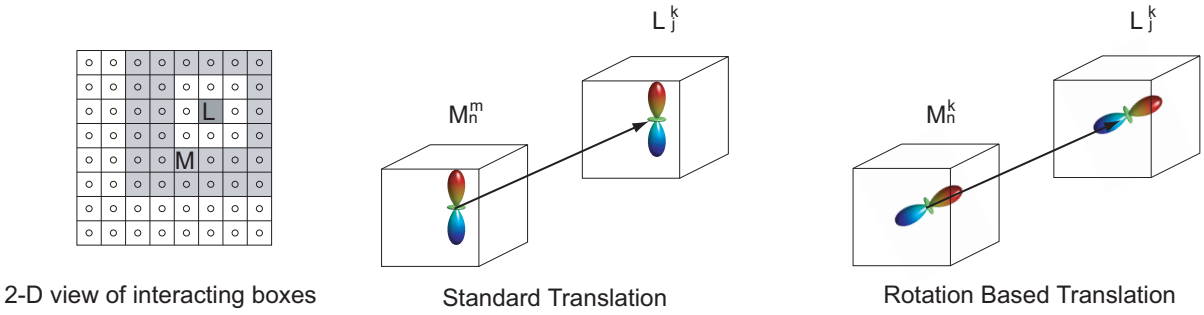

Figure C.11: Schematic of the Rotation Based Translation

Step 6. local expansion: Eq. (C.42)
Step 7. direct calculation: Eq. (C.28)

C.2.4 Rotation Based FMM

The translation operators Eq. (C.43), Eq. (C.44), and Eq. (C.45) have a complexity of $O(p^4)$. For problems that require high accuracy, the order of expansion p must be increased. There are a few methods which can reduce the complexity of the translation operator. The rotation based translation [74] has a complexity of $O(p^3)$, and the plane wave based translation [73] has a complexity of $O(p^2 \log p)$. However, the asymptotic constant is smaller for the methods with higher complexity, so for calculations that do not require large p, the effectiveness of these methods is questionable. For our case, the minimum accuracy requirements suggest that the order of expansion should be at least $p = 10$. For such moderate p the plane wave based translation is slower.

The rotation based translation makes use of a certain property of the spherical harmonic. Assuming that $\theta = 0$, and $\phi = 0$ in Eq. (C.37) yields

$$Y_n^m(0,0) = \sqrt{\frac{(n-|m|)!}{(n+|m|)!}} P_n^{|m|}. \tag{C.47}$$

Following this, the translation operators Eq. (C.43), Eq. (C.44), and Eq. (C.45)

become

$$M_j^k = \sum_{n=0}^{j} \frac{\hat{M}_{j-n}^k A_n^0 A_{j-n}^k \rho^n Y_n^0(0,0)}{(-1)^n A_j^k}, \tag{C.48}$$

$$L_j^k = \sum_{n=0}^{p-1} \frac{\hat{M}_n^k A_n^k A_j^k Y_{j+n}^0(0,0)}{(-1)^{j+k} A_{j+n}^0 \rho^{j+n+1}}, \tag{C.49}$$

$$L_j^k = \sum_{n=j}^{p-1} \frac{\hat{L}_n^k A_{n-j}^0 A_j^k \rho^{n-j} Y_{n-j}^0(0,0)}{A_n^k}. \tag{C.50}$$

It can readily be seen that the complexity of the translation has been reduced to $O(p^3)$. In order to use these translation operators, θ and ϕ must be reduced to zero. A spherical harmonic can be rotated by using the Wigner D matrix

$$Y_n^m(\alpha+\theta, \beta+\phi) = \sum_{k=-n}^{n} D_n^{km}(\theta,\phi) Y_n^k(\alpha,\beta). \tag{C.51}$$

From the definition of M and L in Eq. (C.41) and Eq. (C.42), it can be seen that M and L are the spherical harmonic Y multiplied by values which are independent of the angle. Thus, the rotation of M and L directly follow that of Y.

$$M_n^m(\alpha+\theta, \beta+\phi) = \sum_{k=-n}^{n} D_n^{km}(\theta,\phi) M_n^k(\alpha,\beta), \tag{C.52}$$

$$L_n^m(\alpha+\theta, \beta+\phi) = \sum_{k=-n}^{n} D_n^{km}(\theta,\phi) L_n^k(\alpha,\beta). \tag{C.53}$$

A schematic of the rotation based translation is shown in Fig. C.11. The two boxes in the center and right figure represent a pair of interacting boxes for the multipole to local translation, and the corresponding 2-D view is shown in the left figure. Also, in the center and right figures, an isosurface of Y_2^0 is drawn inside the boxes to represent the axis of M and L. In the standard translation the axis of the spherical harmonics and the translational vector (depicted by an arrow) are not aligned. In the rotational based translation, the multipole expansion M_n^m is first rotated by Eq. (C.52) to align with the translational vector. Then Eq. (C.49) is solved to obtain the local expansion L_j^k, and Eq. (C.53) is used to rotate L_j^k back to the original coordinate frame.

The Wigner D matrix can be decomposed into

$$D_n^{km}(\theta,\phi) = d_n^{km}(\theta) e^{\iota(k+m)\phi}. \tag{C.54}$$

There exist a variety of recurrence relations for d_n^{km}. It is true that some of these recurrence relations [75] accumulate too much round off error for calculations with large expansion order. The recurrence relations by White & Head-Gordon [74] seems to work for large expansion order $p > 10$, and is sufficient for our case. The starting point and recurrence relations can be written as

$$d_n^{n,n} = \cos\left(\frac{\theta}{2}\right)^{2n}, \tag{C.55}$$

$$d_n^{n,k-1} = \sqrt{\frac{n+k}{n-k+1}}\tan\left(\frac{\theta}{2}\right) d_n^{n,k}, \tag{C.56}$$

$$\begin{aligned} d_n^{m-1,k} = &\sqrt{\frac{n(n+1)-k(k+1)}{n(n+1)-m(m-1)}} d_n^{m,k+1}, \\ &- \frac{k+m}{\sqrt{n(n+1)-m(m-1)}} \frac{\sin\theta}{1+\cos\theta} d_n^{m,k}. \end{aligned} \tag{C.57}$$

C.2.5 FMM on MDGRAPE-3

The MDGRAPE-3 is the third model of a special purpose computer designed for molecular dynamics calculations. One MDGRAPE-3 chip has the peak performance of 330 GFlops. The vortex method has been used on the second model MDGRAPE-2 by Sheel *et al.*[76] for calculating the collision of vortex rings. The present study focuses on the simultaneous use of the FMM and MDGRAPE-3. One major problem in this sense is that the MDGRAPE chips can only handle two types of calculations. The Coulomb potential

$$p_i = \sum_{j=1}^{N} b_j g(a|\mathbf{r}_{ij}|^2), \tag{C.58}$$

and Coulomb force

$$f_i = \sum_{j=1}^{N} b_j g(a|\mathbf{r}_{ij}|^2)\mathbf{r}_{ij}. \tag{C.59}$$

$g()$ is an arbitrary function, which must be defined prior to the calculation. a and b_j are constants, which can be used for scaling. The direct form of the Biot-Savart equation Eq. (C.69) and the stretching term Eq. (C.70) can be calculated by using a combination of Eq. (C.58) and Eq. (C.59) [76], but the mutipole and local expansions and their translations are impossible to reduce to such a form. Therefore, the MDGRAPE-3 can only be used for the final step of the FMM where it calculates the direct interaction of particles. This in turn will prevent the optimum level of box divisions from growing.

The inefficiency of the above method resides in the fact that only one of the two time consuming routines of the FMM is calculated on the MDGRAPE-3. It is possible to calculate both hot spots of the FMM by converting the multipole to local translation into a many body problem. This requires the use of two independent methods, the Poisson integral method by Anderson [77] and the pseudo-particle method by Makino [78]. Instead of calculating the multipole and local expansions at the center of the boxes, these methods calculate the physical properties of interest at quadrature points placed on a spherical shell surrounding the boxes. In contrast to the original FMM, which uses five different equations for the expansions and translations, these methods use only two. Makino's method for the multipole to multipole translation

$$\boldsymbol{\alpha}_i = \sum_{j=1}^{N} \boldsymbol{\alpha}_j \sum_{n=0}^{p-1} \frac{2n+1}{K} \left(\frac{\rho_j}{r_s}\right)^n P_n(\cos\gamma_{ij}), \tag{C.60}$$

and Anderson's method for the local to local translation

$$\boldsymbol{\Phi}_i = \sum_{j=1}^{N} \boldsymbol{\Phi}_j \sum_{n=0}^{p-1} \frac{2n+1}{K} \left(\frac{\rho_j}{r_s}\right)^n P_n(\cos\gamma_{ij}), \tag{C.61}$$

i represents the index after the translation and j represents the one before. K is the number of quadrature points on the sphere surrounding the box, so the index i runs from 1 to K, and r_s is the radius of this sphere. γ_{ij} is the angle between the position vector of source and target particles. Given that $\mathbf{x}_i = (r_i, \theta_i, \phi_i)$ and $\mathbf{x}_j = (\rho_j, \alpha_j, \beta_j)$, $\cos\gamma_{ij}$ can be written as

$$\cos\gamma_{ij} = \frac{\mathbf{x}_i \cdot \mathbf{x}_j}{r_i \rho_j}, \tag{C.62}$$

Everything else (particle to multipole, multipole to local, local to particle translations) is calculated by

$$\boldsymbol{\Phi}_i = \sum_{j=1}^{N} \frac{\boldsymbol{\alpha}_j}{4\pi r_{ij}}, \tag{C.63}$$

and this equation can be transformed into the form of Eq. (C.58), and can be processed on the MDGRAPE.

Next, a brief explanation is given about how this method is actually used, by considering an example analogous to the one shown in Fig. C.9. Suppose we are calculating the Biot-Savart equation. The flow of calculation is shown in Fig. C.12 and C.13.

Step.1(P2M) Eq. (C.63) is calculated for the quadrature points on a sphere that is twice the size of the circumscribing sphere. Then, the vortex strength $\boldsymbol{\alpha}$ on the

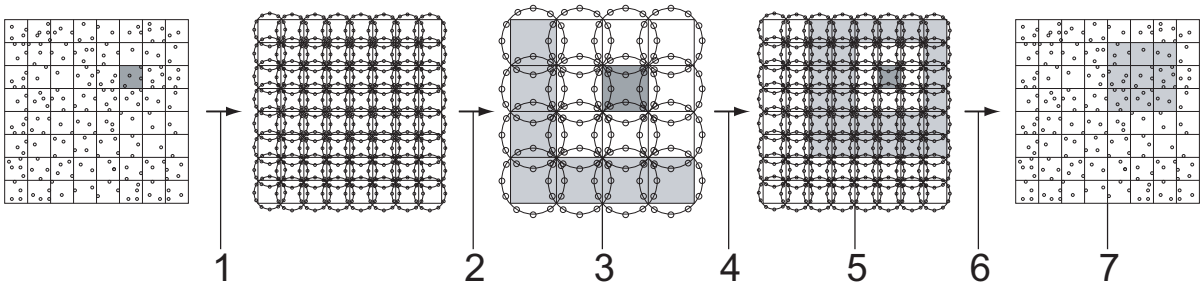

Figure C.12: Flow of FMM calculation without multipoles

circumscribing sphere is calculated from the potential $\mathbf{\Phi}$ on the large sphere by solving a system of equations in Eq. (C.63).

Step.2(M2M) Makino's method Eq. (C.60) is used to translate the vortex strength onto the larger spheres.

Step.3(M2L) Eq. (C.63) is calculated for the quadrature points on the non-neighboring spheres.

Step.4(L2L) Anderson's method Eq. (C.61) is used to translate the potential onto the smaller spheres.

Step.5(M2L) Eq. (C.63) is calculated for the quadrature points on the remaining non-neighboring spheres.

Step.6(L2P) Solve a system of equations given by Eq. (C.63) to calculate vortex strength on a sphere that is twice the size of the circumscribing sphere, from the potential on the circumscribing sphere. Then, calculate Eq. (C.69) to obtain the velocity of all particles in the corresponding box.

Step.7(P2P) Calculate the remaining induced velocity using Eq. (C.69) for all particles in the light grey box in the last figure.

A pseudo-particle tree code can be constructed by skipping steps 3, 4, and 5 and directly calculating the local expansion at each level.

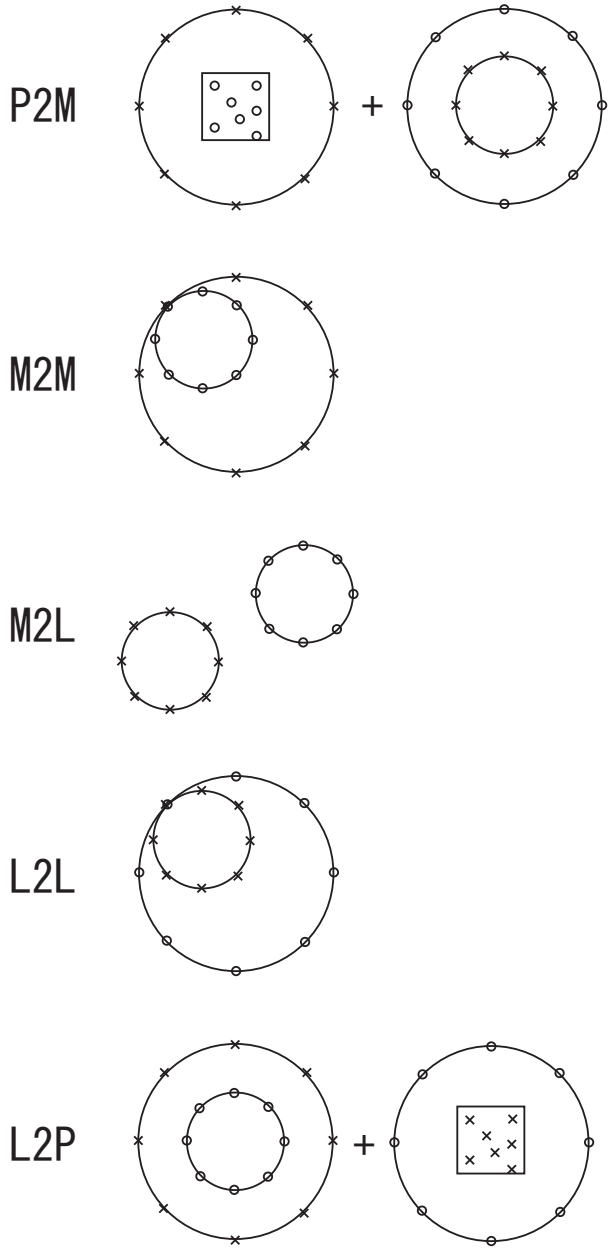

Figure C.13: A closer look of the individual steps. "x" are targets and "o" are sources

C.3 Application to Vortex Methods

C.3.1 2-D case

When using real variables, the components of the Biot-Savart law would look like

$$u_i = -\sum_{j=1}^{N} \frac{\alpha_j}{2\pi} \frac{y_i - y_j}{r_{ij}^2}, \tag{C.64}$$

$$v_i = \sum_{j=1}^{N} \frac{\alpha_j}{2\pi} \frac{x_i - x_j}{r_{ij}^2}. \tag{C.65}$$

For the 2-D case one can use complex variables to express the same thing using only

$$w_i = \sum_{j=1}^{N} \frac{i}{2\pi} \frac{\alpha_j}{z_i - z_j}, \tag{C.66}$$

where $z = x + iy$ and $w = u - iv$. For such a case, it is only necessary to apply the 1-D expansions Eq. (C.15) and Eq. (C.16), where z is used instead of x. The resulting equations are

$$w_i = \frac{i}{2\pi} \sum_{k=0}^{p-1} (z_i - z_*)^{-k-1} \left\{ \sum_{j=1}^{N} \alpha_j (z_j - z_*)^k \right\}, \tag{C.67}$$

$$= \frac{i}{2\pi} \sum_{k=0}^{p-1} (z_i - z_*)^{k} \left\{ \sum_{j=1}^{N} \alpha_j (z_j - z_*)^{-k-1} \right\}, \tag{C.68}$$

for the multipole and local expansion, respectively.

C.3.2 3-D case

In a 3-D calculation the Biot-Savart equation

$$\mathbf{u}_i = \sum_{j=1}^{N} \boldsymbol{\alpha}_j g_\sigma \times \nabla G, \tag{C.69}$$

and the stretching term

$$\begin{aligned} \frac{D\boldsymbol{\alpha}_i}{Dt} &= \boldsymbol{\alpha}_i \cdot \nabla \mathbf{u}_i \\ &= \boldsymbol{\alpha}_i \cdot \nabla \sum_{j=1}^{N} \boldsymbol{\alpha}_j g_\sigma \times \nabla G \\ &= \sum_{j=1}^{N} \boldsymbol{\alpha}_j \nabla g_\sigma \times \nabla G \cdot \boldsymbol{\alpha}_i, \end{aligned} \tag{C.70}$$

are both subject to the FMM formulation. G is the Green's function of the Laplace equation. g_σ is the cutoff function, which is defined by $g_\sigma = \int_0^\rho \zeta s^{d-1} ds$, where $\zeta\left(\frac{|\mathbf{x}|}{\sigma}\right) = 2^{d-1}\pi\sigma^d\zeta_\sigma(\mathbf{x})$, and d is the dimension. The Green's function can be approximated by the multipole expansion

$$\sum_{j=1}^{N} G \approx \frac{1}{4\pi}\sum_{n=0}^{p-1}\sum_{m=-n}^{n} \underbrace{r_i^{-n-1}Y_n^m(\theta_i,\phi_i)}_{S_i} \left\{\sum_{j=1}^{N} \underbrace{\rho_j^n Y_n^{-m}(\alpha_j,\beta_j)}_{M_j}\right\}, \tag{C.71}$$

and also the local expansion

$$\sum_{j=1}^{N} G \approx \frac{1}{4\pi}\sum_{n=0}^{p-1}\sum_{m=-n}^{n} \underbrace{r_i^{n}Y_n^m(\theta_i,\phi_i)}_{R_i} \left\{\sum_{j=1}^{N} \underbrace{\rho_j^{-n-1} Y_n^{-m}(\alpha_j,\beta_j)}_{L_j}\right\}. \tag{C.72}$$

The operators S, M, R, L are defined to simplify the equations in the following steps. Using these operators, Eq. (C.69) can be written as

$$\mathbf{u}_i \approx \frac{1}{4\pi}\sum_{n=0}^{p-1}\sum_{m=-n}^{n} \left\{\sum_{j=1}^{N} \boldsymbol{\alpha}_j M_j\right\} \times \nabla S_i, \tag{C.73}$$

$$\mathbf{u}_i \approx \frac{1}{4\pi}\sum_{n=0}^{p-1}\sum_{m=-n}^{n} \left\{\sum_{j=1}^{N} \boldsymbol{\alpha}_j L_j\right\} \times \nabla R_i. \tag{C.74}$$

Similarly, Eq. (C.70) can be written as

$$\frac{D\boldsymbol{\alpha}_i}{Dt} \approx \frac{1}{4\pi}\sum_{n=0}^{p-1}\sum_{m=-n}^{n} \left\{\sum_{j=1}^{N} \boldsymbol{\alpha}_j \times \nabla M_j\right\} (\boldsymbol{\alpha}_i \cdot \nabla S_i), \tag{C.75}$$

$$\frac{D\boldsymbol{\alpha}_i}{Dt} \approx \frac{1}{4\pi}\sum_{n=0}^{p-1}\sum_{m=-n}^{n} \left\{\sum_{j=1}^{N} \boldsymbol{\alpha}_j \times \nabla L_j\right\} (\boldsymbol{\alpha}_i \cdot \nabla R_i). \tag{C.76}$$

The cutoff function does not appear in these equations since they are used to calculate the effect of the far field, for which it would have negligible effect.

Unlike the potential equation, these equations require the calculation of gradients of the spherical harmonic. For example, in Eq. (C.74) ∇R must be calculated. Taking the derivative for each direction in spherical coordinates yields

$$\nabla R = \left(n\rho^{n-1}Y, \rho^n \frac{\partial Y}{\partial \theta}, \iota m \rho^n Y\right). \tag{C.77}$$

The calculation of these values is straightforward except for the derivative of Y_n^m, which from Eq. (C.37) becomes

$$\frac{\partial Y_n^m(\theta,\phi)}{\partial\theta} = \sqrt{\frac{(n-|m|)!}{(n+|m|)!}}\frac{\partial P_n^{|m|}(cos\theta)}{\partial\theta}e^{im\phi}. \tag{C.78}$$

The derrivative of P_n^m can be calculated from

$$\frac{\partial P_n^m}{\partial\theta} = \frac{(n-m+1)P_{n+1}^m - (n+1)\cos\theta P_n^m}{\sin\theta}. \tag{C.79}$$

Appendix D

Energy Spectrum Equation

In the calculations of homogenous isotropic turbulence and homogeneous shear flow, the critical factor is the balance between the production, spectral transfer, and dissipation of kinetic energy. The energy spectrum equation is the key equation, which has the corresponding terms for the above mentioned components. The derivation for the homogeneous isotropic case and homogeneous shear case are are shown in a comprehensive manner by combining the information given in Bernard & Wallace [79] and Hinze [80]. The notations used here basically follow that of Bernard & Wallace.

D.1 Two Point Correlation

The essentials of two point correlations are given in p.9-14, 256-261 of Bernard & Wallace. Following these conventions, the two point double and triple velocity correlation and the velocity-pressure correlation are defined as

$$\mathcal{R}_{ij}(\mathbf{x},\mathbf{y},t) \equiv \overline{u_i(\mathbf{x},t)u_j(\mathbf{y},t)}, \tag{D.1}$$

$$\mathcal{S}_{ij,k}(\mathbf{x},\mathbf{y},t) \equiv \overline{u_i(\mathbf{x},t)u_j(\mathbf{x},t)u_k(\mathbf{y},t)}, \tag{D.2}$$

$$\mathcal{K}_i(\mathbf{x},\mathbf{y},t) \equiv \overline{u_i(\mathbf{x},t)p(\mathbf{y},t)}. \tag{D.3}$$

These conventions strictly correspond to the following conventions used in Hinze

$$\mathbf{Q}_{i,j} \equiv \overline{(u_i)_A(u_j)_B},$$
$$\mathbf{S}_{ij,k} \equiv \overline{(u_i)_A(u_j)_A(u_k)_B},$$
$$\mathbf{K}_{i,p} \equiv \overline{(u_i)_A p_B},$$

but we will adopt the former by Bernard & Wallace hereafter. As shown in pages 32-33 of Bernard & Wallace, the transport equation of the two point velocity correlation can

be derrived in similar manner to the one point correlation case by taking the average of $u_i(\mathbf{x}, \mathbf{t})$ times the jth component of the Navier-Stokes equation at $\mathbf{y}$ and adding to this the same quantity with i, j and $\mathbf{x}$, $\mathbf{y}$ reversed.

$$\begin{aligned}
&\frac{\partial \mathcal{R}_{ij}}{\partial t}(\mathbf{x},\mathbf{y},t) + \overline{U}_k(\mathbf{y},t)\frac{\partial \mathcal{R}_{ij}}{\partial y_k}(\mathbf{x},\mathbf{y},t) + \overline{U}_k(\mathbf{x},t)\frac{\partial \mathcal{R}_{ij}}{\partial x_k}(\mathbf{x},\mathbf{y},t) \\
&= -\mathcal{R}_{ik}(\mathbf{x},\mathbf{y},t)\frac{\partial \overline{U}_j}{\partial y_k}(\mathbf{y},t) - \mathcal{R}_{jk}(\mathbf{y},\mathbf{x},t)\frac{\partial \overline{U}_i}{\partial x_k}(\mathbf{x},t) \\
&- \frac{\partial \mathcal{S}_{jk,i}}{\partial y_k}(\mathbf{y},\mathbf{x},t) - \frac{\partial \mathcal{S}_{ik,j}}{\partial x_k}(\mathbf{x},\mathbf{y},t) - \frac{1}{\rho}\frac{\partial \mathcal{K}_i}{\partial y_j}(\mathbf{x},\mathbf{y},t) - \frac{1}{\rho}\frac{\partial \mathcal{K}_j}{\partial x_i}(\mathbf{y},\mathbf{x},t) \\
&+ \nu\frac{\partial^2 \mathcal{R}_{ij}}{\partial y_k^2}(\mathbf{x},\mathbf{y},t) + \nu\frac{\partial^2 \mathcal{R}_{ij}}{\partial x_k^2}(\mathbf{x},\mathbf{y},t).
\end{aligned} \tag{D.4}$$

This equation is the starting point of the present analysis. Now, we assume homogeniety in all directions for the correlations, but not the mean velocity, which is true for a homogeneous shear flow. The correlation values then depend only on the relative position of $\mathbf{x}$ and $\mathbf{y}$, and not their absolute positions. The independent variables of the correlations can be changed to

$$\mathcal{R}_{ij}(\mathbf{x},\mathbf{y},t) = \mathcal{R}_{ij}(\mathbf{r},t), \tag{D.5}$$

$$\mathcal{S}_{ij,k}(\mathbf{x},\mathbf{y},t) = \mathcal{S}_{ij,k}(\mathbf{r},t), \tag{D.6}$$

$$\mathcal{K}_i(\mathbf{x},\mathbf{y},t) = \mathcal{R}_i(\mathbf{r},t), \tag{D.7}$$

where $\mathbf{r} = \mathbf{y} - \mathbf{x}$. This leads to the following relation for the derrivative.

$$\frac{\partial \mathcal{R}_{ij}}{\partial x_k}(\mathbf{x},\mathbf{y},t) = \frac{\partial \mathcal{R}_{ij}}{\partial r_k}\frac{\partial}{\partial x_k}(\mathbf{y}-\mathbf{x}) = -\frac{\partial \mathcal{R}_{ij}}{\partial r_k}(\mathbf{r},t). \tag{D.8}$$

Similarly,

$$\frac{\partial \mathcal{R}_{ij}}{\partial y_k}(\mathbf{x},\mathbf{y},t) = \frac{\partial \mathcal{R}_{ij}}{\partial r_k}(\mathbf{y}-\mathbf{x},t), \tag{D.9}$$

$$\frac{\partial \mathcal{S}_{jk,i}}{\partial y_k}(\mathbf{y},\mathbf{x},t) = -\frac{\partial \mathcal{S}_{jk,i}}{\partial r_k}(\mathbf{x}-\mathbf{y},t), \tag{D.10}$$

$$\frac{\partial \mathcal{S}_{ik,j}}{\partial x_k}(\mathbf{x},\mathbf{y},t) = -\frac{\partial \mathcal{S}_{ik,j}}{\partial r_k}(\mathbf{y}-\mathbf{x},t), \tag{D.11}$$

$$\frac{\partial \mathcal{K}_i}{\partial y_j}(\mathbf{x},\mathbf{y},t) = \frac{\partial \mathcal{K}_i}{\partial r_j}(\mathbf{y}-\mathbf{x},t), \tag{D.12}$$

$$\frac{\partial \mathcal{K}_j}{\partial x_i}(\mathbf{y},\mathbf{x},t) = \frac{\partial \mathcal{K}_j}{\partial r_i}(\mathbf{x}-\mathbf{y},t). \tag{D.13}$$

Applying these relations to Eq. (D.4) yields

$$\begin{aligned}
&\frac{\partial \mathcal{R}_{ij}}{\partial t}(\mathbf{r},t) + \overline{U}_k(\mathbf{y},t)\frac{\partial \mathcal{R}_{ij}}{\partial r_k}(\mathbf{r},t) - \overline{U}_k(\mathbf{x},t)\frac{\partial \mathcal{R}_{ij}}{\partial r_k}(\mathbf{r},t) \\
&= -\mathcal{R}_{ik}(-\mathbf{r},t)\frac{\partial \overline{U}_j}{\partial y_k}(\mathbf{y},t) - \mathcal{R}_{jk}(\mathbf{r},t)\frac{\partial \overline{U}_i}{\partial x_k}(\mathbf{x},t) \\
&+ \frac{\partial \mathcal{S}_{jk,i}}{\partial r_k}(-\mathbf{r},t) + \frac{\partial \mathcal{S}_{ik,j}}{\partial r_k}(\mathbf{r},t) - \frac{1}{\rho}\frac{\partial \mathcal{K}_i}{\partial r_j}(\mathbf{r},t) - \frac{1}{\rho}\frac{\partial \mathcal{K}_j}{\partial r_i}(-\mathbf{r},t) \\
&+ 2\nu\frac{\partial^2 \mathcal{R}_{ij}}{\partial r_k^2}(\mathbf{r},t)
\end{aligned} \tag{D.14}$$

This equation corresponds to (4-17) in Hinze, and is a generalized form of the transport equation of the two point velocity correlation for both homogeneous isotropic turbulence and homogeneous shear flows. Without loss of generality, we may assume that $\overline{U}_k = Sx_3\delta_{k1}$, where S is the shear rate of the homogeneous shear and $S = 0$ for the homogeneous isotropic turbulence. This implies that

$$\overline{U}_k(\mathbf{y},t) - \overline{U}_k(\mathbf{x},t) = \frac{\partial \overline{U}_1}{\partial x_3}r_3\delta_{k1} = Sr_3\delta_{k1}, \tag{D.15}$$

and

$$\frac{\partial \overline{U}_i}{\partial x_j} = S\delta_{i1}\delta_{j3}. \tag{D.16}$$

Substitution of these two relations to Eq. (D.14) yields

$$\begin{aligned}
&\frac{\partial \mathcal{R}_{ij}}{\partial t}(\mathbf{r},t) + Sr_3\frac{\partial \mathcal{R}_{ij}}{\partial r_1}(\mathbf{r},t) \\
&= -S\mathcal{R}_{i3}(-\mathbf{r},t)\delta_{j1} - S\mathcal{R}_{j3}(\mathbf{r},t)\delta_{i1} \\
&+ \frac{\partial \mathcal{S}_{jk,i}}{\partial r_k}(-\mathbf{r},t) + \frac{\partial \mathcal{S}_{ik,j}}{\partial r_k}(\mathbf{r},t) - \frac{1}{\rho}\frac{\partial \mathcal{K}_i}{\partial r_j}(\mathbf{r},t) - \frac{1}{\rho}\frac{\partial \mathcal{K}_j}{\partial r_i}(-\mathbf{r},t) \\
&+ 2\nu\frac{\partial^2 \mathcal{R}_{ij}}{\partial r_k^2}(\mathbf{r},t).
\end{aligned} \tag{D.17}$$

D.2 Spectral Representation

The energy spectrum equation is in wave number space so the correlation tensors must be transformed to wave number space. This is done by first defining the following correlation tensors in wave number space.

$$\mathcal{E}_{ij}(\mathbf{k},t) \equiv (2\pi)^{-3} \int_{\mathbb{R}^3} e^{\iota \mathbf{r}\cdot\mathbf{k}} \mathcal{R}_{ij}(\mathbf{r},t) d\mathbf{r}, \tag{D.18}$$

$$\mathcal{T}_{ij,k}(\mathbf{k},t) \equiv (2\pi)^{-3} \int_{\mathbb{R}^3} e^{\iota \mathbf{r}\cdot\mathbf{k}} \mathcal{S}_{ij,k}(\mathbf{r},t) d\mathbf{r}, \tag{D.19}$$

$$\mathcal{H}_{i}(\mathbf{k},t) \equiv (2\pi)^{-3} \int_{\mathbb{R}^3} e^{\iota \mathbf{r}\cdot\mathbf{k}} \mathcal{K}_{i}(\mathbf{r},t) d\mathbf{r}, \tag{D.20}$$

$\mathbf{k}$ is the wave number vector, ι is the imaginary unit $\iota = \sqrt{-1}$, $\int_{\mathbb{R}^3}$ represents the integral in three real space dimensions. From Eq. (D.18) we also obtain

$$k_1 \frac{\partial \mathcal{E}_{ij}}{\partial k_3}(\mathbf{k},t) \equiv -(2\pi)^{-3} \int_{\mathbb{R}^3} e^{\iota \mathbf{r}\cdot\mathbf{k}} r_3 \frac{\partial \mathcal{R}_{ij}}{\partial r_1}(\mathbf{r},t) d\mathbf{r}. \tag{D.21}$$

Applying the Fourier transform to Eq. (D.17) and using the above conventions yields

$$\begin{aligned} &\underbrace{\frac{\partial \mathcal{E}_{ij}}{\partial t}(\mathbf{k},t)}_{\mathcal{L}_{ij}} \underbrace{-Sk_1 \frac{\partial \mathcal{E}_{ij}}{\partial k_3}(\mathbf{k},t)}_{\mathcal{C}_{ij}} = \underbrace{-S\mathcal{E}_{i3}(\mathbf{k},t)\delta_{j1} - S\mathcal{E}_{j3}(\mathbf{k},t)\delta_{i1}}_{\mathcal{P}_{ij}} \\ &+ \underbrace{\iota k_k \mathcal{T}_{jk,i}(\mathbf{k},t) + \iota k_k \mathcal{T}_{ik,j}(\mathbf{k},t)}_{\mathcal{T}_{ij}} \underbrace{-\frac{\iota k_j}{\rho}\mathcal{H}_i(\mathbf{k},t) - \frac{\iota k_i}{\rho}\mathcal{H}_j(\mathbf{k},t)}_{\Pi_{ij}} \\ &- \underbrace{2\nu k^2 \mathcal{E}_{ij}(\mathbf{k},t)}_{\epsilon_{ij}}. \end{aligned} \tag{D.22}$$

Note that the correlations for $-\mathbf{r}$ were transformed to those for $\mathbf{r}$ by using the invariance under reflection $\mathcal{R}_{ij}(\mathbf{r},t) = \mathcal{R}_{ij}(-\mathbf{r},t)$, $\mathcal{S}_{ij,k}(\mathbf{r},t) = -\mathcal{S}_{ij,k}(-\mathbf{r},t)$, and $K_i(\mathbf{r},t) = -K_i(-\mathbf{r},t)$ before applying the Fourier transform.

The fact that the correlation tensors become a function of the wave number and time, but not space is a consequence of homogeniety. In other words, the transport equation Eq. (D.22) holds for all locations in space simultaneously, and is not a function of space.

Each term still corresponds to the terms in the Reynolds stress transport equation. $\mathcal{L}_{ij}$ is the unsteady term which represents the temporal change in the global kinetic energy.

$\mathcal{C}_{ij}$ originates from the convection term, but for this case represents the transfer of energy between wave numbers due to interaction with the mean flow through the mean shear rate.

$\mathcal{P}_{ij}$ is obviously the production term, which represents the production of energy due to the mean shear.

$\mathcal{T}_{ij}$ is the transfer term, which represents the transfer of energy between wave numbers caused by the tilting and stretching of eddies. This term reduces to the turbulent diffusion term in a one point correlation, but for the spectral equation based on two point correlations, it accounts for the interaction between the separate scales -scales which correspond to the distance of the two points of the two point correlation-.

Π_{ij} is the pressure-velocity term. This term originally corresponds to the velocity-pressure-gradient term and not the pressure-rate-of-strain term. However for the present homogenous case, the pressure diffusion term is zero since the homogenous properties do not diffuse. Thus, this term is a two point correlation version of the pressure-rate-of-strain term, which represents the influence of the pressure field in bringing an initially anisotropic turbulence back toward isotropy.

ϵ_{ij} is the dissipation term, which accounts for the dissipation of energy at small scales. This term originally corresponds to the sum of the viscous diffusion term and dissipation term, but since $\mathcal{E}_{ij}$ is homogeneous, it is diffused by neither tubulent fluctuation nor viscous effects. Hence, the viscous diffusion is zero and this term is the two point correlation version of the dissipation term.

Contracting the indices and defining $K \equiv \frac{1}{2}\mathcal{E}_{ii}$ yields

$$\underbrace{\frac{\partial K}{\partial t}(\mathbf{k},t)}_{\mathcal{L}} \underbrace{-Sk_1\frac{\partial K}{\partial k_3}(\mathbf{k},t)}_{\mathcal{C}} = \underbrace{-S\mathcal{E}_{13}(\mathbf{k},t)}_{\mathcal{P}} + \underbrace{\iota k_k \mathcal{T}_{ik,i}(\mathbf{k},t)}_{\mathcal{T}} - \underbrace{2\nu k^2 K(\mathbf{k},t)}_{\epsilon}, \tag{D.23}$$

since the redistribution term does not have normal components $\Pi_{ii} = 0$. For simplicity we will combine the mean shear effects and redifine this as the production

$$\underbrace{\frac{\partial K}{\partial t}(\mathbf{k},t)}_{\mathcal{L}} = \underbrace{Sk_1\frac{\partial K}{\partial k_3}(\mathbf{k},t) - S\mathcal{E}_{13}(\mathbf{k},t)}_{\mathcal{P}} + \underbrace{\iota k_k \mathcal{T}_{ik,i}(\mathbf{k},t)}_{\mathcal{T}} - \underbrace{2\nu k^2 K(\mathbf{k},t)}_{\epsilon}. \tag{D.24}$$

The energy spectrum equation for the homogeneous shear flow can be written as

$$\frac{\partial K}{\partial t}(\mathbf{k},t) = \mathcal{P} + \mathcal{T} - \epsilon. \tag{D.25}$$

For isotropic turbulence $S = 0$ so we obtain

$$\frac{\partial K}{\partial t}(\mathbf{k},t) = \mathcal{T} - \epsilon. \tag{D.26}$$

Bibliography

[1] Ould-Salihi, M. L. Cottet, & G.-H. Hamraoui, M. E. (2000) Blending Finite-Difference and Vortex Methods for Incompressible Flow Computations. *SIAM J. Sci. Comput.* **22**-5, 1655-1674.

[2] Rosenhead, L. (1931) The Formation of Vortices from a Surface of Discontinuity. *Proc. Roy. Soc. London. Ser. A* **134**, 170-192.

[3] Chorin, A. J. (1973) Discretization of a Vortex Sheet, with an Example of Roll-Up. *J. Comput. Phys.* **13**-3, 423-429.

[4] Kuwahara, K. & Takami, H. (1973) Numerical Studies of Two-Dimensional Vortex Motion by a System of Point Vortices. *J. Phys. Soc. Japan* **34**-1, 247-253.

[5] Hald, O. H. (1978) Convergnece of Vortex Methods for Euler's Equations. *Math. Comput.* **32**-143, 791-809.

[6] Beale, J. T. & Majda, A. (1982) Vortex Methods. I: Convergence in Three Dimensions. *Math. Comput.* **39**-159, 1-27.

[7] Hess, J. L. (1990) Panel Methods in Computational Fluid Dynamics. *Annu. Rev. Fluid Mech.* **22**, 255-274.

[8] Pozrikidis, C. (2002) *A Practical Guide to Boundary Element Methods.*, Chapman & Hall/CRC.

[9] Cottet, G.-H. & Koumoutsakos, P. D. (2000) *Vortex Methods*, Cambridge University Press.

[10] Chorin, A. J. (1973) Numerical Study of Slightly Viscous Flow. *J. Fluid Mech.* **57**, 785-796.

[11] Leonard, A. (1980) Vortex Methods for Flow Simulations. *J. Comput. Phys.* **37**, 289-335.

[12] Degond, P. & Mas-Gallic, S. (1989) The Weighted Particle Method for Convection-Diffusion Equations. Part 1: The Case of an Isotropic Viscosity. *Math. Comput.* **53**-188, 485-507.

[13] Couet, B. & Buneman, O. (1981) Simulation of Three-Dimensional Incompressible Flows with a Vortex-In-Cell Method. *J. Comput. Phys.* **39**-2, 305-328.

[14] Chorin, A. J. (1978) Vortex Sheet Approximation of Boundary Layers. *J. Comput. Phys.* **27**-3, 428-442.

[15] Fishelov, D. (1990) Vortex Methods for Slightly Viscous Three-Dimensional Flow. *SIAM J. Sci. Stat. Comput.* **11**-3, 399-424.

[16] Winckelmans, G. S. & Leonard, A. (1993) Contributions to Vortex Particle Methods for the Computation of Three-Dimensional Incompressible Unsteady Flows. *J. Comput. Phys.* **109**, 247-273.

[17] Cottet, G.-H., Koumoutsakos, P., & Ould Salihi, M. L. (2000) Vortex Methods with Spatially Varying Cores. *J. Comput. Phys.* **162**-1, 164-185.

[18] Daeninck, G., Ploumhans, P., & Winckelmans, G. S. (2002) Simulation of Three-Dimensional Bluff-Body Flows Using Vortex Methods: From Direct Numerical Simulation Towards Large-Eddy Simulation Modeling. *J. Turb.* **043**, 1-7.

[19] Koumoutsakos, P., Leonard, A., & Pepin, F. (1994) Boundary Conditions for Viscous Vortex Methods. *J. Comput. Phys.* **113**-1, 52-61.

[20] Ploumhans, P. & Winckelmans, G. S. (2000) Vortex Methods for High-Resolution Simulations of Viscous Flow Past Bluff Bodies of General Geometry. *J. Comput. Phys.* **165**-2, 354-406.

[21] Ploumhans, P., Winckelmans, G. S., Salmon, J. K., Leonard, A., & Warren, M. S. (2002) Vortex Methods for Direct Numerical Simulation of Three-Dimensional Bluff Body Flows: Application to the Sphere at Re = 300, 500, and 1000. *J. Comput. Phys.* **178**-2, 427-463.

[22] Barnes, J. & Hut, P. (1986) A Hierarchical $O(N \log N)$ Force-Calculation Algorithm. *Nature* **324**, 446-449.

[23] Greengard, L. & Rokhlin, V. (1987) A Fast Algorithm for Particle Simulations. *J. Comput. Phys.* **73**, 325-348.

[24] Sugimoto, D., Chikada, Y., Makino, J., Ito, T., Ebisuzaki, T., Umemura, M. (1990) A Special-purpose Computer for Gravitational Many-body Problems. *Nature* **345**, 33-35.

[25] Fukushige, T., Taiji, M., Makino, J., Ebisuzaki, T., & Sugimoto, D. (1996) Parallelized Special-purpose Computer for Many-body Simulations with an Arbitrary Central Force. *Astrophys. J.* **468**, 51-61.

[26] Sbalzarini, I. F., Walther, J. H., Bergdorf, M., Hieber, S. E., Kotsalis, E. M., & Koumoutsakos, P. (2006) PPM-A Highly Efficient Parallel Particle-Mesh Library for the Simulation of Continuum Systems. *J. Comput. Phys.* **215**, 566-588.

[27] Poncet, P. (2006) Finite Difference Stencils Based on Particle Strength Exchange Schemes for Improvement of Vortex Methods. *J. Turb.* **7**-23, 1-24.

[28] Rossi, L. F. (2005) Achieving High-Order Convergence Rates with Deforming Basis Functions. *SIAM J. Sci. Comput.* **26**-3, 885-906.

[29] Ploumhans, P., Daeninck, G., & Winckelmans, G. (2004) Simulation of Three-Dimensional Bluff-Body Flows Using the Vortex Particle and Boundary Element Methods. *Flow Turb. Combust.* **73**-2, 117-131.

[30] Barba, L. A., Leonard, A., & Allen, C. B. (2005) Advances in Viscous Vortex Methods- Meshless Spatial Adaption Based on Radial Basis Function Interpolation. *Int. J. Num. Meth. Fluids* **47**-5, 387-421.

[31] Eldredge, J. D., Leonard, A., & Colonius, T. (2002) A General Deterministic Treatment of Derivatives in Particle Methods *J. Comput. Phys.* **180**, 686-709.

[32] Totsuka, Y. & Obi, S. (2007) A Validation of the Viscous Dissipation Model for Fast Vortex Methods in Simulations of Decaying Turbulence. *J. Fluid Sci. Tech.* **2**, 248-257.

[33] Cottet, G. H., Michaux, B., Ossia, S., & Van der Linden, G. (2002) A Comparison of Spectral and Vortex Methods in Three-Dimensional Incompressible Flows. *J. Comput. Phys* **175**, 702-712.

[34] Rossi, L. F. (1996) Resurrecting Core Spreading Vortex Methods: A New Scheme that is Both Deterministic and Convergent. *SIAM J. Sci. Comput.* **17**-2, 370-397.

[35] Huang, M.-J. (2005) Diffusion via Splitting and Remeshing via Merging in Vortex Methods. *Int. J. Num. Meth. Fluids* **48**-2, 521-536.

[36] Chatelain, P. & Leonard, A. (2002) Face-centred cubic lattices and particle redistribution in vortex methods. *J. Turb.* **3**-046.

[37] Shankar, S. & van Dommelen, L. (1996) A New Diffusion Procedure for Vortex Methods *J. Comput. Phys.* **127**-2, 88-109.

[38] Ogami, Y. & Akamatsu T. (1991) Viscous Flow Simulation Using the Discrete Vortex Model-the Diffusion Velocity Method. *Comput. Fluids* **19**, 433-441.

[39] Grant, J. R. & Marshall, J. S. (2005) Diffusion Velocity for a Three-Dimensional Vorticity Field. *Theor. Comput. Fluid Dyn.* **19**-6, 377-390.

[40] Winckelmans, G. S. (2004) Vortex Methods. *The Encyclopedia of Fluid Mechanics* **3** John Wiley & Sons.

[41] Rogallo, R. S. (1981) Numerical experiments in homogeneous turbulence. *NASA Tech. Mem.*, 81315.

[42] Lambert, C. G., Darden, T. A., & Board, J. A. (1996) A Multipole Based Algorithm for Efficient Calculation of Forces and Potentials in Macroscopic Periodic Assemblies of Particles. *J. Comput. Phys.* **126**, 274-285.

[43] Jimenez, J., Wray, A. A., Saffman, P. G., & Rogallo, R. S. (1993) The Structure of Intense Vorticity in Isotropic Turbulence. *J. Fluid Mech.* **255**, 65-90.

[44] Pumir, A. (1994) A Numerical Study of Pressure Fluctuations in Three-Dimensional, Incompressible. Homogeneous, Isotropic Turbulence. *Phys. Fluids* **6**-6, 2071-2083.

[45] Greengard, C. (1985) The Core Spreading Method Approximates the Wrong Equation. *J. Comput. Phys.* **61**-2, 345-348.

[46] Lee, M. J., Kim, J., & Moin, P. (1990) Structure of Turbulence at High Shear Rate. *J. Fluid Mech.* **216**, 561-583.

[47] Allen, M. P. & Tildesley, D. J. (1987) *Computer Simulation of Liquids*, Oxford Science Publications.

[48] Schumann, U. (1985) Algorithms for Direct Numerical Simulation of Shear-Periodic Turbulence, in: Soubbaramayer. *Proc. 9th Int. Conf. Num. Meth. Fluid Dyn.*, Lecture Notes in Physics 218.

[49] Williamson, J. H. (1980) Low-storage Runge-Kutta Schemes. *J. Comput. Phys.* **35**, 48-56.

[50] Kim, J., Moin, P., & Moser, R. D. (1987) Turbulence Statistics in Fully Developed Channel Flow at Low Reynolds Number. *J. Fluid Mech.* **177**, 133-166.

[51] Lu, S. S. & Willmarth, W. W. (1973) Measurements of the Structure of the Reynolds Stress in a Turbulent Boundary Layer. *J. Fluid Mech.* **60**, 481-511.

[52] Pumir, A. (1996) Turbulence in Homogeneous Shear Flows *Phys. Fluids* **8**, 3112-3127.

[53] Kida, S. & Tanaka, M. (1992) Reynolds Stress and Vortical Structure in a Uniformly Sheared Turbulence *J. Phys. Soc. Japan* **61**, 4400-4417.

[54] Chatelain, P., Curioni, A., Bergdorf, M., Rossinelli, D., Andreoni, W., Koumoutsakos, P. (2008) Billion Vortex Particle Direct Numerical Simulations of Aircraft Wakes. *Comput. Methods Appl. Mech. Engrg.* **197**,1296-1304.

[55] Cocle, R., Winckelmans, G., & Daeninck, G. (2008) Combining the Vortex-In-Cell and Parallel Fast Multipole Methods for Efficient Domain Decomposition Simulations. *J. Comput. Phys.* **227**, 2263-2292.

[56] Lighthill, M. J. (1963) *Introduction. Boundary Layer Theory* Oxford University Press, 54-61.

[57] Kinney, R. B. & Paolino, M. A. (1974) Flow Transient Near the Leading Edge of a Flat Plate Moving Through a Viscous Fluid *ASME J. Appl. Mech.* **41**, 919-924.

[58] Kinney, R. B. & Cielak, Z. M. (1977) Analysis of Unsteady Viscous Flow Past an Airfoil: Part I - theoretical development *AIAA J.* **15**, 1712-1717.

[59] Wu, J. C. (1976) Numerical Boundary Conditions for Viscous Flow Problems *AIAA J.* **14**, 1042-1049.

[60] Anderson, C. (1989) Vorticity Boundary Conditions and Boundary Vorticity Generation for Two-Dimensional Viscous Incompressible Flows *J. Comput. Phys.* **80**, 72-97.

[61] Cottet, G.-H. (1988) Vorticity Boundary Conditions and the Deterministic Vortex Method for the Navier-Stokes Equation *Mathematical Aspects of Vortex Dynamics*, Society for Industrial and Applied Mathematics.

[62] Cottet, G.-H. (1991) Large Time Behavior of Deterministic Particle Approximations to the Navier-Stokes Equations *Math. Comput.* **56**, 45-59.

[63] Bernard, P. S. A Deterministic Vortex Sheet Method for Boundary Layer Flow *J. Comput. Phys.* **117**, 132-145.

[64] Marshall, J. S. and Grant, J. R. (1996) A Method for Determining the Velocity Induced by Highly Anisotropic Vorticity Blobs *J. Comput. Phys.* **126**, 286-298.

[65] Bergdorf, M., Cottet, G.-H., & Koumoutsakos, P. Multilevel Adaptive Particle Methods for Convection-Diffusion Equations *Multiscale Model. Simul.* **4**, 328-357.

[66] Rossi, L. F. (2006) Evaluation of the Biot-Savart Integral for Deformable Elliptical Gaussian Vortex Elements *SIAM J. Sci. Comput.* **28**, 1509-1532.

[67] Fukagata, K., Kasagi, N., & Koumoutsakos, P. (2006) A Theoretical Prediction of Friction Drag Reduction in Turbulent Flow by Superhydrophobic Surfaces *Phys. Fluids* **18**, 051703.

[68] Kajishima, T. (1999) Finite-Difference Method for Convective Terms Using Non-Uniform Grid. *Trans. JSME/B*, **65**-633, 1607-1612.

[69] Ham, F. E., Lien, F. S., & Strong, A. B. (2002) A Fully Conservative Second-Order Finite Difference Scheme for Incompressible Flow on Nonuniform Grids. *J. Comput. Phys.* **177**, 117-133.

[70] Spalart, P. R., Moser, R. D., & Rogers, M. M. (1991) Spectral Methods for the Navier-Stokes Equations with One Infinite and Two Periodic Directions. *J. Comput. Phys.* **96**, 297-324.

[71] Dukowicz, J. K. & Dvinsky, A. S. (1992) Approximate Factorization as a Higher-Order Splitting for the Implicit Incompressible Flow Equations. *J. Comput. Phys.* **102**, 336-347.

[72] Hrycak, T. & Rokhlin, V. (1998) An Improved Fast Multipole Algorithm for Potential Fields. *SIAM J. Sci. Stat. Comput.* **19**-6, 1804-1826.

[73] Cheng, H., Greengard, L. & Rokhlin, V. (1999) A Fast Adaptive Multipole Algorithmin Three Dimensions. *J. Comput. Phys.* **155**, 468-498.

[74] White, C. A. & Head-Gordon, M. (1996) Rotating Around the Quartic Angular Momentum Barrier in Fast Multipole Method Calculations. *J. Chem. Phys.*, **105**-12, 5061-5067.

[75] Blanco, M. A., Floreza, M., & Bermejo, M. (1997) Evaluation of the Rotation Matrices in the Basis of Real Spherical Harmonics. *J. of Mol. Struct.*, **419**, 19-27.

[76] Sheel, T. K., Yasuoka, K., & Obi, S., (2007) Fast Vortex Method Calculation using a Special-Purpose Computer. *Comput. Fluids*, **36**-8, 1319-1326.

[77] Anderson, C.R., (1992) An Implementation of the Fast Multipole Method Without Multipoles. *SIAM J. Sci. Stat. Comput.* **13**, 923-947.

[78] Makino, J., (1999) Yet Another Fast Multipole Method Without Multipoles-Pseudoparticle Multipole Method. *J. Comput. Phys.* **151**, 910-920.

[79] Bernard, P. S. & Wallace, J. M. (2002) *Turbulent Flow* John Wiley & Sons.

[80] Hinze, J. O. (1975) *Turbulence* McGraw-Hill.